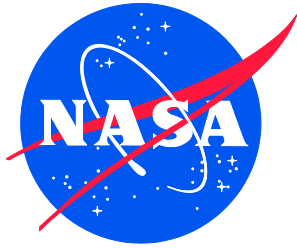# Implementation of J-A Methodology Elastic-Plastic Crack Instability Analysis Capability into the WARP-3D Code

Kenneth R. Hamm, Jr./NESC
Langley Research Center, Hampton, Virginia

Banavara R. Seshadri
National Institute of Aerospace, Hampton, Virginia

David S. Dawicke
Analytical Services and Materials, Hampton, Virginia

Ivatury S. Raju/NESC Retired
Langley Research Center, Hampton, Virginia

NASA STI Program . . . in Profile

Since its founding, NASA has been dedicated to the advancement of aeronautics and space science. The NASA scientific and technical information (STI) program plays a key part in helping NASA maintain this important role.

The NASA STI program operates under the auspices of the Agency Chief Information Officer. It collects, organizes, provides for archiving, and disseminates NASA's STI. The NASA STI program provides access to the NTRS Registered and its public interface, the NASA Technical Reports Server, thus providing one of the largest collections of aeronautical and space science STI in the world. Results are published in both non-NASA channels and by NASA in the NASA STI Report Series, which includes the following report types:

- TECHNICAL PUBLICATION. Reports of completed research or a major significant phase of research that present the results of NASA Programs and include extensive data or theoretical analysis. Includes compilations of significant scientific and technical data and information deemed to be of continuing reference value. NASA counter-part of peer-reviewed formal professional papers but has less stringent limitations on manuscript length and extent of graphic presentations.

- TECHNICAL MEMORANDUM. Scientific and technical findings that are preliminary or of specialized interest, e.g., quick release reports, working papers, and bibliographies that contain minimal annotation. Does not contain extensive analysis.

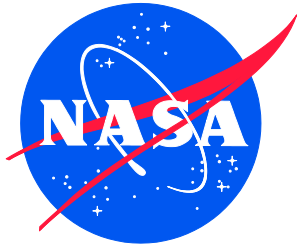- CONTRACTOR REPORT. Scientific and technical findings by NASA-sponsored contractors and grantees.

- CONFERENCE PUBLICATION. Collected papers from scientific and technical conferences, symposia, seminars, or other meetings sponsored or co-sponsored by NASA.

- SPECIAL PUBLICATION. Scientific, technical, or historical information from NASA programs, projects, and missions, often concerned with subjects having substantial public interest.

- TECHNICAL TRANSLATION. English-language translations of foreign scientific and technical material pertinent to NASA's mission.

Specialized services also include organizing and publishing research results, distributing specialized research announcements and feeds, providing information desk and personal search support, and enabling data exchange services.

For more information about the NASA STI program, see the following:

- Access the NASA STI program home page at *http://www.sti.nasa.gov*

- E-mail your question to help@sti.nasa.gov

- Phone the NASA STI Information Desk at 757-864-9658

- Write to:
  NASA STI Information Desk
  Mail Stop 148
  NASA Langley Research Center
  Hampton, VA 23681-2199

Implementation of J-A Methodology Elastic-Plastic Crack Instability Analysis Capability into the WARP-3D Code

Kenneth R. Hamm, Jr./NESC
Langley Research Center, Hampton, Virginia

Banavara R. Seshadri
National Institute of Aerospace, Hampton, Virginia

David S. Dawicke
Analytical Services and Materials, Hampton, Virginia

Ivatury S. Raju/NESC Retired
Langley Research Center, Hampton, Virginia

November 2018

Acknowledgments

NASA Engineering and Safety Center
Technical Assessment Report

Implementation of J-A Methodology Elastic-Plastic Crack Instability Analysis Capability into the WARP-3D Code

November 8, 2018

Report Approval and Revision History

NOTE: This document was approved at the November 8, 2018, NRB. This document was submitted to the NESC Director on November 13, 2018, for configuration control.

Approved:	*Original Signature on File*	11/13/18
	NESC Director	Date

Version	Description of Revision	Office of Primary Responsibility	Effective Date
1.0	Initial Release	Kenneth Hamm, NESC Chief Engineer's Office, ARC	11/8/18

Table of Contents

Technical Assessment Report

List of Figures

List of Tables

Technical Assessment Report

1.0   Scope

Determination of stress field and constraint around the crack tip is critical for achieving reliable fracture control analysis results for all space and non-space programs that require fracture control analysis. The vast majority of fracture mechanics analysis performed in support of fracture control rationale is carried out using reasonably conservative values for initiation fracture toughness derived from high constraint test geometries. An attempt is made to reduce conservatism and consider constraint specific toughness capability. This required using J resistance curve data obtained from standard specimens that were adjusted to match the component versus test specimen constraint level (i.e., A constraint parameter).

For effectively performing this improved analysis approach, a special software code was required that was accurate, efficient, and easy to use. This report summarizes the attempts at ongoing processes to achieve development of such software.

The key stakeholders for this assessment are all NASA and commercial space companies that need to meet fracture control requirements for human and robotic programs.

2.0   Signature Page

Submitted by:

Team Signature Page on File – 11/14/18
_____
Mr. Kenneth R. Hamm, Jr.   Date

Significant Contributors:

_____   _____
Dr. Banavara R. Seshadri   Date   Dr. David S. Dawicke   Date

_____
Dr. Ivatury S. Raju   Date

Signatories declare the findings, observations, and NESC recommendations compiled in the report are factually based from data extracted from program/project documents, contractor reports, and open literature, and/or generated from independently conducted tests, analyses, and inspections.

3.0   Team List

Name	Discipline	Organization
Core Team		
Kenneth Hamm	NESC Lead	ARC
Ivatury Raju	Technical Lead	NESC, Retired
Royce Forman	Materials	JSC, Retired
Mohammad Zanganeh	Materials	JSC
Banavara R. Seshadri	Material Modeling/Analysis	LaRC/NIA
Venkataraman Shivakumar	Materials	Jacobs, Retired
Dave Dawicke	Testing	LaRC/AS&M
Consultants		
Ken Johnson	Statistics	MSFC
Lorie Grimes-Ledesma	Materials	JPL
Business Management		
Catherine Little	Program Analyst	LaRC/MTSO
Assessment Support		
Diane Sarrazin	Project Coordinator	LaRC/AMA
Linda Burgess	Planning and Control Analyst	LaRC/AMA
Erin Moran	Technical Editor	LaRC/AMA

3.1   Acknowledgements

The team would like to thank all those who read and provided input or comments to this report. We would especially like to thank the technical peer reviewers whose insightful questions and comments have made this a much better product. They are, Dr. Phillip Allen (MSFC), Dr. James Mcmahon (JSC), Dr. James Smith (JSC), Mr. Joachim Beek (JSC), Mr. Steven Gentz (MSFC/NESC), and Dr. Gregory Swanson (MSFC).

4.0   Executive Summary

Characterization of the near crack-tip stress/strain fields is the foundation of fracture mechanics. The description of the near tip stress field and the prediction of when fracture occurs is well established for brittle materials that exhibit linear elastic behavior. However, in ductile materials or conditions that violate linear elastic assumptions (Aluminum alloys, Al 2024-T3, Al 2024-T351 etc.), the elastic-plastic crack-tip stress fields are characterized by the Hutchison-Rice-Rosengren (HRR) field. The J-integral is commonly used to characterize amplitude of the HRR field under elastic-plastic conditions. The J-integral has been demonstrated for crack-tip fields that are under high constraint conditions (i.e., small-scale plasticity where the J-dominance is maintained). However, as the external load increases, yielding changes from small- to large-scale plasticity and usually a loss of constraint (i.e., reduction in the triaxial stress field along the crack front). The loss of constraint leads to the deviation of the crack-tip stress fields from that given by the HRR field. Hence, the J-dominance will be gradually lost and additional parameter(s) are required to quantify the crack-tip stress fields and predict fracture behavior.

The assessment objectives were to: 1) implement a two-parameter (i.e., J-A) fracture criterion into an elastic-plastic three-dimensional (3D) finite element analysis (FEA), 2) validate the implementation by comparison with the A parameter from literature data, 3) conduct material characterization tests to quantify the material behavior and provide fracture data for validation of the J-A fracture criteria, and (4) perform evaluations to establish if the J-A criteria can be used to predict fracture in a ductile metallic material (e.g., aluminum alloys). The A parameter in these criteria is the second parameter in a three-term elastic–plastic asymptotic expansion of the near-tip stress behavior.

A series of extensive FEAs were performed using WARP3D [ref. 27][1] software package to obtain solutions for the A parameter for different specimen configurations. The methodology needed for the estimation of the A parameter in the asymptotic expansion was developed and implemented using Matlab® [ref. 29]. A user material (UMAT) routine was used to model the material stress-strain response using a Ramberg-Osgood power law with a hardening exponent (n) and a material coefficient (α). This UMAT routine was successfully implemented in WARP3D software and validated through comparison with the experimental data.

Three configurations were extracted from published results: 1) center cracked plate (CCP), 2) single edge-cracked plate (SECP), and 3) double edge-cracked plate (DECP). These configurations and four other configurations (three-hole tension (THT)), three-point bend (3PTB), three-hole compact tension (3PCT), and compact tension (CT)) were analyzed to verify the methodology that was developed and implemented into WARP3D. Solutions of the A parameter were obtained for remote tension loading conditions that started with small-scale yielding and continued into the large-scale plasticity regime. The results indicate that the methodology developed can be used to calculate the elastic–plastic J-A parameters for test specimens with a range of crack geometries, material strain hardening behaviors, and loading conditions. The J-A parameters were implemented as fracture criteria and used to predict the test results. For comparison, other fracture criteria were used to predict the same test results.

---

[1] WARP3D is an open source finite element code for 3D nonlinear analysis of solids. The capabilities of the code focus on fatigue & fracture analyses, primarily in metals. WARP is not an acronym, but a term borrowed from the *Star Trek* TV series.

Major findings include: The A constraint parameter A varies with specimen type and applied load thus accurate determination is crucial in predicting the failure load, and the A parameter is asymptotic as the failure load is approached, making an accurate determination difficult (i.e., small differences in the A parameter can cause large variations in failure load) for materials exhibiting elastic-plastic behavior. The failure predictions from J-A methodology were more accurate than the traditionally used K_C and J methods, and have comparable scatter to that observed when using the crack-tip opening angle (CTOA) method. However, the J-A methodology requires considerable effort (expertise level and labor) to implement and to evaluate the A parameter for different specimen types and materials, or to apply this methodology to part-through crack (e.g., 3D problems) structural applications.

5.0   Background/Problem Description

Characterizations of crack-tip stress/strain fields are the foundation of fracture mechanics. In classical elastic-plastic fracture mechanics (EPFM), the J-integral is commonly used to characterize amplitude of the elastic-plastic crack-tip stress fields (i.e., the HRR field) [refs. 1–3]. The J-integral has been demonstrated for crack-tip fields under high constraint conditions where the J-dominance is maintained and the HRR fields [refs. 2 and 3] characterize the crack-tip stress/strain fields. However, as the external load increases from small- to large-scale yielding, there is a loss of constraint along the crack front and the stress field deviates from that given by the HRR fields. Hence, the J-dominance will be gradually lost and additional parameter(s) would be required to quantify the crack-tip stress fields. All the detailed information involving crack-tip stress fields, J-integral, HRR field and CTOA are presented in Appendix A.

Several two-parameter approaches for elastic–plastic crack-tip fields have been proposed to overcome the limitation of J-based fracture mechanics approach. References 4 and 5 proposed to use the amplitude of the second term in the asymptotic expansion for mode I plane-strain condition of power-law hardening material as an additional parameter. References 6 through 8 proposed the J-T approach using the second term of Williams' expansion of the elastic crack-tip field [ref. 9] as constraint parameter (T) to describe elastic–plastic crack-tip fields for a variety of plane-strain cases. References 10 and 11 suggested the J-Q approach based on the main feature of the elastic–plastic crack-tip stress fields. The second fracture parameter Q is defined as the difference between the stresses in crack-tip region determined by numerical analysis and the HRR or small-scale yielding (SSY) stress fields. A detailed discussion on two parameter approaches J-T and J-Q are presented in Appendix A. References 12 and 13 expanded on references 4 and 5 by conducting a more sophisticated analysis of the higher order terms of asymptotic expansion of stress and displacement fields in the crack-tip. A three-term expansion of the crack-tip field was derived with J and A that is the dimensionless amplitude of the second order term. This work confirmed that, in general a two-term expansion is not sufficient to characterize crack-tip behavior, but using more than three terms in the asymptotic expansion of field is redundant for plane strain mode I cracks. Later, references 14 and 15 presented the three-term expansion in another format and suggested to use the magnitude of the second term in the series expansion A, with J to characterize the crack-tip stress fields.

In summary, it has been shown that these two-parameter approaches (i.e., J-T, J-Q and J-A) provide effective characterization of plane-strain elastic–plastic crack-tip fields in a variety of crack configurations and loading conditions. To use the constraint-based structural integrity procedures, both the first parameter (i.e., J-integral) and the second parameter (i.e., constraint parameter) need to be obtained for the cracked components under consideration. In particular, the numerical and analytical methods to obtain T-stress for two-dimensional (2D) and 3D crack geometries have been developed [refs. 16–19]. Solutions of T-stress were developed for a range of 2D and 3D crack geometries and loading conditions [refs. 19-22]. However, unlike the T-stress, the determination of the second elastic-plastic parameters (e.g., Q and A) are not as well established. Due to material nonlinearities, the elastic-plastic parameters will depend on the material hardening characteristics, specimen/crack geometry, and external loading conditions. Reference 23 suggested the one-to-one relationships between the Q factor and the T-stress under small to contained yielding conditions. Contained yielding is defined as the state in which the

plastic zone is on a length scale that is small compared to, for example, crack length and thickness dimensions. This reference also suggests using pure power-law hardening solutions to estimate Q factors under fully plastic conditions. An overall empirical formula to estimate Q factors from small to large scale yielding was proposed by interpolating between the small-scale yielding solutions based on T-stress and the fully plastic solutions. Reference 13 determined the A parameter values by matching the three-term expansion on one stress component with the finite element (FE) solutions at one or several locations within the plastic zone. Reference 15 suggested an algorithm to obtain the A parameter by fitting the three-term expansion using one typical stress component with the FE results in the region that is significant for the fracture process. It is difficult to determine the Q or A values for a wide range of loading, geometric, and material properties. Therefore, available solutions for Q or A are limited. Some solutions can be found for 2D [refs. 24-26], but further systematic development is required.

The overall goal of this study was to evaluate J-A methodology to determine the applicability of using this approach as failure prediction tool. This required the understanding of the advantages and limitations of the technique and the associated implementation challenges involved in the incorporation into commercial codes. The assessment plan was to: implement the J-A fracture criteria into a FEA; verify the calculated A parameter with available literature data; and evaluate if the J-A criteria can be used to predict fracture in ductile metallic materials.

Material characterization and fracture tests were conducted on 2024-T3 aluminum coupons extracted from 1-inch thick plates. The material characterization tests included tensile and tension/torsion tests to generate data for the stress-strain model required in the finite element analysis. The fracture tests included several different configurations to provide different levels of constraint for evaluation of the fracture model. The description of different types of tests conducted are explained in Appendix B.

Series of extensive FEAs were conducted using WARP3D software to obtain solutions of the A parameter for different types of test specimen configurations. The methodology needed for the estimation of the A parameter in the asymptotic expansion was developed and implemented using Matlab® software. Empirical equations to predict the A parameter under SSY to fully plastic conditions were developed based on FE results. In particular, an empirical law [ref. 15] was implemented to enable the determination of the A parameter for a given crack configuration. Several configurations were analyzed using this methodology: 1) CCP, 2) SECP, and 3) DECP. Solutions of the A parameter accounted for material nonlinearity using the Ramberg–Osgood power law with n and α. The UMAT routine that modeled the Ramberg-Osgood material behavior was successfully implemented in WARP3D software. Remote tension loading was applied to generate behavior from small- to large-scale yielding. In addition, the THT, 3PTB, and CT coupons were analyzed and the A parameter was estimated for each coupon and applied load condition. The results indicate the methodology developed can used to calculate the second elastic–plastic fracture parameters for test specimens for a range of crack geometries, material strain hardening behaviors, and loading condition.

5.1 Theoretical Background: J-A Two-Parameter Characterization of Crack-tip Fields

References 12 and 13 suggested the J–A_2 two-parameter fracture mechanics approach. The A_2 parameter represents the magnitude of the second term in the series expansion of crack-tip stress fields. References 14 and 15 derived the same series expansion and suggested that the magnitude of second term in the series could be used with J to characterize the crack-tip stress

fields. A similar approach (J-A) [ref. 15] used a different normalized form of A_2. In this report, the solutions of the A parameter were calculated and the formula expressions and the terminologies of variables used by references 14 and 15 were followed. Once solutions of the A parameter were determined, the magnitude of A_2 can be obtained. The elastic–plastic material behavior is described by deformation theory with the Ramberg–Osgood uniaxial stress–strain curve:

$$\frac{\epsilon}{\epsilon_0} = \frac{\sigma}{\sigma_0} + \alpha \left(\frac{\sigma}{\sigma_0}\right)^n \tag{1}$$

where σ_o is the yield stress; α is a material coefficient; n is the hardening exponent ($n > 1$); $\epsilon_o = \sigma_o / E$; and E is the Young's modulus.

The three-term asymptotic solution for stress near the crack-tip in elastic–plastic material can be written [refs. 14 and 15] as:

$$\frac{\sigma_{ij}}{\sigma_0} = A_0 \bar{r}^s \bar{\sigma}_{ij}^{(0)}(\theta) + A_1 \bar{r}^t \bar{\sigma}_{ij}^{(1)}(\theta) + A_2 \bar{r}^{2t-s} \bar{\sigma}_{ij}^{(2)}(\theta) \tag{2}$$

where σ_{ij} are stress components, σ_{rr}, $\sigma_{\theta\theta}$, and $\sigma_{r\theta}$ in the polar coordinate system with origin at the crack-tip as shown in Appendix A-1; $\bar{\sigma}_{ij}^{(0)}(\theta)$, $\bar{\sigma}_{ij}^{(1)}(\theta)$, and $\bar{\sigma}_{ij}^{(2)}(\theta)$ are normalized angular stress functions; the power "t" is an eigenvalue depending on n of the Ramberg–Osgood relationship; $s = -1/(n + 1)$; and dimensionless radius $\bar{r}$ is defined as $\bar{r} = r/(J/\sigma_o)$.

The coefficient A_0 is defined as:

$$A_0 = (\alpha \epsilon_0 I_n)^{-1/(n+1)} \tag{3}$$

where I_n is a scaling integral [refs. 2 and 3]. References 12 -14 demonstrated that under plane strain conditions for $n \geq 3$, the amplitude for the second order term A_2 is related to the values of A_0 and A_1 by: $A_2 = {A_1^2}/{A_0}$. For convenience, reference 15 introduced the amplitude parameter $A = -A_1$. This allows the three-term asymptotic expansion to be expressed as:

$$\frac{\sigma_{ij}}{\sigma_0} = A_0 \bar{r}^s \bar{\sigma}_{ij}^{(0)}(\theta) - A \bar{r}^t \bar{\sigma}_{ij}^{(1)}(\theta) + \frac{A^2}{A_0} \bar{r}^{2t-s} \bar{\sigma}_{ij}^{(2)}(\theta) \tag{4}$$

The stress components can be obtained from Eq. (4) after the parameters J and A have been obtained for the crack geometry. Reference 14 proposed a computational algorithm to determine the values of normalized angular functions $\bar{\sigma}_{ij}^{(0)}(\theta)$, $\bar{\sigma}_{ij}^{(1)}(\theta)$, and $\bar{\sigma}_{ij}^{(2)}(\theta)$; asymptotic power "t"; and scaling integral I_n. For engineering applications, based on the computational algorithm [ref. 14], the values of parameters t, s, and I_n are shown in Table 1 for materials with n = 3, 4, 5, 7,

and 10. The normalized functions $\bar{\sigma}_{ij}^{(0)}(\theta)$, $\bar{\sigma}_{ij}^{(1)}(\theta)$, and $\bar{\sigma}_{ij}^{(2)}(\theta)$ can be found in references 12 through 14.

Table 1. The Values of Asymptotic Powers s, t and Scaling Integral I_n

	$n = 3$	$n = 4$	$n = 5$	$n = 7$	$n = 10$
s	-0.2500	-0.2000	-0.1667	-0.1250	-0.0909
t	-0.0128	0.0328	0.0546	0.0694	0.0698
I_n	5.5073	5.2213	5.0235	4.7655	4.5399

5.2   Determination of the A Parameter

The methods of determining J-integral have been established in the literature. The domain integral method is used to calculate J for the FEAs conducted in this report. Several methods were proposed to determine the values of amplitude for the A parameter. The "point match" method solves the quadratic equation of the A parameter (Eq. (4)) for one or more points near the crack-tip using FE results for the selected stress component. For example, references 12 and 13 calculated the A parameter by averaging the calculated values at points $\bar{r} = 2$, $\theta = 0°$, and $45°$ for stress components σ_r and/or σ_θ. A method proposed in reference 15 obtained A by the fitting Eq. (4) to the FE results in the crack-tip region (i.e., typically between $1.5 \leq \bar{r} \leq 5$ and $0° \leq \theta \leq 45°$). For example, for the ith fitting point, Eq. (4) can be expressed as:

$$e_i A^2 + f_i A + g_i = \delta_i \tag{5}$$

$$e_i = \frac{\bar{r}^{2t-s}}{A_0} \bar{\sigma}^{(2)}(\theta_i) \tag{6}$$

$$f_i = -\bar{r}_i^t \bar{r}^t \bar{\sigma}^{(1)}(\theta_i) \tag{7}$$

$$g_i = A_0 \bar{r}_i^s \bar{\sigma}^{(0)}(\theta_i) - \frac{\sigma_{FEM(\bar{r}_i,\theta_i)}}{\sigma_0} \tag{8}$$

where δ_i is the deviation of the asymptotic stress field from the FE stress solution σ_{FEM} at the ith fitting point with the polar coordinates $\bar{r}_i, \theta_i$. Stress components σ_{rr}, $\sigma_{\theta\theta}$, or some combinations (e.g., $\sigma_{rr} + \sigma_{\theta\theta}$) can be used for fitting the stresses. In general, the σ from Eqs. (5-8) can be either σ_{rr} or $\sigma_{\theta\theta}$ stress components, or some combination of the two. Then, minimizing the sum of squares of the deviations $\sum \delta_i^2$ with weights leads to a cubic equation for amplitude of the A parameter as:

$$eA^3 + fA^2 + gA + h = 0 \tag{9}$$

$$e = 2 \sum (a_i^2 w_i^2) \tag{10}$$

$$f = 3 \sum (a_i b_i w_i^2) \tag{11}$$

$$g = \sum (2a_i c_i w_i^2 + b_i^2 w_i^2) \tag{12}$$

$$h = \sum (b_i c_i w_i^2) \tag{13}$$

where w_i is the weight for the ith fitting point. Weights for the points can be proportional to the area that is represented by the ith fitting point. The A parameter values can be obtained by solving this cubic equation for three roots. Off all the three roots, the root that has the same sign as that of c_i is the appropriate root. It was demonstrated in reference 15 that this method gives more consistent and accurate results for the A parameter compared to the ''point match'' method. In this report, least square fit regression analysis capability was used to determine A values using FE results.

5.3   FEA

Extensive FEA were performed using WARP3D to obtain the crack-tip stress fields for different coupon configurations and various loading conditions. Eight noded brick elements (HEX8) and small strain formulation were used in the analyses. The details of the models are outlined in the following sections. The following material properties for 2024-T3 were used in FE analyses, Young's modulus, E = 11128 ksi, Poisson's ratio, v = 0.3, Yield stress, σ_0 = 70.215 ksi, Material coefficient, α = 0.5 and Hardening exponent, n = 10. J and A were estimated from these stress fields and the methodology developed to calculate the A parameter values at each loading condition. J-values were obtained from WARP3D analysis using equivalent domain integral methods. Typically, 5 to 6 domains were used around the crack front. Convergence checks were performed to ensure consistent J-values.

5.4   Implementation of UMAT routine

2024-T3 material was modeled using Romberg-Osgood power law strain hardening relation. Circular unnotched tensile specimens and notched tension-torsion specimens were used in the tests. Appendix B discusses details of all testing. The material model used in current numerical investigation is based on deformation plasticity theory. The Ramberg–Osgood power-law strain hardening relation was implemented as a UMAT routine in WARP3D. The uniaxial tension stress–strain curve from Ramberg–Osgood relation is described in Eq. (1). The UMAT routine was verified by conducting a series of uniaxial tension and combination of torsion-tension tests conducted on 2024-T3 aluminum, as described in Appendix B. The results from the analyses are compared with test data in Figures 1 and 2. As described in Appendix B, the global strain was obtained using virtual extensometers to extract the relative displacement of two points that were initially 1 inch apart. The local strains used a similar virtual extensometer, but with an initial gage length that was 0.1 inch apart and located in the necking region. Variation in global and local stress and strain from test are represented by Global and Local solid lines in Figure1 respectively. Correspondingly, variation in WARP3D analysis global and local stress and strain are indicated by Global-warp3d and Local-warp3d solid lines respectively. Similar comparisons between test and analysis under torsion-tension loading are shown in Figure 2. The comparison shows acceptable agreement suggesting the validity of the implemented UMAT routine.
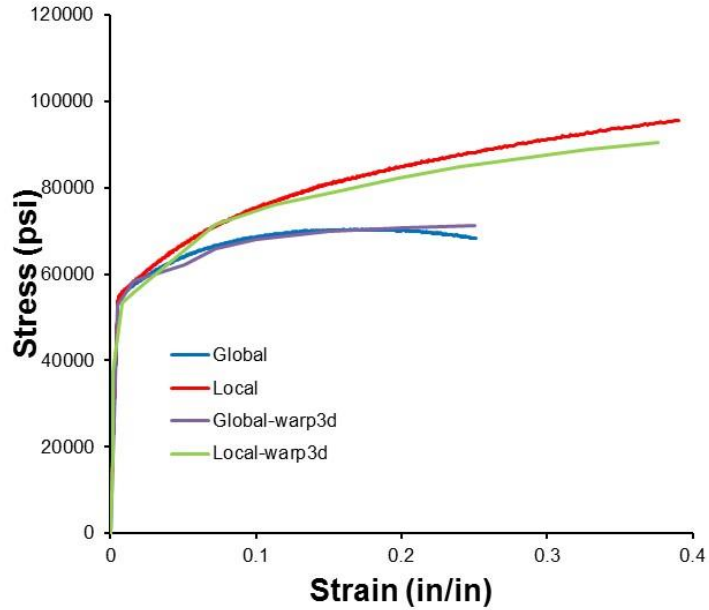
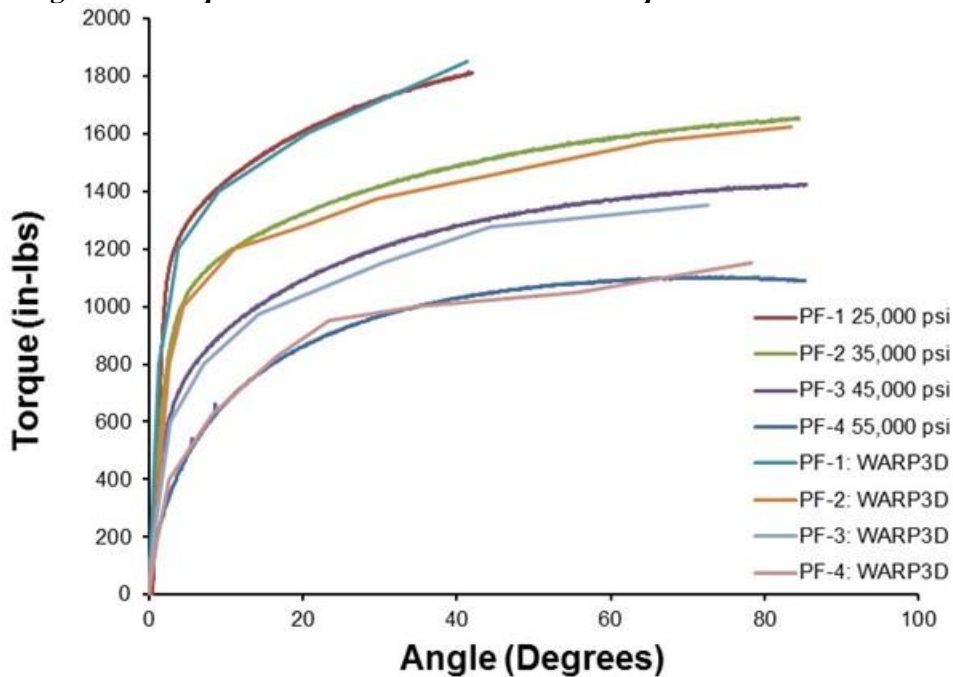Figure 1. Comparison of uniaxial stress-strain response with test data.

Figure 2. Comparison of notch tensile and torsion response with test data.

5.5 Capability to Generate Visualization Tool Kit (VTK) Format Files for Visualization

A new capability to view contour plots of displacement vector, strain, and stress tensors on undeformed and deformed geometry was developed to view in 3D format using PARAVIEW [ref. 28] software and the capability was developed using Matlab® software.

5.6 Capability to Determine A

A new capability to determine amplitude of the A parameter that was discussed in previous Sections 5.1 and 5.2 was developed using Matlab® software. This involved developing a script to read WARP3D analyses results and transferring them into polar coordinates and adding a least square fit regression analysis capability to determine A values.

5.7 Verification of the A Parameter

Three mode I coupon configurations, shown in Figure 3, CCP, SECP, and DECP, were analyzed using WARP3D. The 3D finite element models (FEMs) for CCP, SECP, and DECP specimens were created using 3D brick elements. A typical FE mesh used in WARP3D analyses is illustrated in Figure 4. The 2D plane-strain conditions were simulated with the additional boundary condition of fixing the out-of-plane displacements ($u_Z = 0$). Remote tension loading was applied on the models of the three coupon configurations, and the ratio of coupon length to coupon width (H/W) was 2.0.
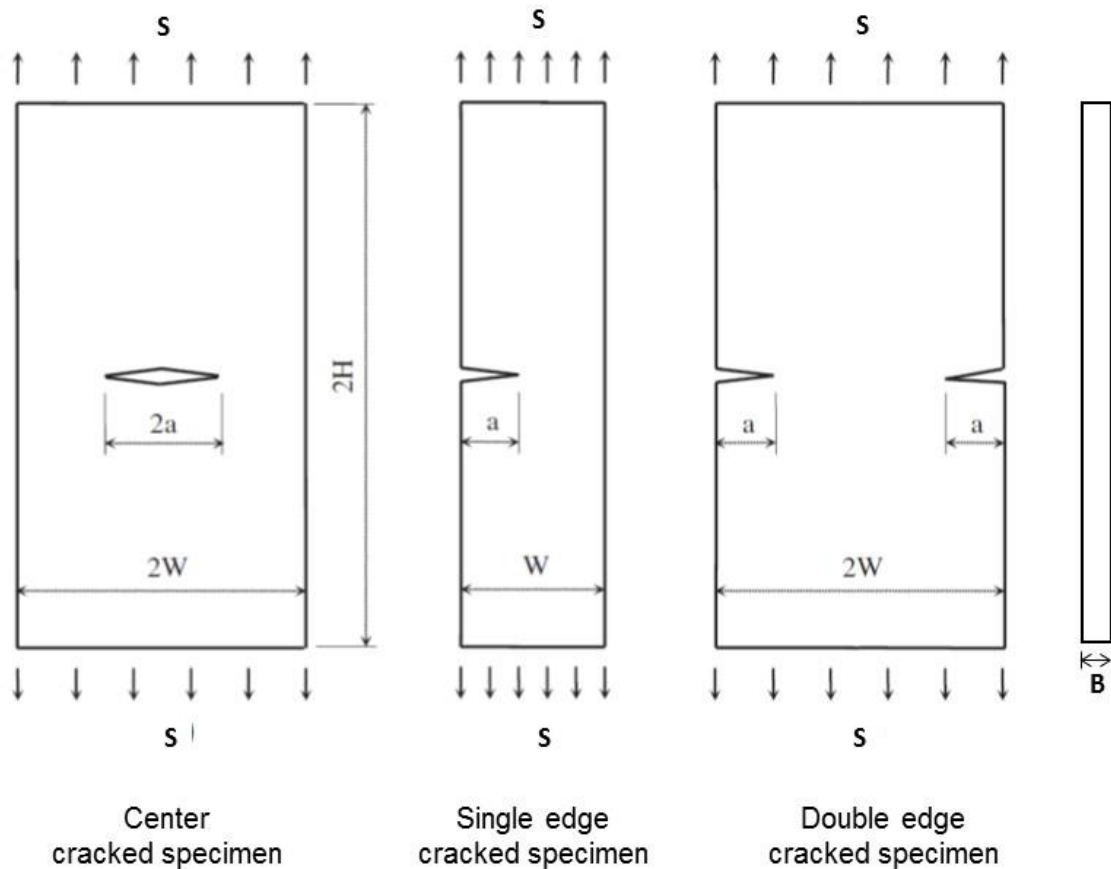

Figure 3. Different specimens analyzed for verifying developed J-A prediction methodology.
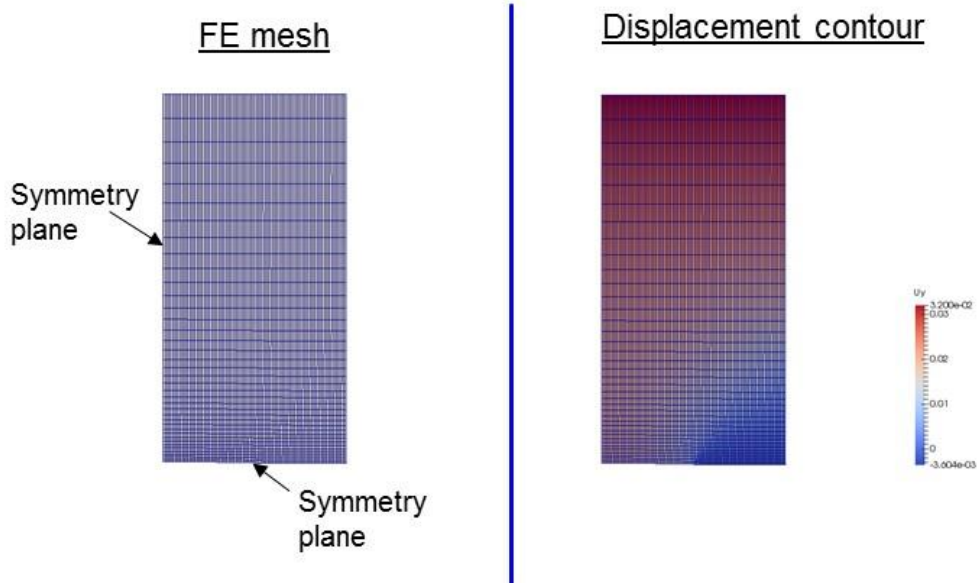
FE mesh | **Displacement contour**

Symmetry plane

Symmetry plane

Figure 4. A typical FE mesh and displacement in y-direction (in.) contour plot for center cracked specimen.

The models were considered sufficiently long to simulate the coupons tested under remote tension loading. A separate FEM was developed for each loading scenario to provide sufficient elements in the fracture process zone to evaluate the A values. A typical FE mesh had around 12,000 nodes and 9,000 eight-noded brick elements (see Figure 4). Using symmetries, one quarter of CCP, a half of SECP, and a quarter of DECP specimen were modeled in the FEA. The limit load (σ_L) are used to normalize the applied stress S for CCP, SECP, and DECP models [ref. 30] are represented by equations (14) through (16) for three coupon configurations.

$$CCP: \quad \sigma_L = \frac{2}{3}\left(1 - \frac{a}{W}\right)\sigma_0 \tag{14}$$

$$SECP: \quad \sigma_L = 1.455\frac{a}{W}\left[-1 + \sqrt{1 + \left(\frac{W-a}{a}\right)^2}\right]\sigma_0 \tag{15}$$

$$DECP: \quad \sigma_L = \left[0.36 + 0.91\left(\frac{W-a}{W}\right)\right]\left(\frac{W-a}{W}\right)\sigma_0 \tag{16}$$

where *a* is half or full crack length, and W is specimen width as shown in Figure 3. CCPs were analyzed using WAR3D to determine the A parameter using the mesh shown in Figure 4. Following the recommendations of Nikishov, at least 80 to100 elements were used in the r_bar range from 1.5 to 5 to carry out regression analyses in the estimation of the A parameter.

Representative displacement, strain, and stress contour plots were generated using developed Matlab® code, as shown in Figures 4 and 5. The results of the A parameter for a/W = 0.5, *n* = 10, and α = 0.5 for increasing external load ratio S/σ_L are shown in Figure 6. For comparison, the results from reference 15 and NAFISS and NASJA solutions are compared in the same figure. Analyses results generated using WARP3D and current methodology correlates

with literature data in the range $0.6 \leq S/\sigma_L \leq 1.2$. At values of S/σ_L below 0.6, the current methodology predicts marginally higher values of the A parameter, and at values of S/σ_L above 1.2 the methodology under predicts the value of the A parameter. Overall, the solution of the A parameter from the current methodology correlates with the literature data for the CCP specimen.
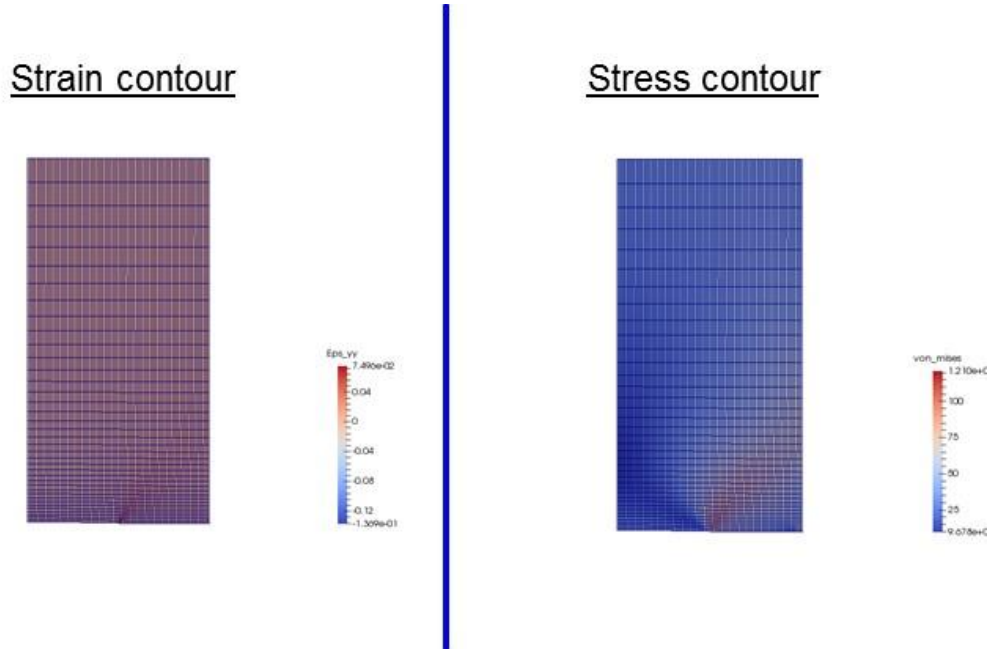
Figure 5. A typical strain and stress (ksi) contour plot for center cracked specimen.
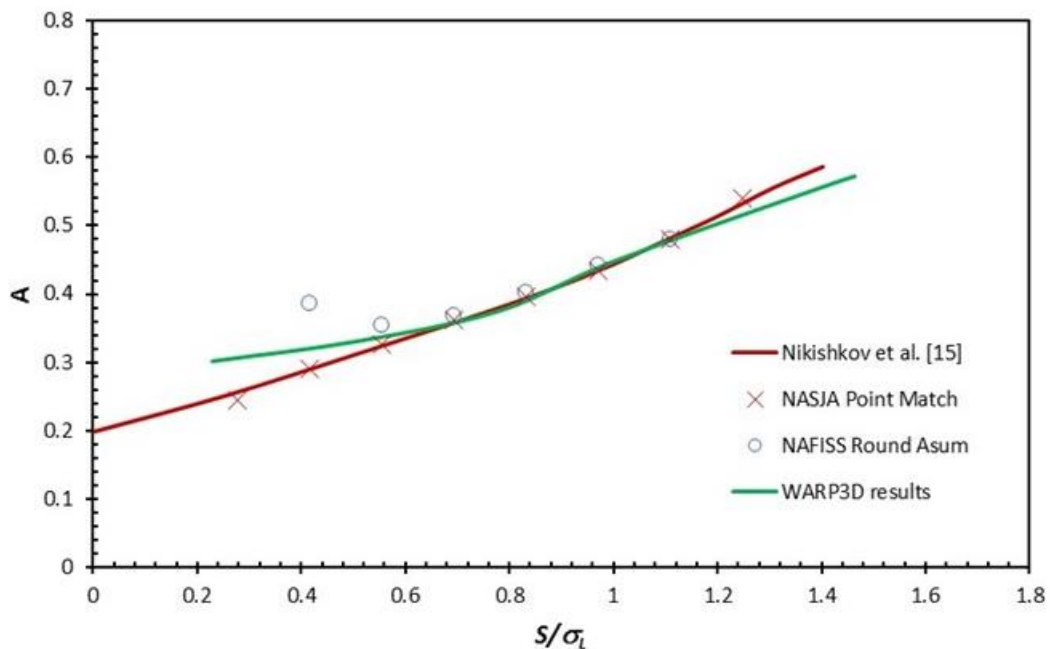

Figure 6. Comparison of A predictions from WARP3D analysis for center cracked specimen.

Representative strain and stress contour plots for a SECP specimen are shown in Figure 7. Comparison of analysis solution of the A parameter for a/W = 0.5, n = 10, and α = 0.5 for increasing S/σ_L for SECP specimen are shown in Figure 8. The analysis solution prediction is higher when compared to reference 15 results. This difference may be related to the different regression analysis algorithm used in the estimation of the A parameter. Representative strain and stress contour plots for the DECP specimen are shown in Figure 9. The comparison of analysis solution of the A parameter for a/W = 0.5, n = 10, and α = 0.5 for increasing S/σ_L for the DECP specimen are shown in Figure 10. Again, the analysis solution predicted is higher when compared to the reference 15 solution.
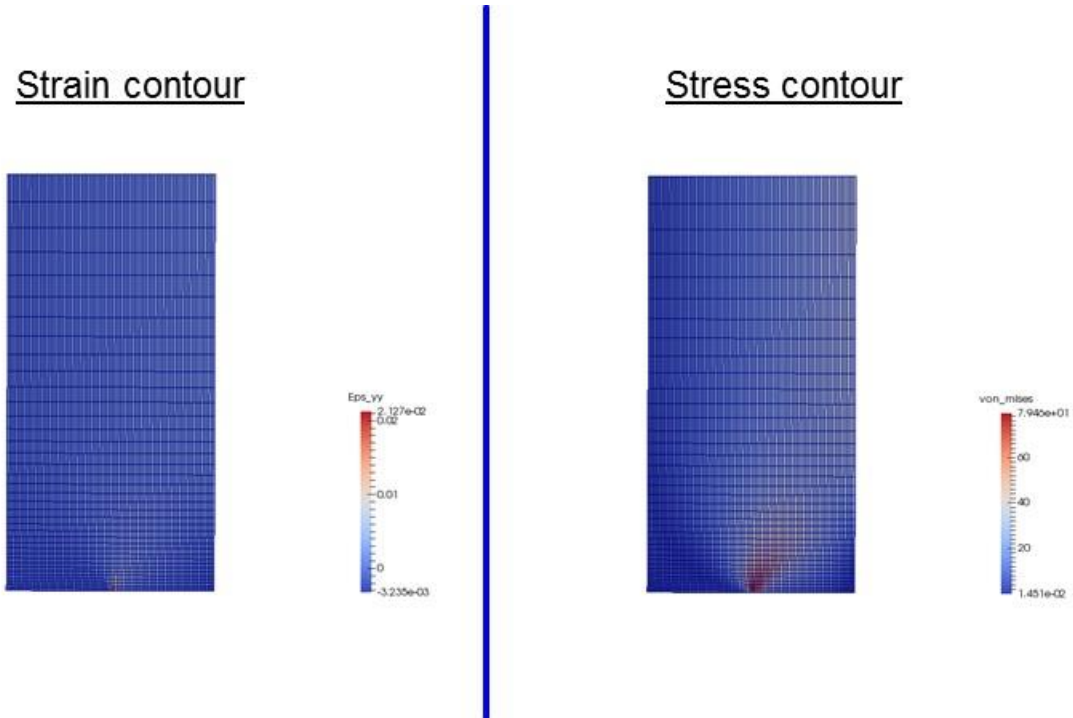

Figure 7. A typical strain and stress (ksi) contour plot for SECP specimen.
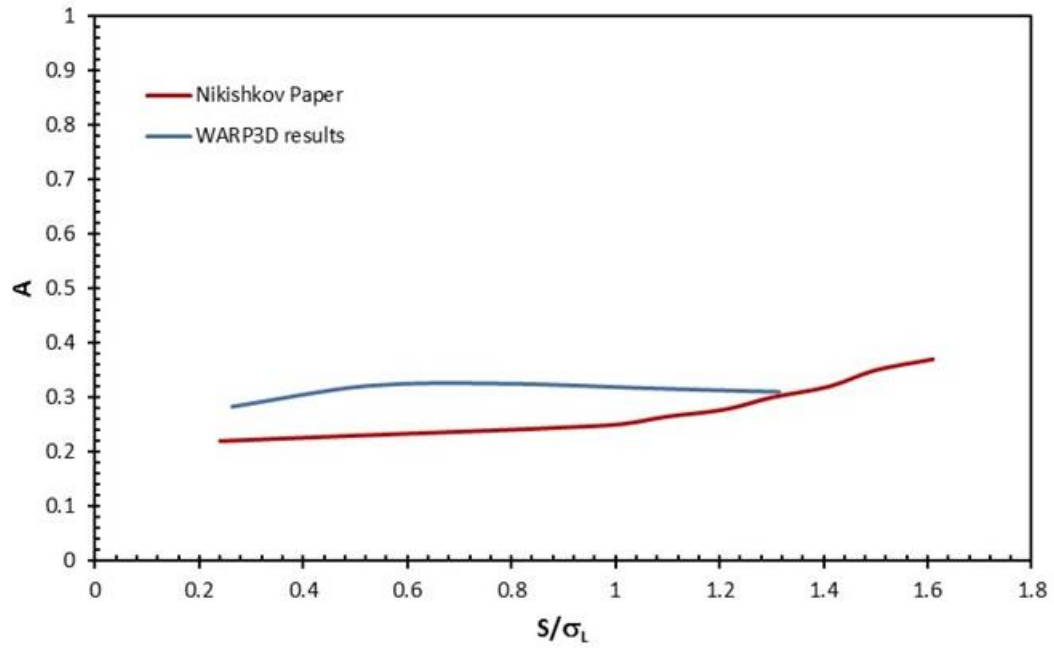
Single Edge Crack a/w=0.5,n=10 α=0.5

Figure 8. Comparison of predicted A from WARP3D analysis for SECP specimen.
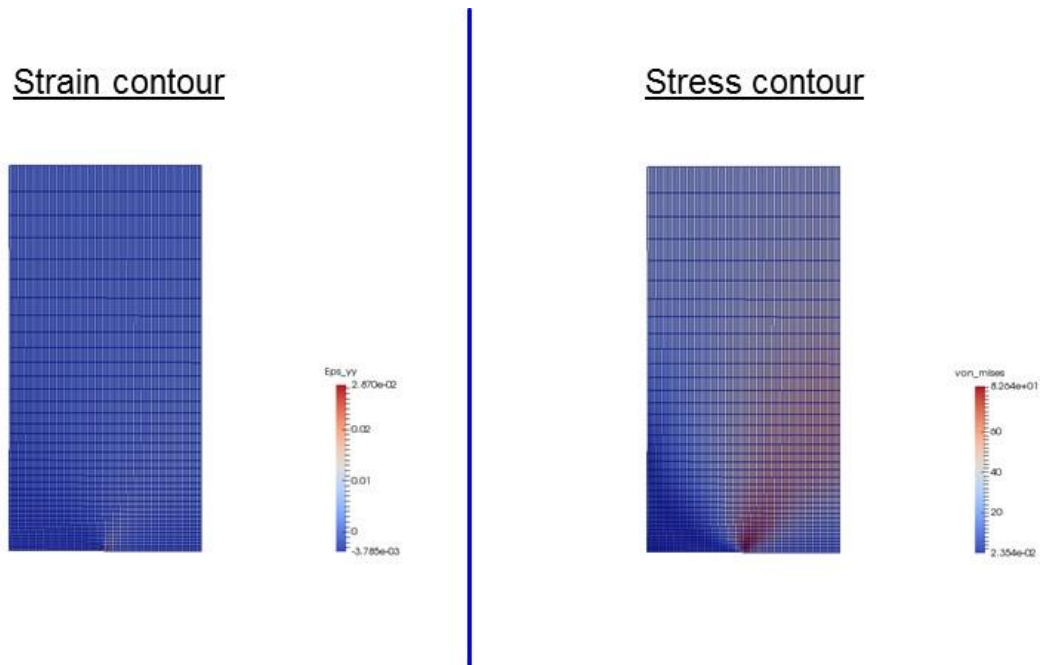

Strain contour

Stress contour

Figure 9. A typical strain and stress (ksi) contour plot for DECP specimen.
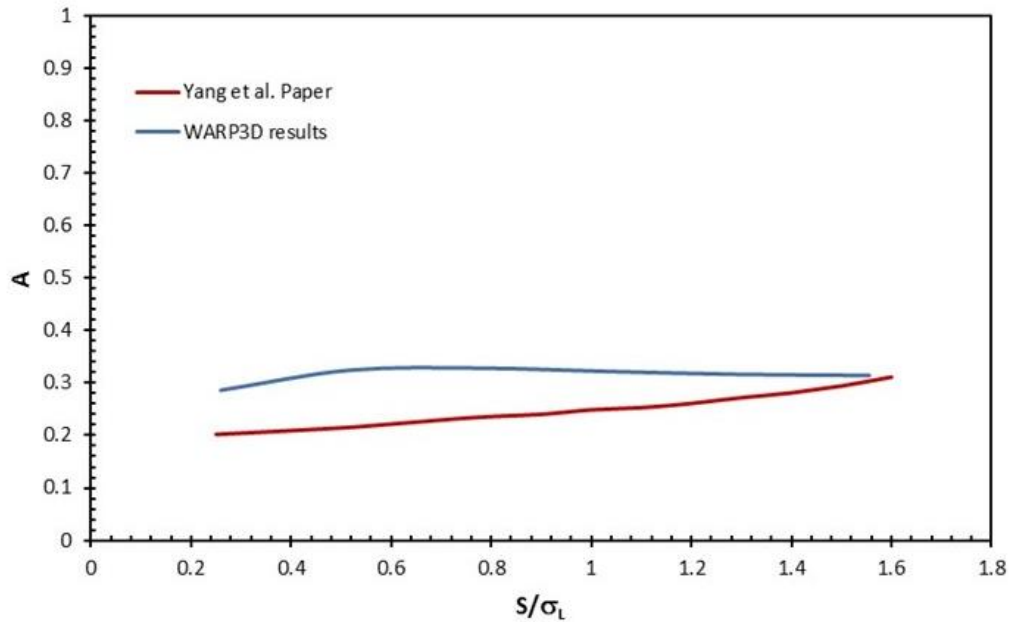
Double Edge Crack a/w=0.5,n=10 α=0.5

Figure 10. Comparison of predicted A from WARP3D analysis for DECP specimen.

5.8 Prediction of A for CT Specimen

The CT specimen shown in Figure 11 was analyzed using WARP3D. The specimen width W = 2.0 inches, and the thickness, was B = 0.75 inch. The 3D FE meshes for CT specimen was created with 3D brick elements. A typical FE mesh used in the WARP3D analyses is illustrated in Figure12. Remote pin loading is applied to the model. A typical FE mesh will have 14,430 nodes and 11,032 eight noded brick elements (see Figure 12). Only a half of CT specimen was modeled in the FE analysis due to symmetries. Additional boundary conditions of $u_Z = 0$, $z = 0$, and $z = B$ were used to simulate 2D plane strain conditions. A separate FEM was developed with sufficient elements in the fracture process zone to be able to evaluate the A parameter for each applied load condition. Representative of displacement and stress contour plots were generated using developed Matlab® code, as shown in Figure 13. The limit load P_L was used to normalize the applied load P for CT specimen is represented by equation (17). The ratio P/P_L can go beyond 1 and other authors like Nikishkov and Yang et al. have shown in their study too that if can go beyond one up to 1.4. The results of the A parameter solution for a/W = 0.5, $n = 10$, and $\alpha = 0.5$ for increasing external load ratio P/P_L is shown in Figure 14. For most of applied load ratios (i.e., P/P_L below 1.1) the predicted value of the A parameter remains nearly constant. In other words, the constraint level at the crack-tip remains nearly constant over a larger portion of applied load ratio. This is why CT specimens are preferred over other types of specimens in generating fracture parameters for different materials and thickness. Only beyond applied ratio of 1.2 does the A parameter increase, indicating a loss of constraint at the crack-tip at higher load levels. Overall, the solution of the A parameter for CT specimen remains constant for major portion of applied load.
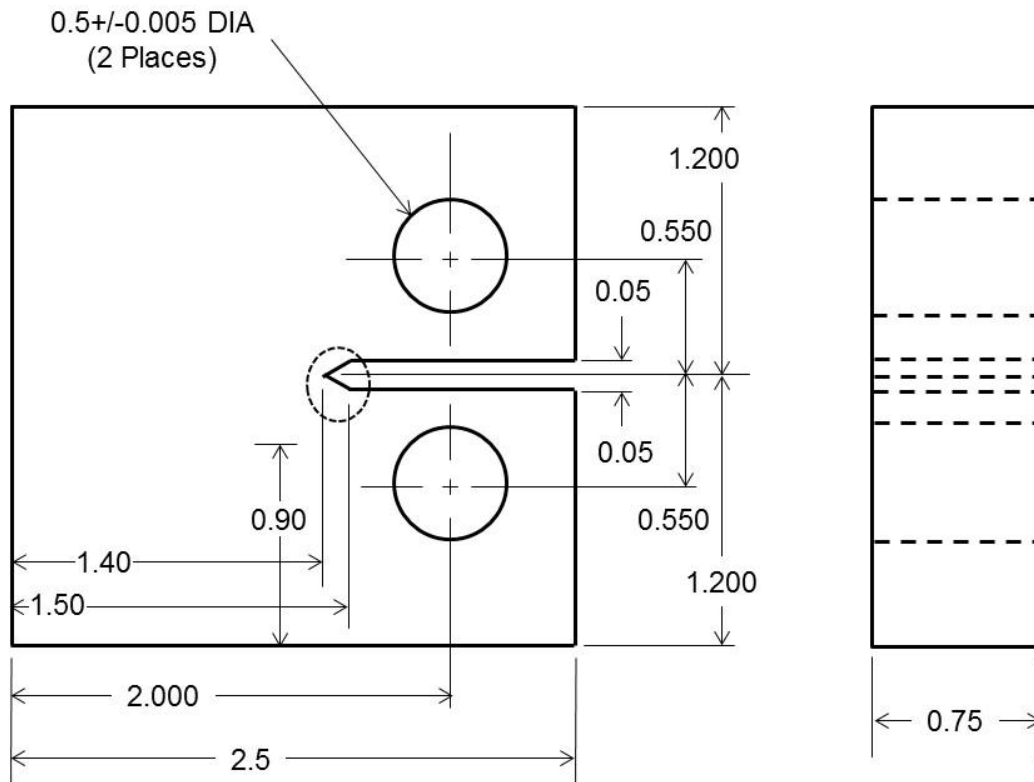
Figure 11. Schematic of CT specimen.
(all dimensions are in inches)

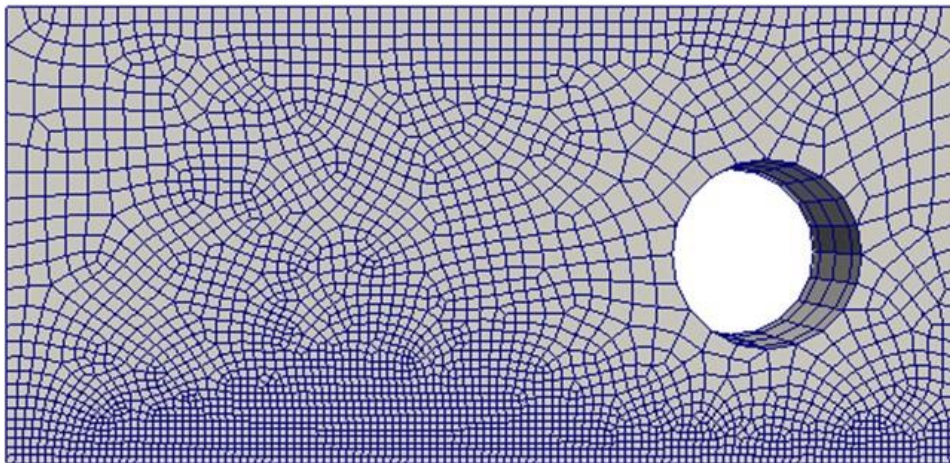**Figure 12. A typical FE mesh for CT specimen.**
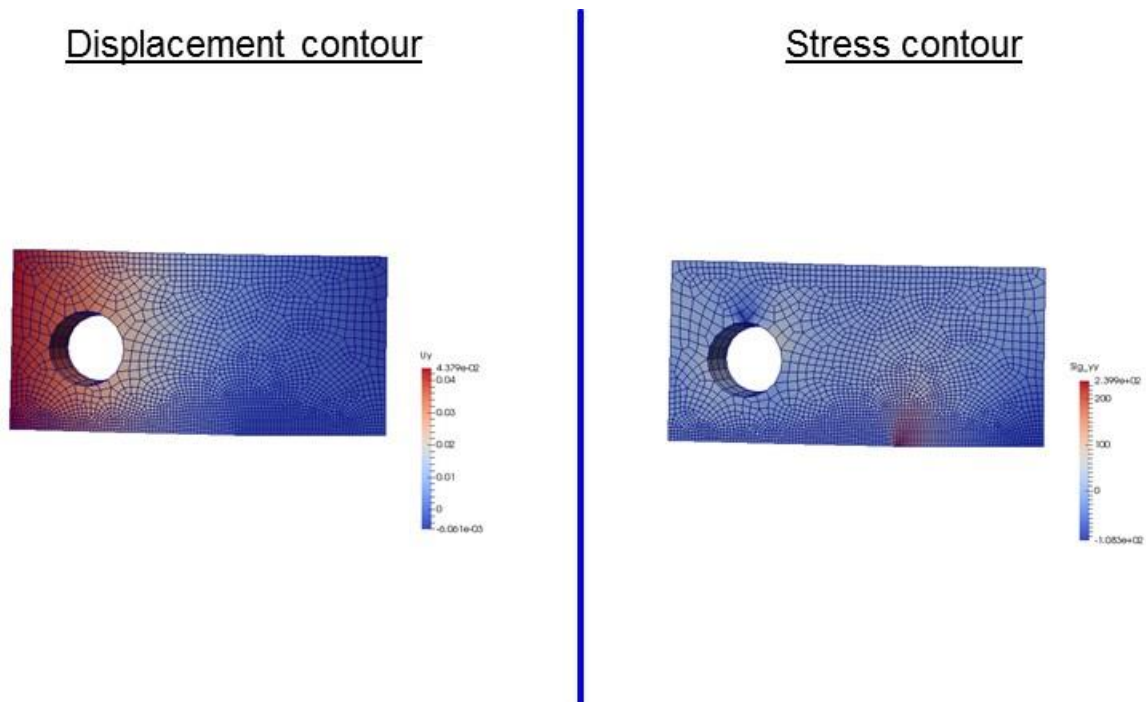
Figure 13. A Typical displacement and stress (ksi) contour plot for CT specimen.
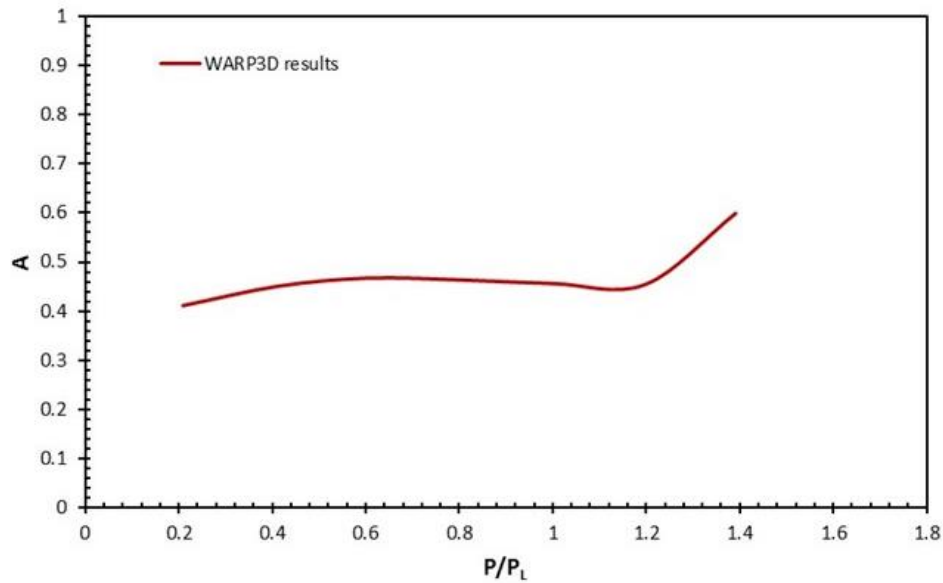

Figure 14. Predicted A from WARP3D analysis for CT specimen.

$$CT: \quad P_L = 1.455\sigma_o WB \left[-1 - \frac{a}{W} + \sqrt{2 + 2\left(\frac{a}{W}\right)^2} \right] \tag{17}$$

5.9 Comparison of A for CCP, SECP, DECP, and CT Specimen

Variation in the A parameter for different specimen types are compared in Figure 15. For a given normalized applied load, the comparison shows each specimen has different level of constraint at the crack-tip. Due to variation in constraint level, the fracture behavior will vary depending on the specimen type. Therefore, the level of initial constraint at the crack-tip and loss of constraint with increasing load will have significant influence on the fracture behavior and the expected failure load.
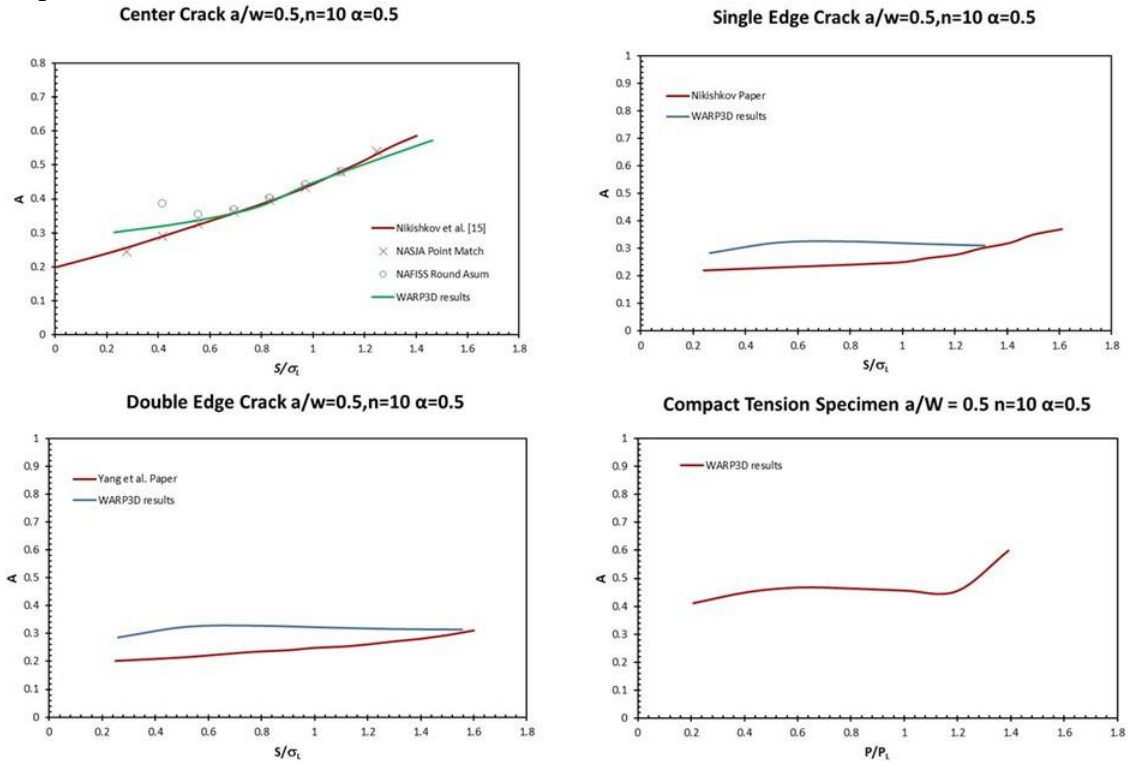

Figure 15. Comparison of estimated A for different types of specimens.

5.10 Prediction of A for 3PTB Specimen

A typical 3PTB specimen, shown in Figure 16, was analyzed using WARP3D. The specimen length was 7.5 inches, and the thickness was B = 0.75 inch. 3D FEMs for 3PTB specimen were created with 3D brick elements. A schematic of 3PTB fixture dimension with CMOD measurement location is shown in Figure 17. A typical FEM used in the WARP3D analyses is shown in Figure 18. Remote bending load is applied on the model. A typical FE mesh had 10,945 nodes and 8,372 eight-noded brick elements. Only a half of 3PTB specimen was modeled in the FEA due to symmetries. Additional boundary condition of $u_z = 0$ was used on the z = 0 and z = B planes to simulate 2D plane strain conditions. FEMs were developed for each applied load condition to provide sufficient elements in the fracture process zone to evaluate the A parameter. Representative displacement and strain contour plots were generated using developed Matlab® code, as shown in Figure 19. P_L was used to normalize the applied load P for 3PTB specimen is represented by equation (18). The results of the A parameter solution for a/W = 0.3 and 0.6, n = 10, and α = 0.5 for increasing P/P_L is shown in Figure 20. At values of P/P_L below 0.4, the predicted value of the A parameter for a/W =0.3 and 0.6 are comparable. With increasing applied load, the A parameter increases, indicating a loss of

constraint. For values of $P/P_L > 1$, the A parameter increases further at a higher rate for $a/W = 0.3$ compared to 0.6 indicating larger rate of loss of constraint for $a/W = 0.3$. Overall, the solution of the A parameter for 3PTB specimen implies that there is a loss of constraint at the crack-tip with increasing applied load, and the increase is larger for $a/W = 0.3$ compared to 0.6.

$$3PB: \quad P_L = 1.455\sigma_o \frac{W^2}{2H}\left(\frac{W-a}{W}\right)^2 \tag{18}$$
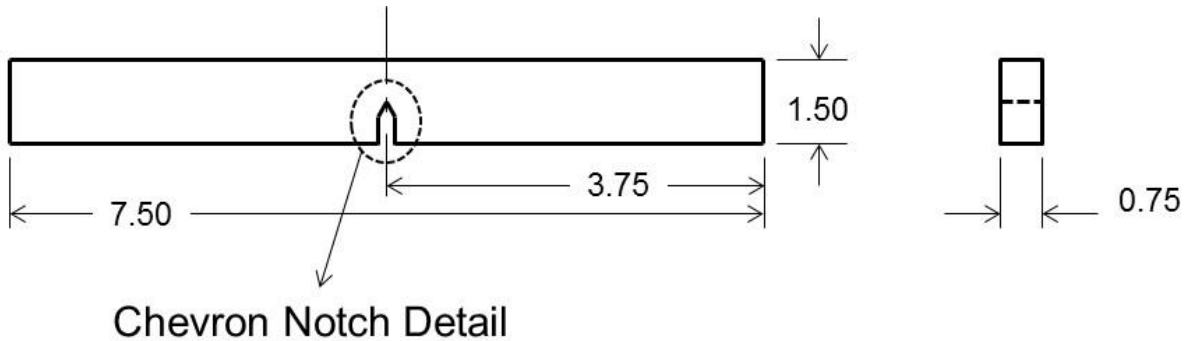

Chevron Notch Detail

Figure 16. Schematic of 3PTB specimen.
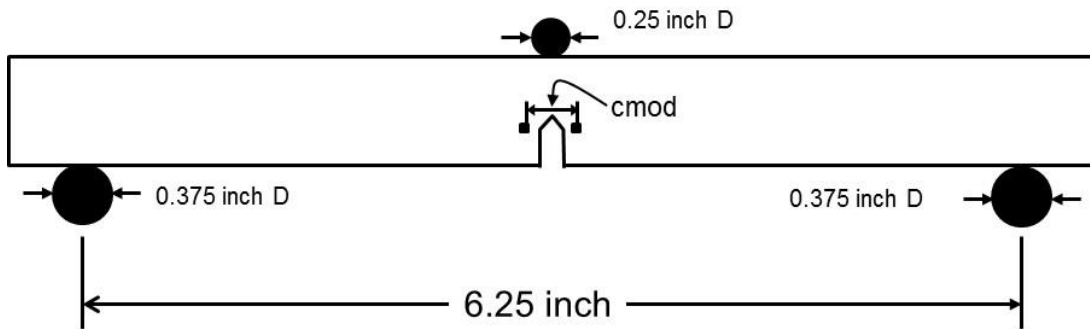
Figure 17. Schematic of 3PTB fixture dimensions.

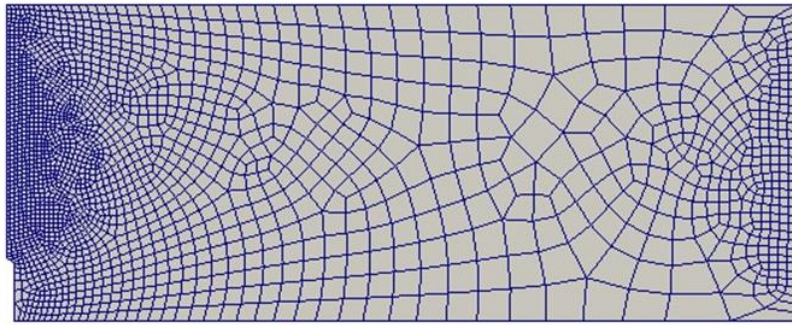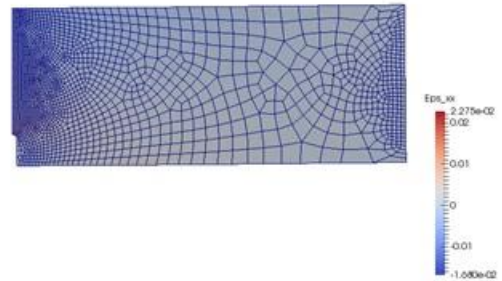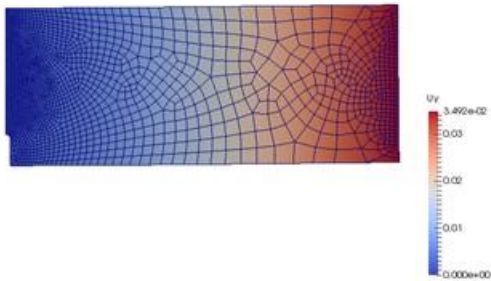*Figure 18. A Typical FE mesh for 3PTB specimen.*

Figure 19. A Typical displacement (in.) and strain contour plot for 3PTB cracked specimen.
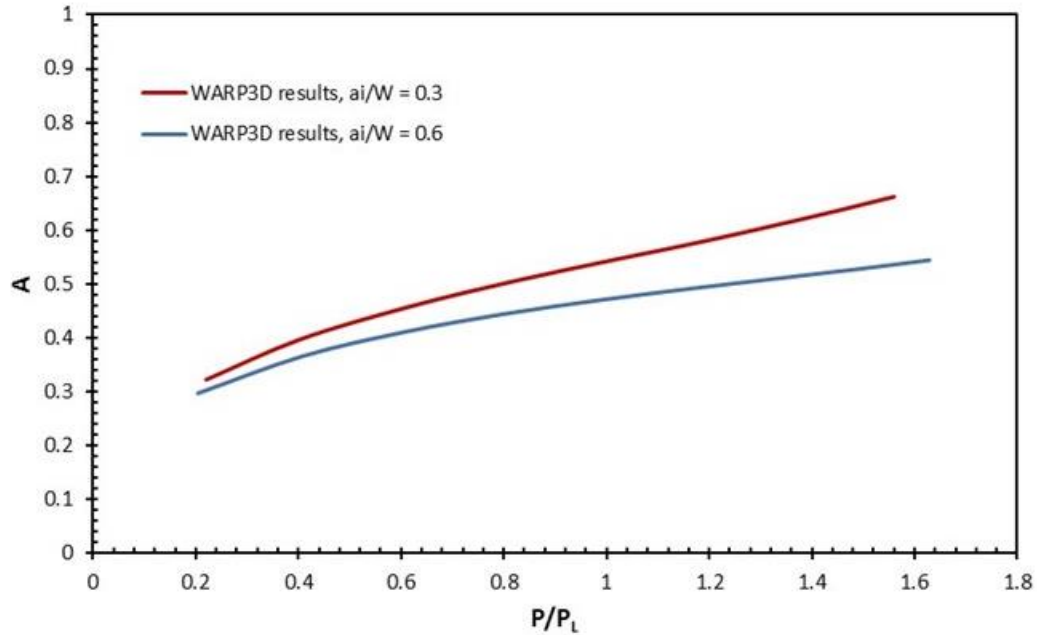
Three Point Bend Specimen n=10 α=0.5

Figure 20. Predicted A from WARP3D analysis for 3PTB specimens.

5.11   Prediction of A for THT Specimen

A typical THT specimen shown in Figure 21 was analyzed using WARP3D. The specimen width was W = 3.0 inches, and the thickness was B = 0.75 inch. The CMOD location measurement is shown in Figure 21. The 3D FE meshes for the THT specimen were created with 3D brick elements. A typical FE mesh used in the WARP3D analyses is presented in Figure 22. Remote tension loading is applied on the model, and the H/W = 4. The typical THT mesh had 20,270 nodes and 15,564 eight noded brick elements. Only a half of the THT specimen was modeled due to symmetries. The 2D plane-strain conditions were simulated with the additional boundary conditions of $u_Z = 0$, on surfaces (i.e., z = 0 and z = B). A separate FEM was generated for each applied load condition to provide sufficient elements in the fracture process zone for the evaluation of the A parameter. A strain and stress contours plots generated using developed Matlab® code are shown in Figure 23. The limit load (stress) σ_L was used to normalize the applied load S for THT specimen. The results of the A parameter solution for a/W = 0.05,
$n = 10$, and α = 0.5 for increasing external load ratio S/σ_L is shown in Figure 24. The predicted value of the A parameter remains constant for values of S/σ_L below 0.4, then increases indicating a loss of constraint with increasing load. Overall, the solution of the A parameter for THT specimen implies that there is drastic variation in constraint at the crack-tip and the loss of constraint is higher with increasing applied S/σ_L value.

3-Hole Tension

0.6 D
(2 places)

cmod

3.00

1.80

0.90

5.20

6.00

6.80

12.00

0.75
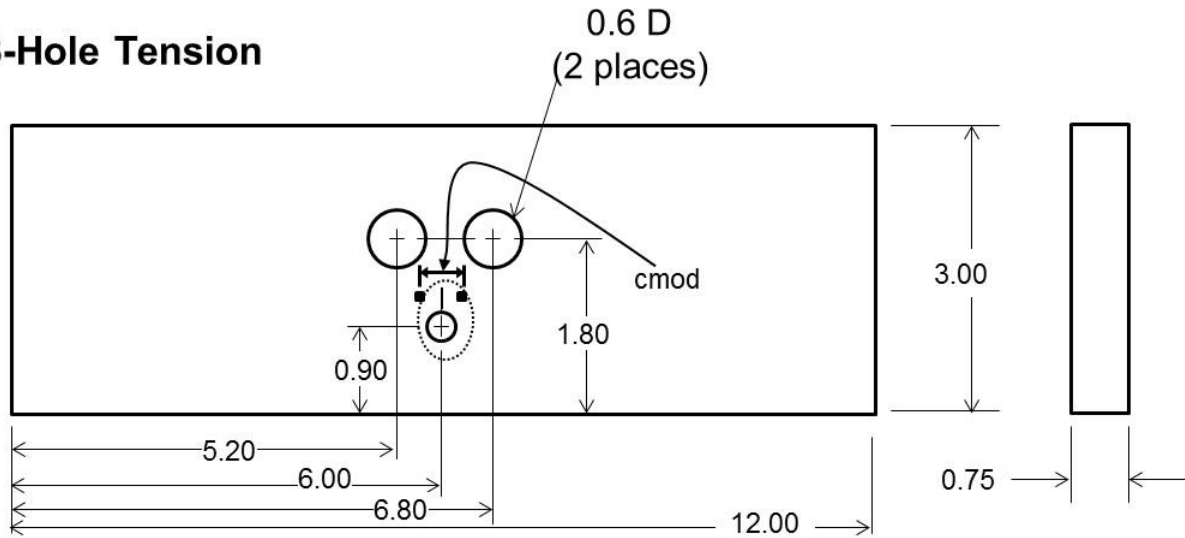
Figure 21. Schematic of THT specimen.

Y

Z   X
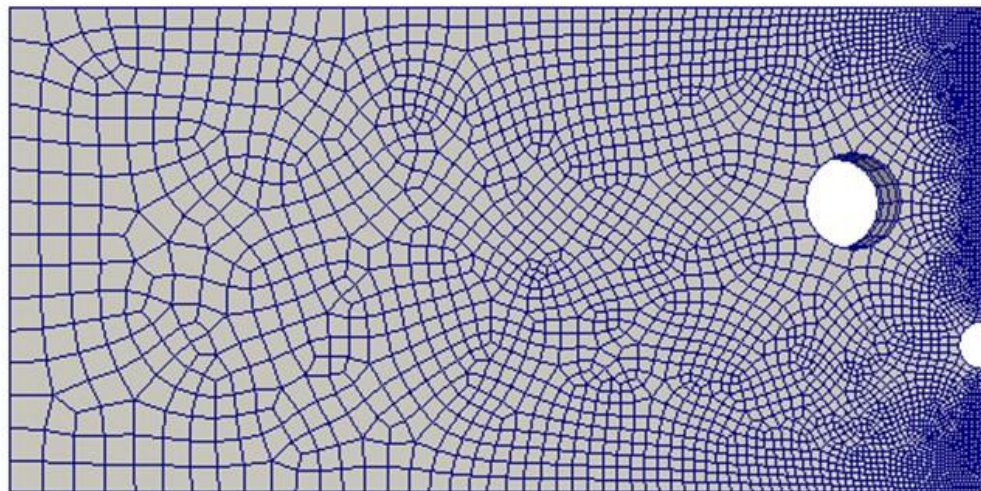
Figure 22. A typical FE mesh for THT specimen.
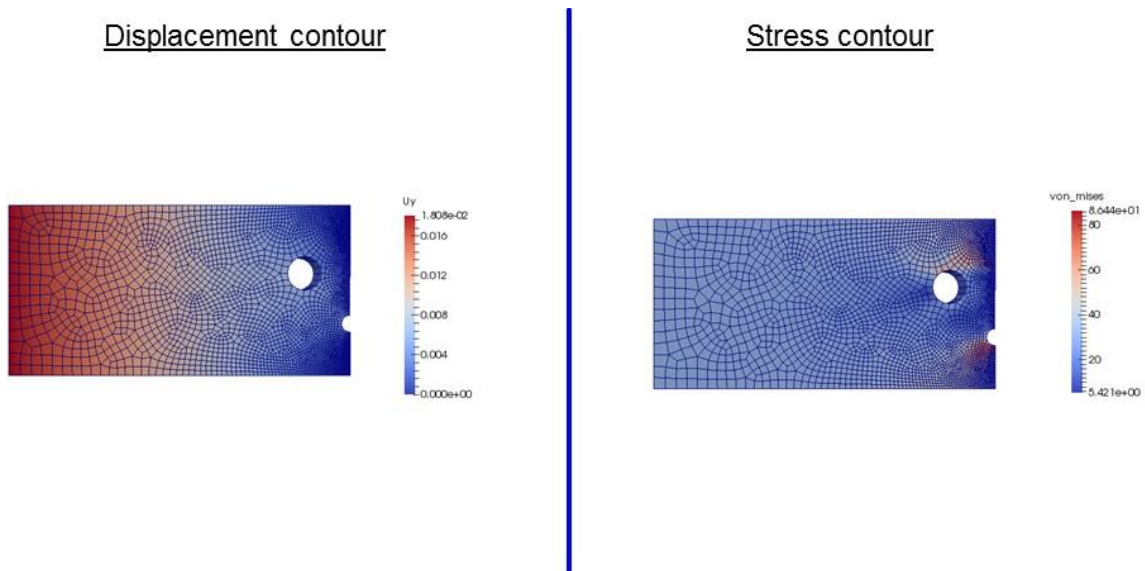
Figure 23. Typical displacement (in.) and stress (ksi) contour plot for THT cracked specimen.
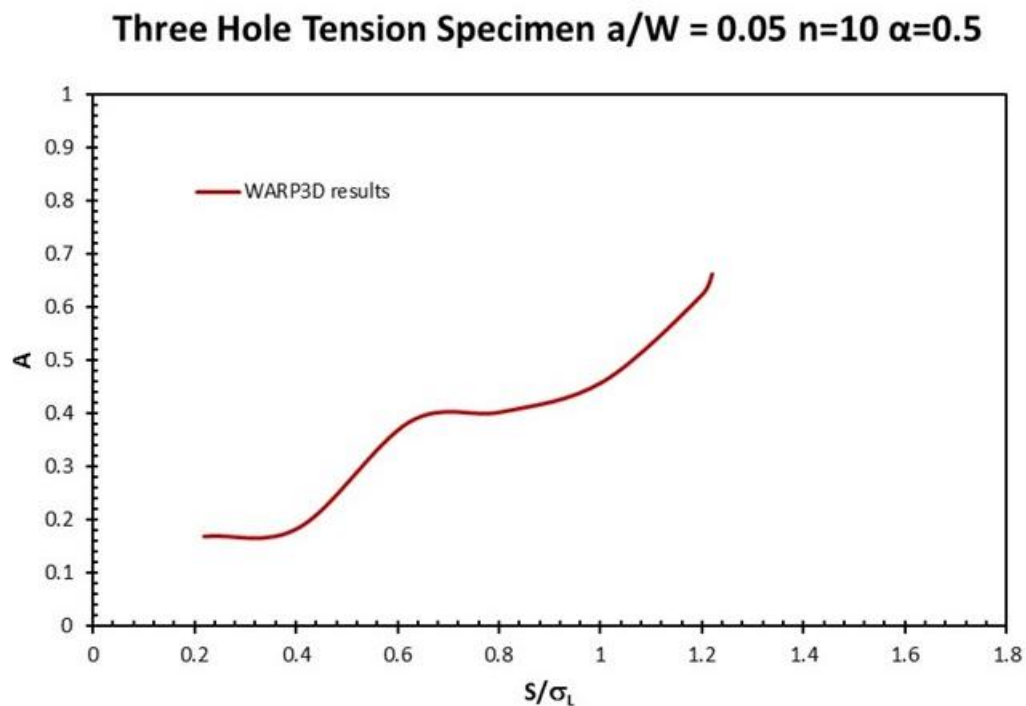
Figure 24. Predicted A from WARP3D analysis for THT cracked specimen.

5.12   Prediction of A Solutions for Part Through Cracks

The methodology that was developed to evaluate the A parameter to study the level of constraint ahead of the crack-tip described in Sections 1.1 and 1.2 is valid under plane strain condition. All the normalized angular stress functions, $\bar{\sigma}_{ij}^{(0)}(\theta)$, $\bar{\sigma}_{ij}^{(1)}(\theta)$, and $\bar{\sigma}_{ij}^{(2)}(\theta)$ evaluated at the crack-tip are for plane strain conditions. For application under 3D part through crack conditions, relationship for angular stress functions have not been developed and thus would have to be

derived before current methodology can be applied under such conditions. This effort was beyond the scope of this assessment.

5.13 Prediction of J-A Solution for THT Specimen

Comparison of variation in the J versus the A parameter is shown in Figure 25 for different initial crack lengths of the THT specimen. J and A increase with applied load. Note that increase in the value of the A parameter at the crack-tip indicates loss of constraint. With further increase in applied load, the relationship between J and A becomes asymptotic. This behavior was observed for all three crack lengths analyzed. The J-A -values that correspond to the failure loads observed in the test are indicated by filled symbols in Figure 25. Tests to determine failure for range of constrains were conducted as described in Appendix B. Failure refers to unstable fracture that occurred at the maximum load observed during the test. By knowing the failure load from the test, corresponding load was applied to the specimen in the numerical simulation. J and A values were estimated from the analysis results and plotted in the Figure 25 as filled symbols. The symbols (i.e., failure points) lie on the asymptotic portion of the curve. This suggests that failure occurs when the variation in J versus A become asymptotic.
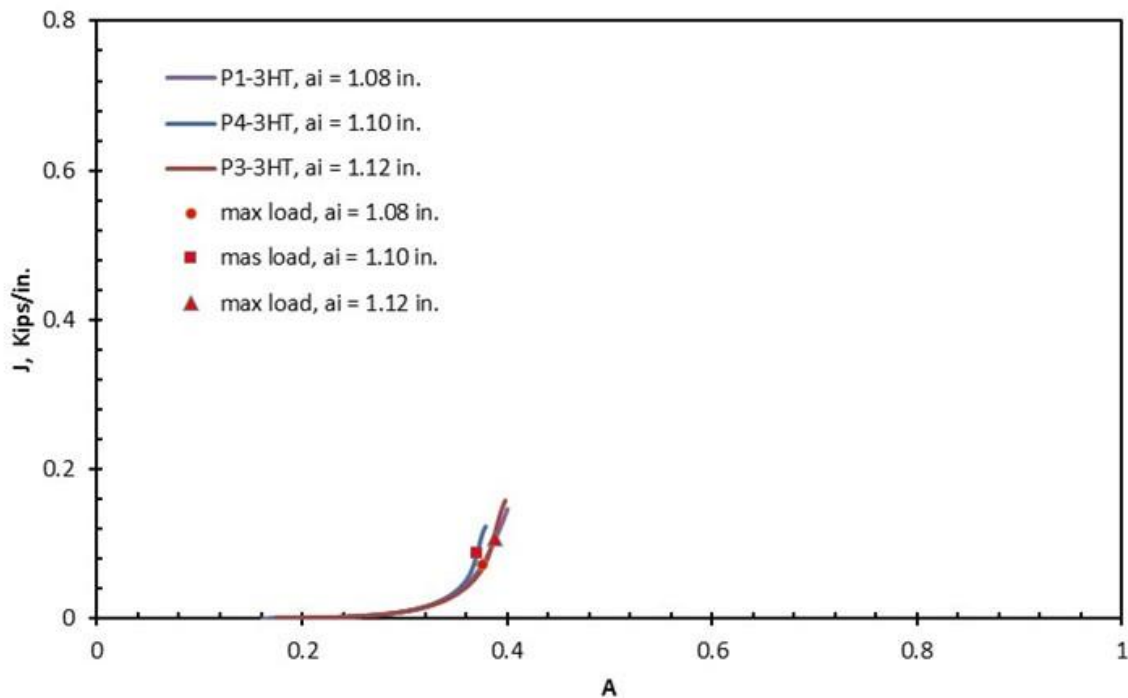
Figure 25. Prediction of J-A solution for THT specimen.

5.14 Prediction of J-A Solution for 3PTB Specimen

The variation in J versus A for a 3PBT specimen with different initial crack lengths is shown in Figure 26. The J-A values that correspond to the failure loads observed in the test are indicated by filled symbols in Figure 26. As with the THT specimen configuration, J and A increase with increasing load, and failure occurs in the asymptotic portion of the curve.
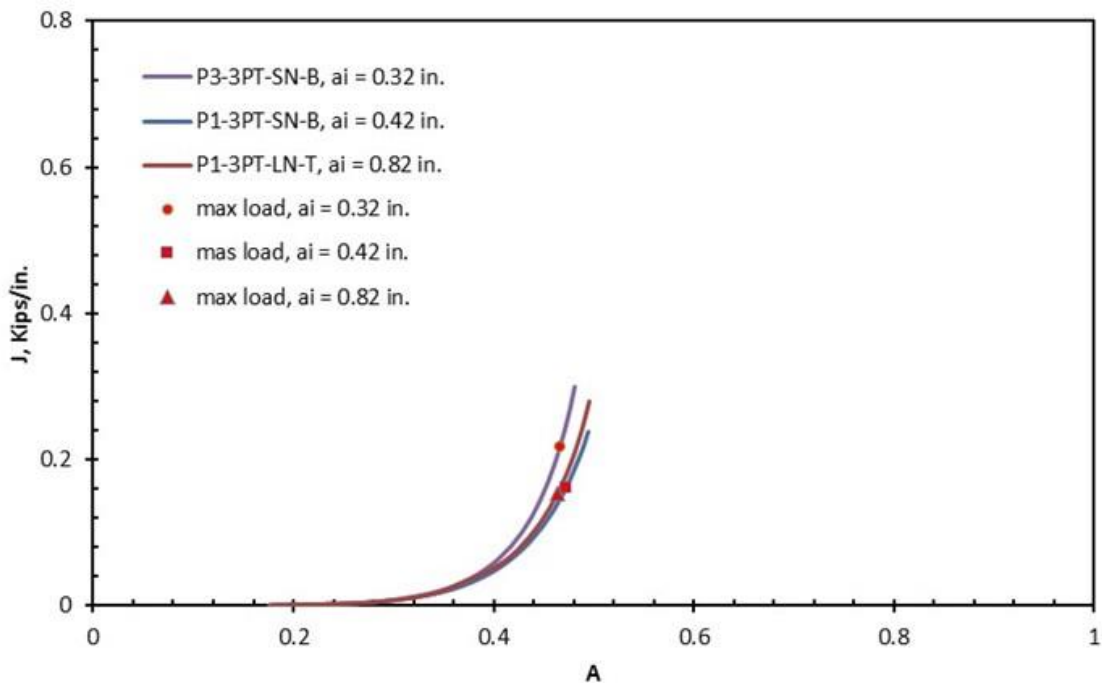
Figure 26. Prediction of J-A solution for 3PTB specimen.

5.15 Prediction of J-A Solution for Different Types of Specimens

Similar to THT and 3PTB specimens, the variation in J versus A was determined for other specimen configurations, and the J-A values determined for the failure loads observed in the tests, as shown in Figure 27. The different specimen configurations have variations in width and crack length, producing a variation in the constraint behavior. The failure point occurred in the asymptotic portion of the J-A curve for all the specimen configurations that were tested. There appears to be a narrow band or range of constraint value A, where all of the specimens fail (i.e., between 0.39 to 0.42). Since the band is relatively narrow, accurate determination of the A parameter is important to characterize or predict the instability of failure. From Figure 27, A appears to be constant at failure for different specimens analyzed but it varies anywhere from 0.38 to 0.44. If J_total_critical and similarly A_critical, a constant value that describes the level of constraint at failure can be defined, then by normalizing J and A, one can come up with a Failure Assessment Diagram (FAD). The envelope defines whether the specimen or coupon is safe or unsafe. If the point is outside, then it is unsafe. This can be explored in the future.
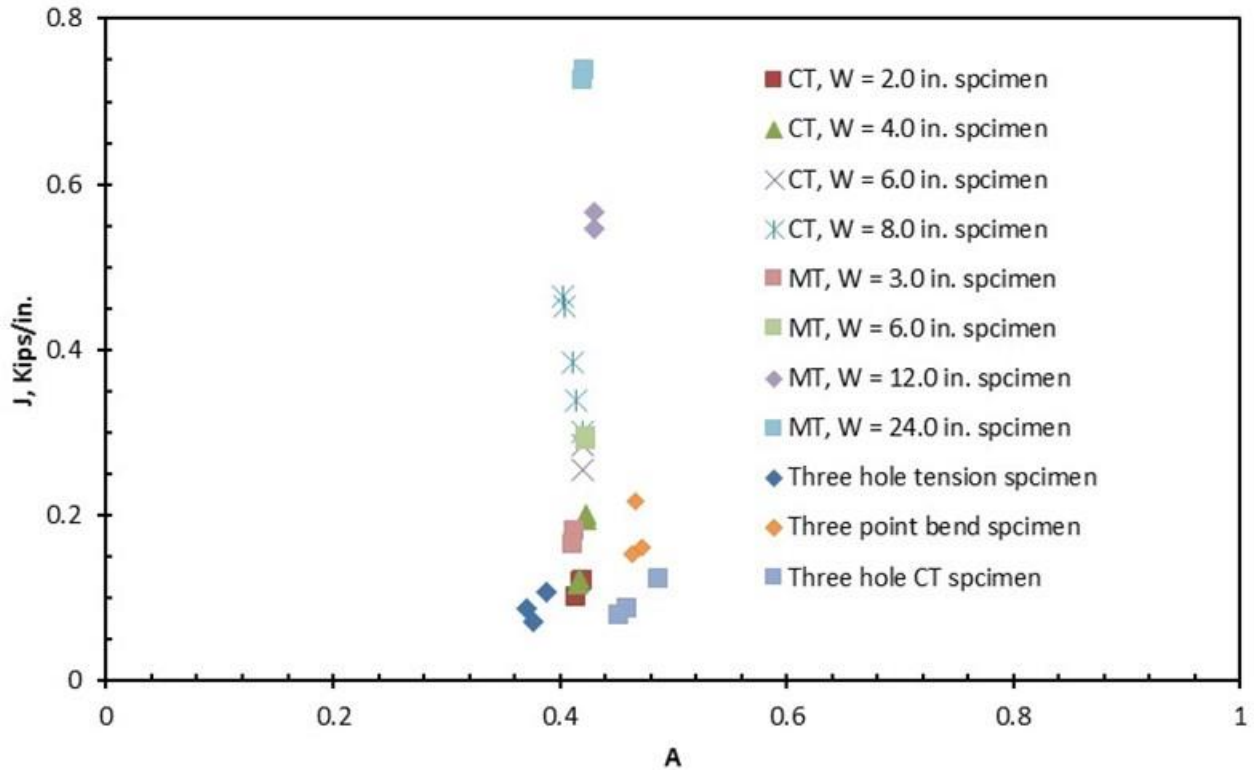
Figure 27. Comparison of J-A parameter for different types of specimens.

5.16   Sensitivity of Failure Load to the A Parameter

The sensitivity of failure load to the A parameter was examined by evaluating at the failure load, 80% of the failure load, and 120% of the failure load, as shown in Figures 28 through 30, respectively. Similarly, the normalized failure load (i.e., predicted failure load divided by the failure load observed in the test) was determined for A values of 0.37, 0.43, and 0.41, as shown in Figures 31 to 33, respectively. As expected from the asymptotic J-A relationship near failure, small changes in the critical value of the A parameter have a strong influence on the predicted failure load. An A value of 0.37 did not capture the influence of specimen size on the failure load, as seen by the variation of the failure loads for the MT and CT specimens shown in Figure 31. Similarly, an A value of 0.43 did not capture the influence of specimen configuration constraint, as seen by the variation in normalized failure loads for the MT and CT specimens shown in Figure 32. From an empirical observation, the choice of an A value of 0.41 appears to best represent the failure loads observed in the tests for all specimen configurations and sizes.
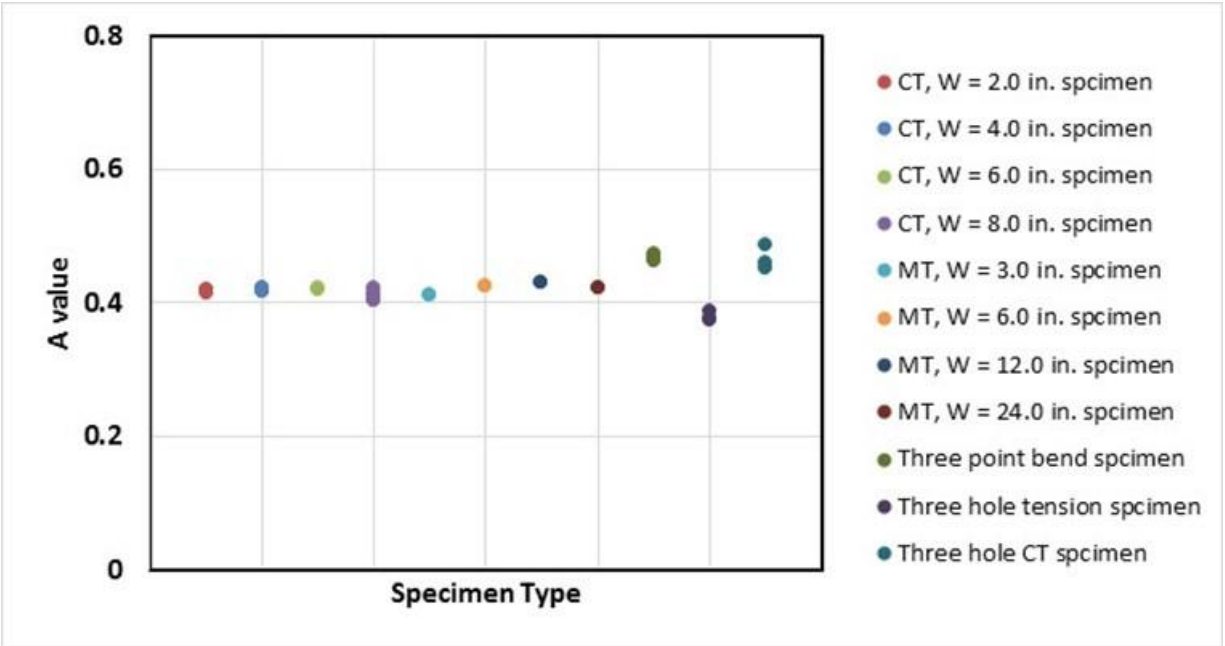
Figure 28. Comparison of A for different specimen types at failure load.
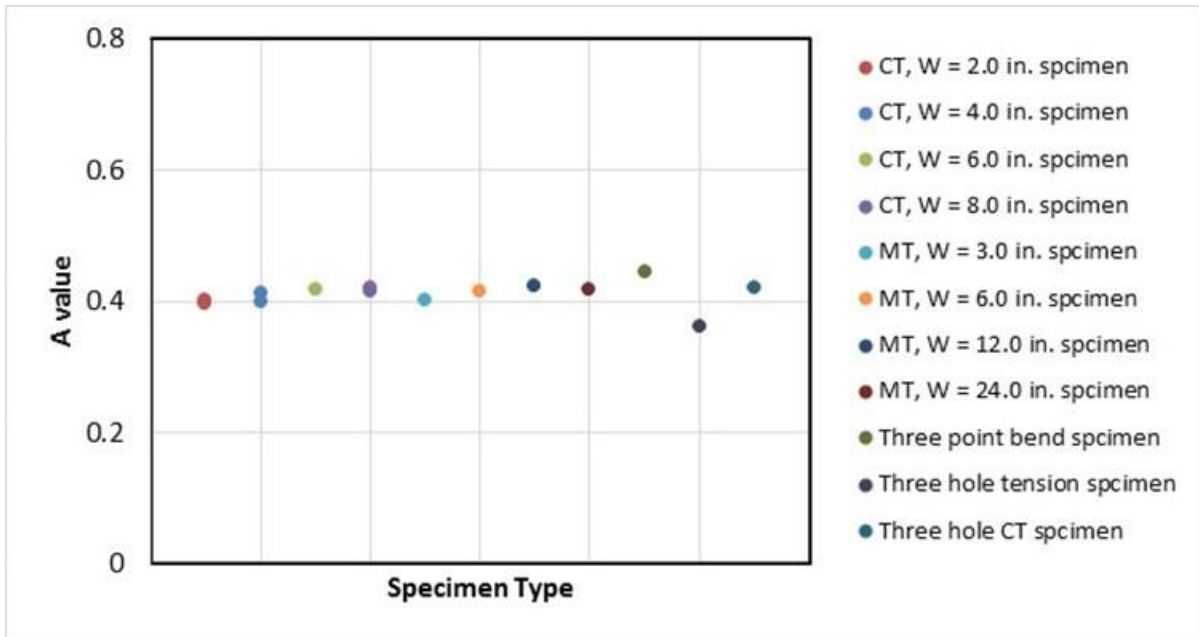
Figure 29. Comparison of A for different specimen types at 80% of failure load.
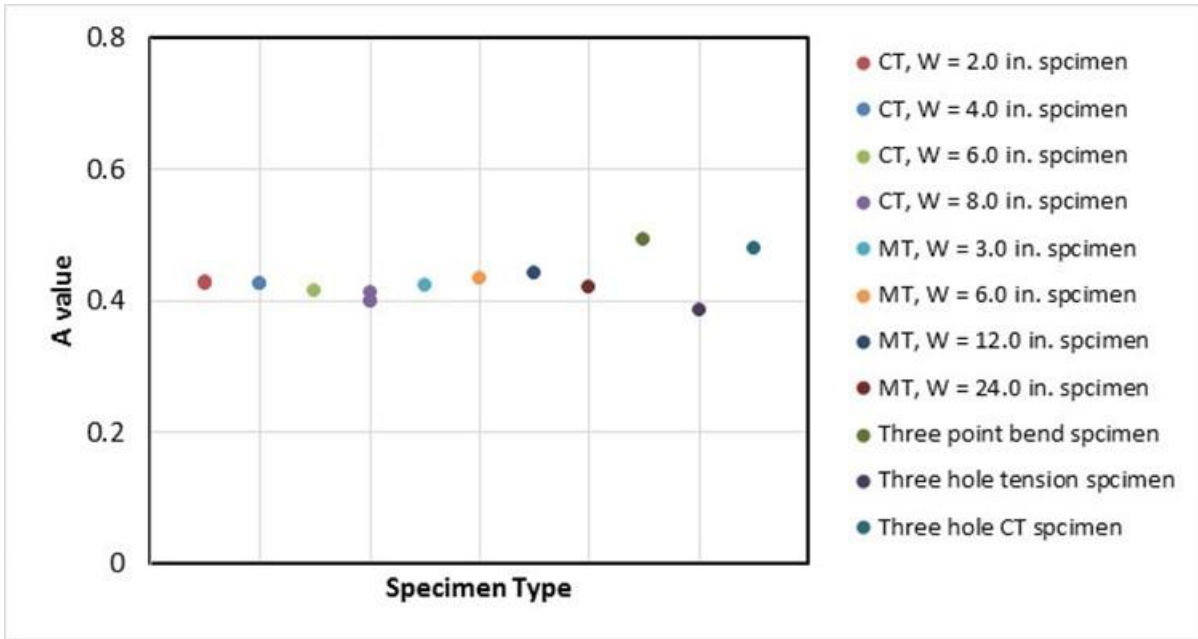
Figure 30. Comparison of A for different specimen types at 120% of failure load.
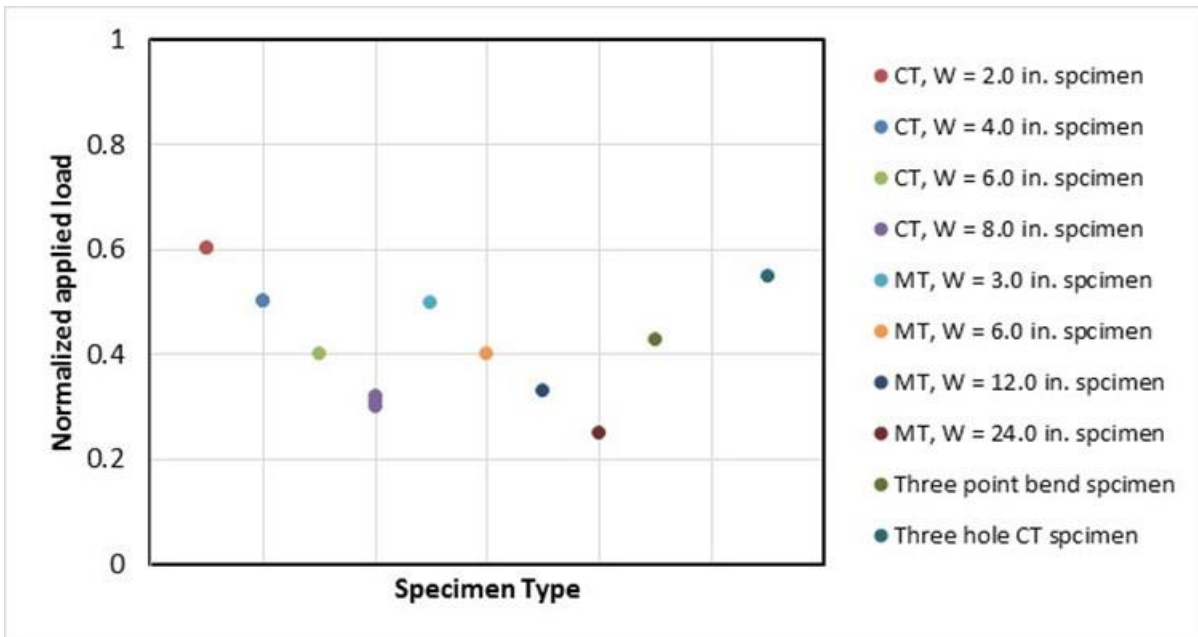
Figure 31. Variation in normalized applied load for different specimen types at A = 0.37.
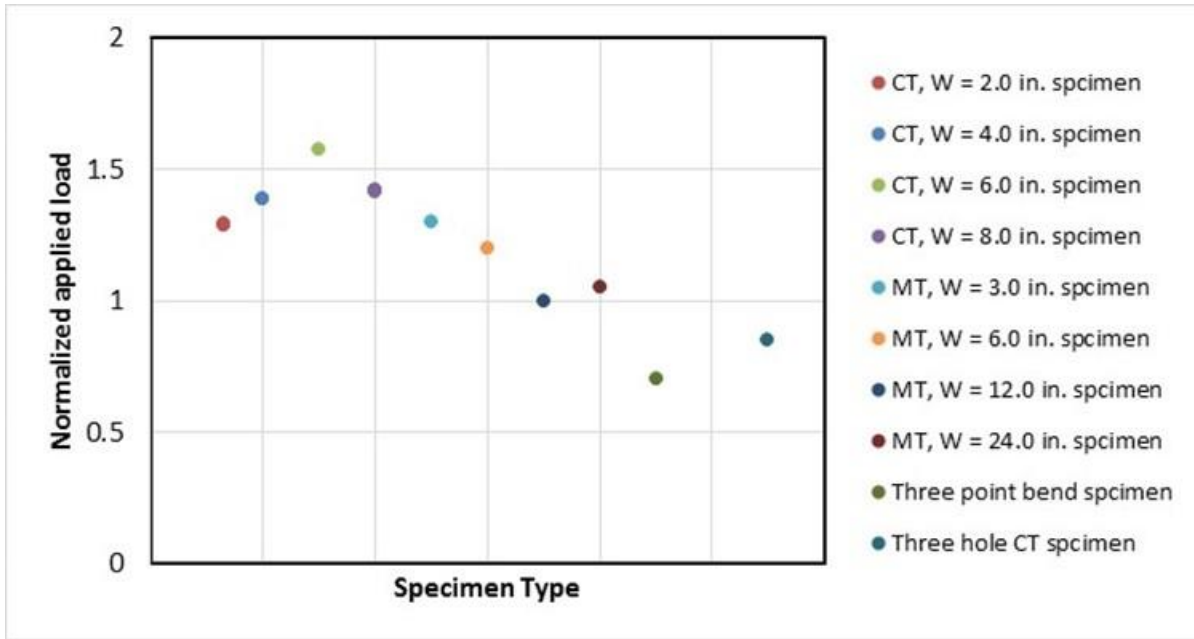
Figure 32. Variation in normalized applied load for different specimen types at A = 0.43.
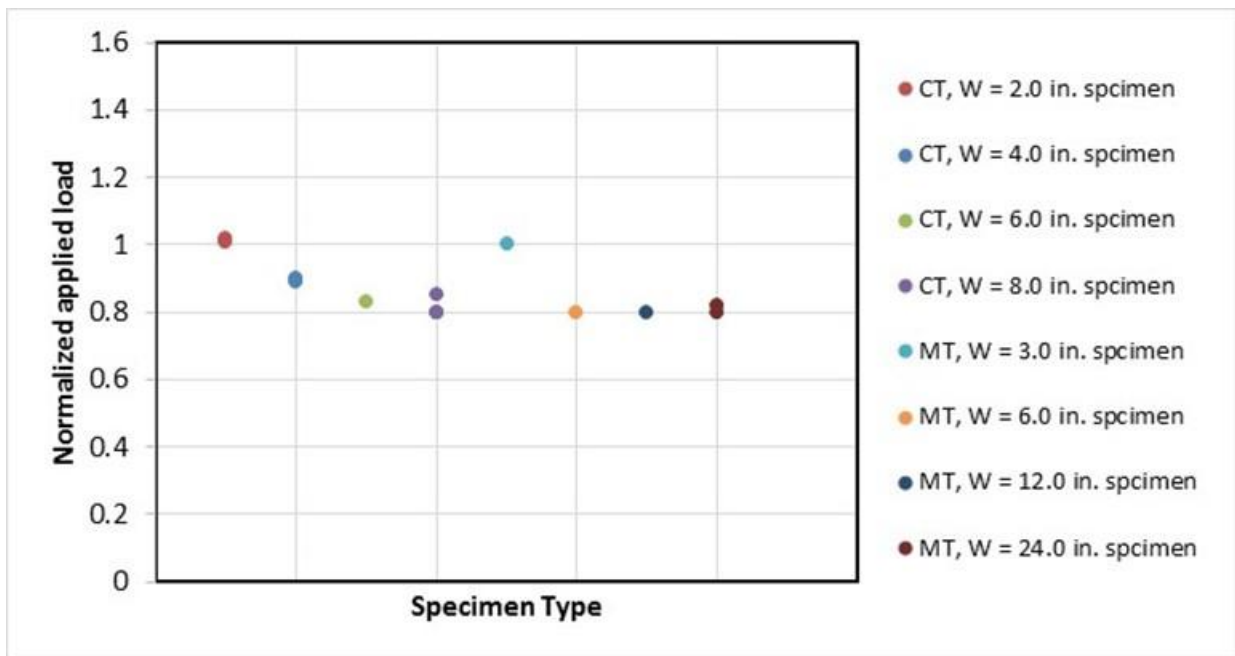
Figure 33. Variation in normalized applied load for different specimen types at A = 0.41.

5.17   Comparison with Other Fracture Prediction Methods

The failure loads predicted using the J-A approach was compared with predictions made with other techniques that have been used in fracture analysis. The techniques examined were: 1) linear elastic fracture toughness, K_C; 2) elastic-plastic J; and 3) elastic-plastic CTOA.

The value of the stress intensity factor, assuming the initial crack length, at fracture was calculated for each test. The values were normalized by the average for all of the tests, as shown in Figure 34. The variation in predicted failure load (i.e., ±40%) illustrates the problem with using linear elastic fracture mechanics for materials that experience ductile fracture. Similarly, the use of the EPFM parameter J, shown in Figure 35, exhibits comparable levels of variation.
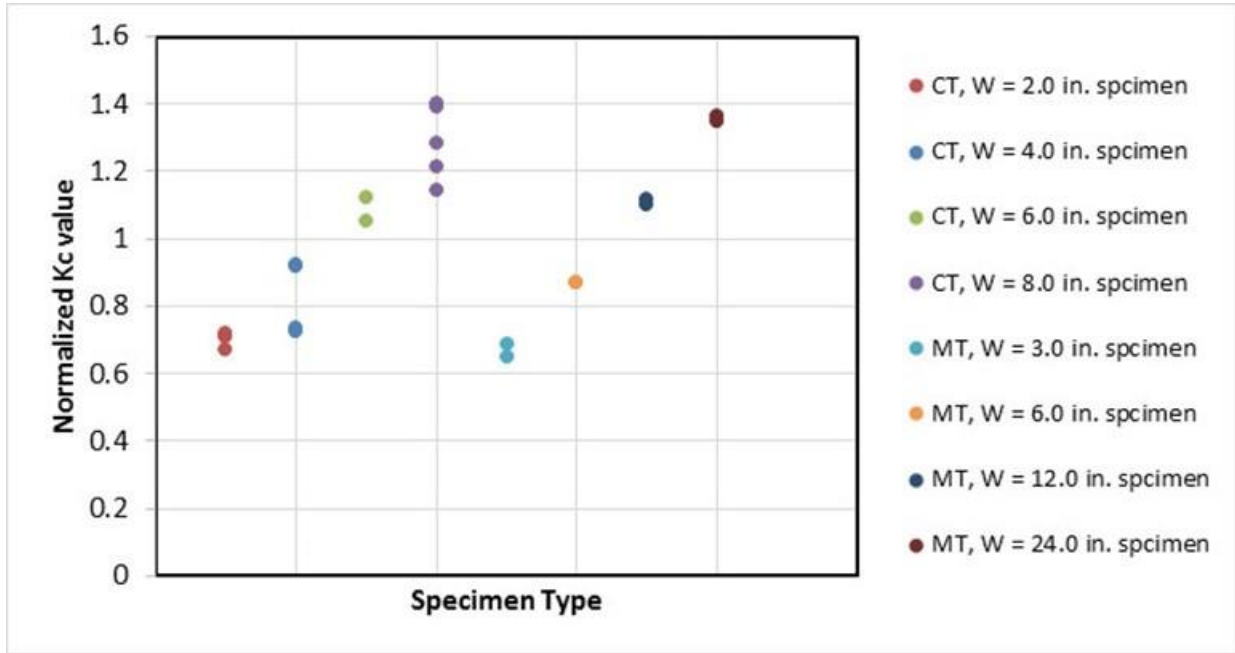
Figure 34. Variation in normalized K_C value for different specimen types.
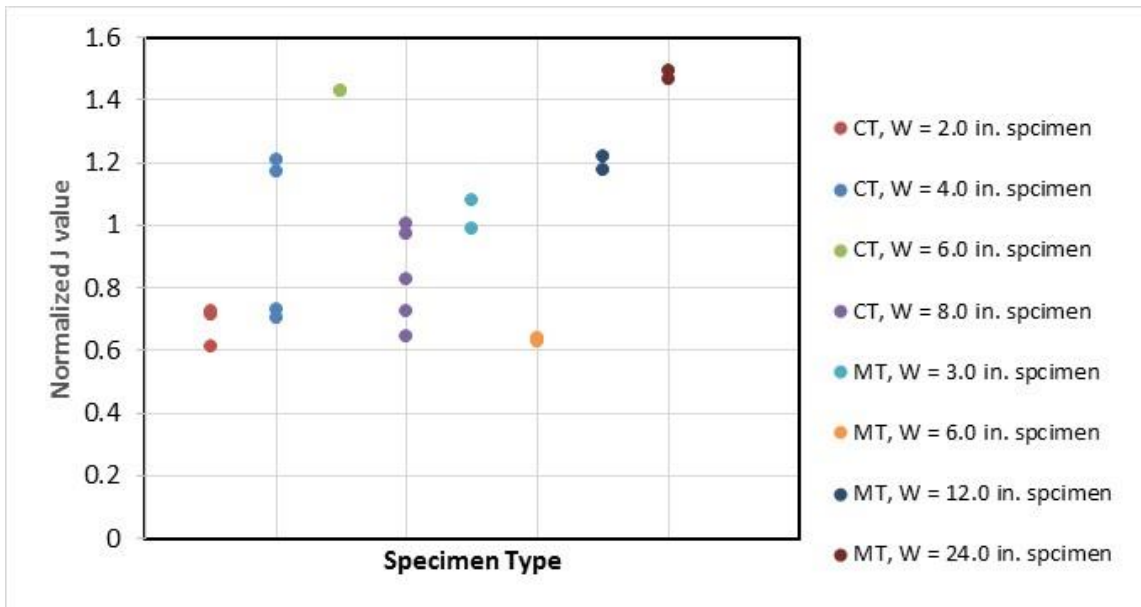
Figure 35. Variation in normalized J values for different specimen types.

The CTOA technique has been used to predict fracture for ductile materials [ref. 31-32] by assuming the crack begins to tear when a critical angle of the crack surfaces is achieved. This technique was used to predict the failure loads for different specimen configurations, as shown in

Figure 36. The scatter in predicted values were similar to that obtained using the J-A fracture criteria with an A value of 0.41, and both the J-A and CTOA methods produced improved predictions (i.e., $\pm20\%$) than K_C or J as shown in Figure 37.
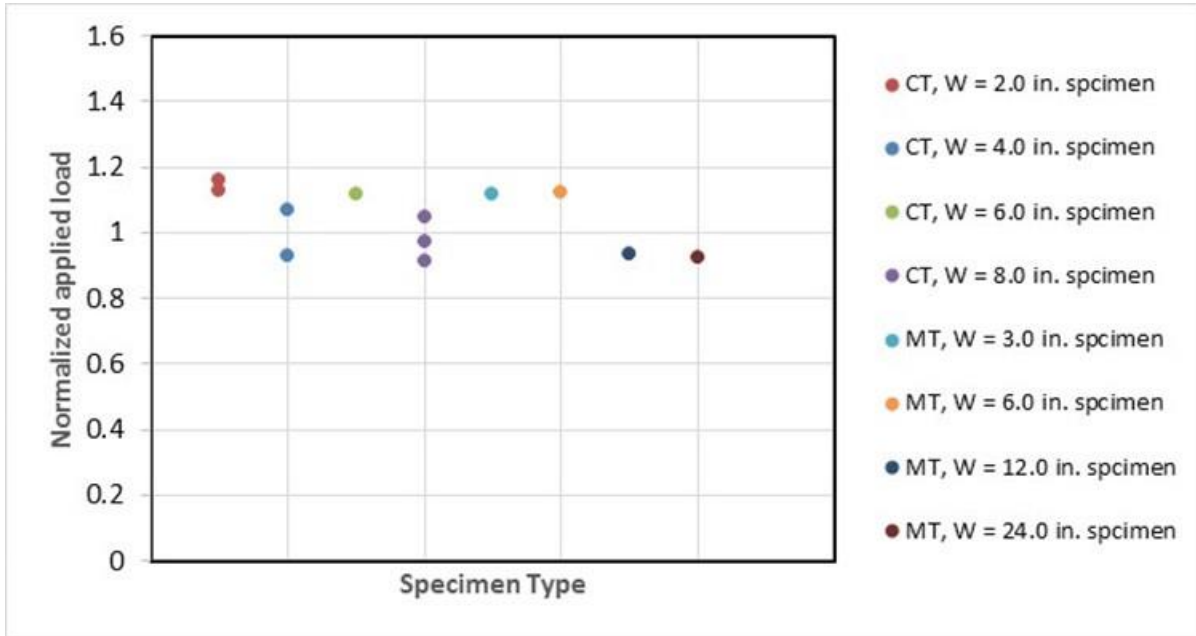
Figure 36. Variation in normalized applied load for different load different specimen types using CTOA criterion.
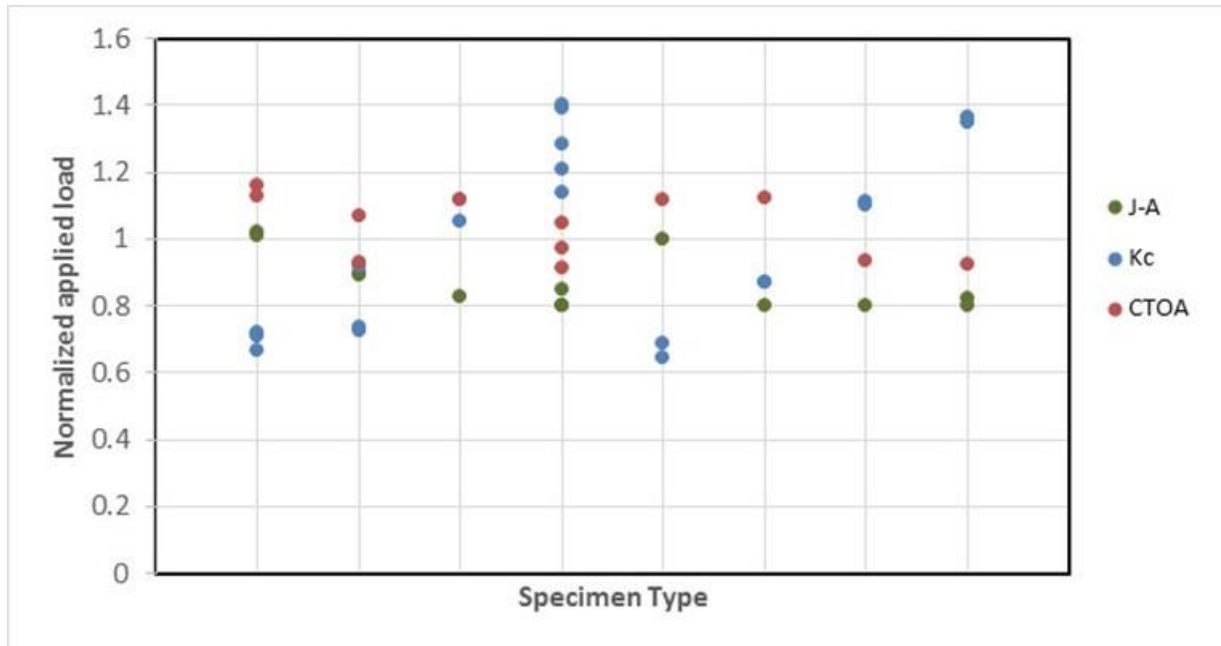
Figure 37. Comparison of variation in normalized applied load for different specimen types using various methods.

5.18   Stable Tearing in Ductile Materials

The ductile aluminum alloy 2024-T3 material was observed to experience stable tearing prior to peak load during some of the fracture tests, as shown in Figure 38. The amount of stable tearing is dependent on the structure size and thickness (i.e., larger, thinner structures experience greater amounts of stable tearing) [refs. 31-32]. The J-A fracture criteria assumes the crack is stationary prior to the maximum load (i.e., fracture). Furthermore, the basic assumptions inherent in the J-integral theory/criterion require a stationary crack; unloading in the region of crack growth is present when stable tearing is present. The J-integral is no longer path independent and the theory breaks down once stable tearing occurs. Thus, the use of a J-A fracture criteria would have to assume that the contribution of energy dissipation due stable tearing would be negligible to the overall toughness of the structure.

a. 5,681 lbs.   b. 5,867 lbs.
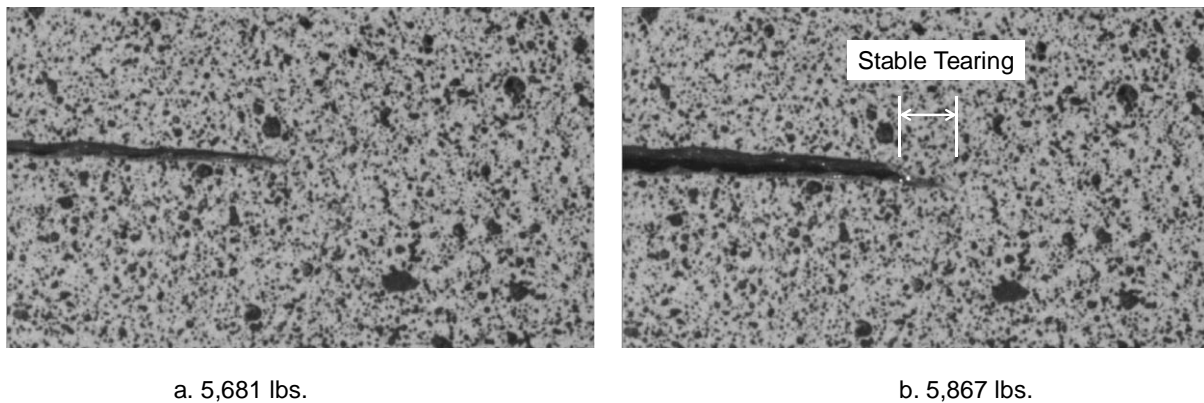
Figure 38.   Example of stable tearing prior to reaching peak load in a 3PCT test.

5.19   Conclusions

This assessment implemented the J-A fracture criteria into the WARP3D EPFM code. This was accomplished by:

- Circular unnotched tensile specimens, notched tension-torsion specimens, 3PTB, THT, and CT specimens were tested as part of the study.

- Implementing a Ramberg–Osgood power-law strain hardening material model relation as a WARP3D UMAT routine.

- Using PARAVIEW/Matlab® software to develop a new capability to view contour plots of displacement vector, strain, and stress tensors on undeformed and deformed geometry was developed to view in 3D format using PARAVIEW software.

- A new capability to determine the constraint parameter A was developed using Matlab® software using least square fit regression analysis capability.

- Extensive elastic–plastic FEAs were conducted to calculate the A parameter for CCP, SECP, and DECP test specimens. The external loading increased from small- to large-scale yielding for those specimens. In addition, the A parameter was predicted for other specimens (e.g., CT, 3PTB, and THT) from small- to large-scale yielding.

6.0 Findings, Observations, and NESC Recommendations

6.1 Findings

The following findings were identified:

F-1. The constraint parameter A varies with specimen type and applied load. Accurate determination of A parameter is crucial in predicting the failure load.

F-2. The constraint parameter A is asymptotic as the failure load is approached, making an accurate determination difficult (i.e., small differences in the A parameter can cause large variations in failure load).

F-3. The failure predictions, for materials exhibiting elastic-plastic behavior, made using the J-A methodology had lower scatter than predictions made using K_C and J methods.

F-4. The scatter observed in failure load for different specimen types using J-A methodology is comparable to the CTOA method.

6.2 Observations

The following observations were identified:

O-1. Comparisons with test data indicated that J methodology alone cannot predict the failure load.

O-2. The J-A methodology requires considerable effort to implement and to evaluate the constraint parameter A for different specimen types and materials.

O-3. The application of J-A methodology to part-through cracks (i.e., 3D problems), encountered in common structural applications, would require considerable effort to derive the local angular stress distributions that already exist for through cracks (i.e., 2D problems).

O-4. The ductile materials may experience stable tearing prior to achieving peak load. The stable tearing violates the stationary crack assumption inherent in the J-integral theory/criterion (deformation theory of plasticity).

6.3 NESC Recommendation

The following NESC recommendation are directed to all NASA and commercial space companies.

R-1. The J-A methodology is currently not mature enough for implementation into flight certification fracture code because:

- The asymptotic nature of the A near fracture requires additional research to develop the proper guidelines for use.

- Additional research is required to extend the approach to complex 3D crack problems.

7.0   Alternative Viewpoints

There were no alternative viewpoints identified during the course of this assessment by the NESC team or the NRB quorum.

8.0   Recommendations for NASA Standards and Specifications

No recommendations for NASA standards and specifications were identified as a result of this assessment.

9.0   Definition of Terms

Corrective Actions   Changes to design processes, work instructions, workmanship practices, training, inspections, tests, procedures, specifications, drawings, tools, equipment, facilities, resources, or material that result in preventing, minimizing, or limiting the potential for recurrence of a problem.

Finding   A relevant factual conclusion and/or issue that is within the assessment scope and that the team has rigorously based on data from their independent analyses, tests, inspections, and/or reviews of technical documentation.

Lessons Learned   Knowledge, understanding, or conclusive insight gained by experience that may benefit other current or future NASA programs and projects. The experience may be positive, as in a successful test or mission, or negative, as in a mishap or failure.

Observation   A noteworthy fact, issue, and/or risk, which may not be directly within the assessment scope, but could generate a separate issue or concern if not addressed. Alternatively, an observation can be a positive acknowledgement of a Center/Program/Project/Organization's operational structure, tools, and/or support provided.

Problem   The subject of the independent technical assessment.

Proximate Cause   The event(s) that occurred, including any condition(s) that existed immediately before the undesired outcome, directly resulted in its occurrence and, if eliminated or modified, would have prevented the undesired outcome.

Recommendation   A proposed measurable stakeholder action directly supported by specific Finding(s) and/or Observation(s) that will correct or mitigate an identified issue or risk.

Root Cause   One of multiple factors (events, conditions, or organizational factors) that contributed to or created the proximate cause and subsequent undesired outcome and, if eliminated or modified, would have prevented the undesired outcome. Typically, multiple root causes contribute to an undesired outcome.

Supporting Narrative   A paragraph, or section, in an NESC final report that provides the detailed explanation of a succinctly worded finding or observation. For example,

the logical deduction that led to a finding or observation; descriptions of assumptions, exceptions, clarifications, and boundary conditions.

10.0   Acronyms and Nomenclature List

2D	2-Dimensional
3D	3-Dimensional
3PCT	Three-Hole Compact Tension
3PTB	Three-Point Bend
CCP	Center Cracked Plate
CMOD	Crack Mouth Opening Displacement
CT	Compact Tension
CTOA	Crack-Tip Opening Angle
DECP	Double Edge-Cracked Plate
EPFM	Elastic-Plastic Fracture Mechanics
HRR	Hutchison-Rice-Rosengren
MSD	Multi-Site Damage
SECP	Single Edge-Cracked Plate
SSY	Small-Scale Yielding
THT	Three-Hole Tension
UMAT	User Material
NAFISS	NASA Fissure

Nomenclature

a	= length of crack in SECT or DECT or half crack length in CCT specimen
$e, f, g, h,$	= coefficients of cubic equation for calculating constraint parameter A from FEA results
e_i, f_i, g_i, h_i	= coefficients of expression on deviation of the asymptotic stress fields from FEA stress calculation for the ith fitting point
A	= constraint parameter (second fracture parameter) in J-A crack-tip fields
A_0, A_1, A_2	= amplitudes of three-term asymptotic expansion for J-A or J-A2 crack-tip fields
B	= Thickness of the specimen
E	= Young's modulus
H	= Height of the specimen
I_n	= scaling integral depending on hardening exponent, n
J	= J-integral
n	= material hardening exponent
P	= applied load on the specimen
P_L	= limit applied load on the specimen
r	= radius in polar coordinates at crack-tip
$\bar{r}$	= dimensionless radius in polar coordinates at crack-tip
$\bar{\bar{r}}_i$	= dimensionless radius in polar coordinates at crack-tip for the ith point
s, t	= powers in J-A crack-tip fields
w_i	= weight for the ith fitting element
W	= width of the specimen
x, y, z	= Cartesian co-ordinates

α	= material coefficient in Ramberg-Osgood relationship
δ_i	= deviation of asymptotic stress fields from the FEA stress solution for i[th] fitting point
ε_{ij}	= strain components
ε_o	= yield strain
θ	= angle in polar coordinates at the crack-tip
θ_i	= angle in polar coordinates at the crack-tip for the ith fitting point
S	= remote tension stress applied on the boundary of the specimen
σ_{ij}	= stress components
σ_o	= yield stress
σ_{FEM}	= stress valued from finite element analysis
$\bar{\sigma}_{ij}^{(0)}, \bar{\sigma}_{ij}^{(1)}$	= dimensionless angular stress functions in J-A crack-tip fields
$\bar{\sigma}_{ij}^{(2)}$	= dimensionless angular stress functions in J-A crack-tip fields
σ_L	= limit load on the specimen
ν	= Poisson's ratio

11.0 References

1. Rice J. R., A Path Independent Integral and the Approximate Analysis of Strain Concentration by Notches and Cracks. J Appl Mech 1968; 35:379–86.
2. Hutchinson J. W., Singular Behavior at the End of a Tensile Crack in a Hardening Material. J Mech Phys Solids 1968; 16:13–31.
3. Rice J. R., Rosengren GF. Plane Strain Deformation Near a Crack-Tip in a Power Law Hardening Material. J Mech Phys Solids 1968; 16:1–12.
4. Li Y. C., Wang TC. Higher-order Asymptotic Field of Tensile Plane-strain Nonlinear Crack Problem. Sci Sin (Ser A) 1986; 29:941–55.
5. Sharma S. M., Aravas N. Determination of Higher-order Terms in Asymptotic Elastoplastic Crack-tip Solutions. J Mech Phys Solids 1991; 39:1043–72.
6. Betegon C, Hancock J. W., Two Parameter Characterization of Elastic-plastic Crack-tip Fields. J Appl Mech 1991; 58:104–10.
7. Al-Ani A.M., Hancock J.W., J-Dominance of Short Cracks in Tension and Bending. J Mech Phys Solids 1991; 39:23–43.
8. Du Z. Z., Hancock J. W., The Effect of Non-singular Stress on Crack-tip Constraint. J Mech Phys Solids 1991; 39:555–67.
9. Williams M. L., On the Stress Distribution at the Base of a Stationary Crack. J Appl Mech 1957; 24:109–14.
10. O'Dowd N. P., Shih C.F., Family of Crack-tip Fields Characterized by a Triaxiality Parameter – I. Structure of fields. J Mech Phys Solids 1991; 39:989–1015.
11. O'Dowd N. P., Shih C.F., Family of Crack-tip Fields Characterized by a Triaxiality Parameter – II. Fracture Applications. J Mech Phys Solids 1992; 40:939–63.
12. Yang S. Higher Order Asymptotic Crack-tip Fields in a Power-law Hardening Material. PhD dissertation, University of South Carolina, USA; 1993.
13. Yang S., Chao Y. J., Sutton MA. Higher-order Asymptotic Fields in a Power-law Hardening Material. Engng Fract Mech 1993; 45:1–20.

14. Nikishkov G. P., An Algorithm and a Computer Program for the Three-term Asymptotic Expansion of Elastic-plastic Crack-tip stress and Displacement Fields. Eng Fract Mech 1995; 50:65–83.
15. Nikishkov G. P., Bruckner-Foit A, Munz D., Calculation of the Second Fracture Parameter for Finite Cracked Bodies using a Three-term Elastic–plastic Asymptotic Expansion. Engng Fracture Mechanics, 1995; 52:685–701.
16. Ainsworth R. A., Sattari-Far I, Sherry A. H., Hooton D. G., and Hadley I., Methods for including Constraint Effects within SINTAP Procedures. Engng Fract Mech 2000; 67:563–71.
17. Kfouri A. P., Some Evaluation of the Elastic T-term using Eshelby's Method. Int J Fract 1986; 30:301–15.
18. Nakamura T, Parks D. M., Determination of Elastic T-stress along Three-dimensional Crack Fronts using an Interaction Integral. Int J Solids Struct 1992; 29:1597–611.
19. Wang X., Elastic T-stress for Cracks in Test Specimens subjected to Non-uniform Stress Distributions. Engng Fract Mech 2002; 69:1339–52.
20. Wang X., Elastic T-stress Solutions for Semi-elliptical Surface Cracks in Finite Thickness Plates. Engng Fract Mech 2003; 70:731–56.
21. Yu X., and Wang X., Weight Functions for T-stress for Semi-elliptical Surface Cracks in Finite-thickness Plates. J Strain Anal Engng Des 2005; 40:403–19.
22. Wang X., Elastic T-Stress Solutions for Penny-shaped Cracks under Tension and Bending. Engng Fract Mech 2004; 71:2283–98.
23. O'Dowd N. P., Applications of Two Parameter Approaches in Elastic–Plastic Fracture Mechanics. Engng Fract Mech 1995; 52:445–65.
24. Gullerud A. S., Dodds Jr R. H., J–Q and Toughness Scaling Model Solutions for M(T), DE(T), SE(B) and C(T) Specimens. Int J Fract 1995; 72:R11–21.
25. Wu S. and Mai Y., Cotterell B. Q Solutions for Compact Tension and Single-Edge Cracked Tension Specimens. Int J Fract 1995; 68:R97–R103.
26. Wang X., Two-parameter Characterization of Elastic–Plastic Crack Front Fields: Surface Cracked Plates under Tensile Loading. Engng Fract Mech 2009; 76:958–82.
27. WARP3D Manual, Release 17.6.0, 3-D Dynamic Nonlinear Fracture Analyses of Solids Using Parallel Computers. January 20 2016, http://www.warp3d.net
28. Ahrens, James, Geveci, Berk, Law, Charles, *ParaView*: An End-User Tool for Large Data Visualization, Visualization Handbook, Elsevier, 2005, ISBN-13:978-0123875822.
29. Math Works, http://www.mathworks.com
30. Anderson T. L., Fracture Mechanics: Fundamentals and Applications. Boca Raton: CRC Press; 2005.
31. Newman, J. C. Jr., Dawicke, D. S. and Seshadri, B. R., "Residual Strength Analyses of Stiffened and Un-Stiffened Panels – Part I: Laboratory Specimens," Engng. Fract. Mech., 70, 2003, 493-507.
32. Seshadri, B. R., Newman, J. C. Jr. and Dawicke, D. S., "Residual Strength Analyses of Stiffened and Un-Stiffened Panels – Part II: wide panels," Engng. Fract. Mech., 70, 2003, 509-524.
33. Irwin, G.R., Analysis of Stresses and Strains Near the End of a Crack Traversing a Plate, J. Appl. Mech. 24 (1957) 361–364.
34. Broek, D., Elementary Engineering Fracture Mechanics, Sijthoff and Noordhoff, 1978.

35. Eshelby, J. D., "The Continuum Theory of Lattice Defects," Solid State Physics, Vol.3, 1956, 79-144.
36. Cherepanov, G. P., "On Crack Propagation in Solids," Int. J. Solids Struct, Vol. 5, 1969, 863-871.
37. Shawn, A. E., Nagaraj, K. A., and Phillip, A. A., "J-T Characterized Stress Fields of Surface-Cracked Metallic Liners Bonded to a Structural Backing – I. Uniaxial Tension," Engng. Fract. Mech., 77, 2010, 170-181.
38. Shawn, A. E., "J-T and J-Q Characterization of Surface Crack Tip Fields in Metallic Liners under Large-Scale Yielding," PhD dissertation, Univ. of Florida, 2011.
39. Wang, Y. Y., "On the Two-Parameter Characterization of Elastic-Plastic Crack-front fields in surface-cracked plates," Constraint Effects in Fracture, ASTM STP 1171, 120-138.
40. O'Dowd N. P., Shih C.F., Two-Parameter Fracture Mechanics: Theory and applications, Fracture Mechanics: 24th Vol., ASTM STP 1207, 21-47.
41. Silva, L.A. L., Cravero, S. and Ruggieri, C., "Correlation of Fracture behavior in high Pressure Pipelines with axial flaws using Constraint designed test specimens. Part II: 3D effects on constraint," Engng. Fract. Mech., 73, 2006, 2123-2138

Appendices

Appendix A. Crack-Tip Stress Fields, J-integral, HRR Field CTOA and Two-Parameter J-T and J-Q Details

A-1. Stress Field around a Crack-tip

Brittle fracture in a solid in the form of crack growth is governed by the stress field around the crack-tip and by parameters that describe the resistance of the material to crack growth. Thus, the analysis of stresses near the crack-tip constitutes an essential part of fracture mechanics. For brittle materials exhibiting linear elastic behavior, methods of elasticity are used to obtain stresses and displacements in cracked bodies. These methods include analytical ones, such as the complex potential function method and the integral transform method, and numerical ones, such as the FE method. The characteristics of the near-tip asymptotic stress and displacement fields and the crack growth criterion based on the crack-tip field are discussed. A crack in a solid consists of disjoined upper and lower faces. The joint of the two crack faces forms the crack front. The two crack faces are usually assumed to lie in the same surface before deformation. When the cracked body is subjected to external loads (remotely or at the crack surfaces), the two crack faces move with respect to each other and these movements may be described by the differences in displacements ux, uy, and uz between the upper and lower crack surfaces, where (x, y, z) is a local Cartesian coordinate system centered at the crack front with the x-axis perpendicular to the crack front, the y-axis perpendicular to the crack plane as shown in Figure A.1.
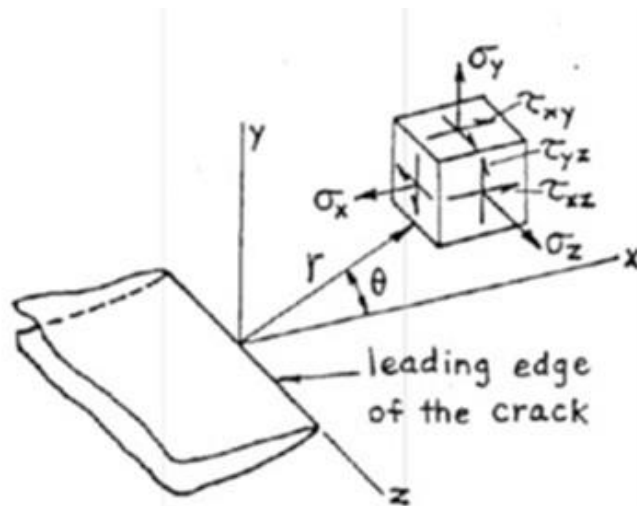

Figure A.1. Schematic of crack-tip stress field.

There are three independent fundamental fracture modes as pointed out by Irwin [ref. 33], and these are schematically illustrated in Figure A.2. The basic fracture modes are Mode I, Mode II, and Mode III, and any fracture mode in a cracked body can be described by one of the three basic modes, or their combinations.
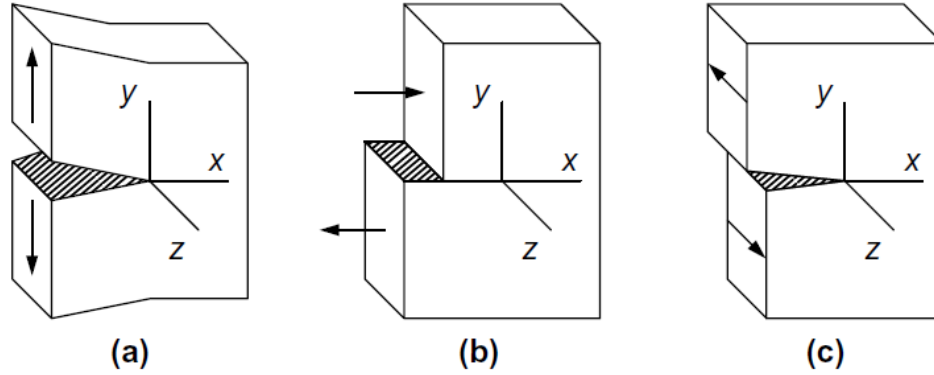
Figure A.2. Schematic of the basic fracture modes (a) Mode I (opening), (b) Mode II (sliding), and (c) Mode III (tearing).

1. *Mode I (Opening Mode)*: The two crack surfaces experience a jump only in *uy*, that is, they move away symmetrically with respect to the undeformed crack plane (*xz*-plane).

2. *Mode II (Sliding Mode)*: The two crack surfaces experience a jump only in *ux*, that is, they slide against each other along directions perpendicular to the crack front, but in the same undeformed plane.

3. *Mode III (Tearing Mode)*: The two crack surfaces experience a jump only in *uz*, that is, they tear over each other in the directions parallel to the crack front but in the same undeformed plane.

The stresses ahead of the crack front can be expressed (refer Figures A.1)

$$\sigma_{xx} = \frac{K_I}{(2\pi r)^{1/2}} \cos\frac{\theta}{2}\left[1 - \sin\frac{\theta}{2}\sin\frac{3\theta}{2}\right] + O(r^{1/2}) \tag{A-1}$$

$$\sigma_{yy} = \frac{K_I}{(2\pi r)^{1/2}} \cos\frac{\theta}{2}\left[1 + \sin\frac{\theta}{2}\sin\frac{3\theta}{2}\right] + O(r^{1/2}) \tag{A-2}$$

$$\tau_{xy} = \frac{K_I}{(2\pi r)^{1/2}} \sin\frac{\theta}{2}\cos\frac{\theta}{2}\cos\frac{3\theta}{2} + O(r^{1/2}) \tag{A-3}$$

$$\tau_{xy} = \frac{K_{II}}{(2\pi r)^{1/2}} + O(r^{1/2}) \tag{A-4}$$

$$\tau_{yz} = \frac{K_{III}}{(2\pi r)^{1/2}} + O(r^{1/2}) \tag{A-5}$$

where the three parameters, K_I, K_{II}, and K_{III} are called stress-intensity factors corresponding to the opening, sliding and tearing modes of fractures, respectively. These expressions show that the stresses have an inverse square root singularity at the crack-tip and the stress intensity factors

K_I, K_{II}, and K_{III} denote the severity of the stress fields of opening, in-plane shearing, and anti-plane shearing, respectively.

A-2.   J-Integral

By considering a small strain analysis, any deformation induced blunting of the crack-tip is neglected. Using J_2 deformation theory of plasticity (equivalent to nonlinear elasticity), the reversible stress-strain response is depicted schematically in Figure A.3.
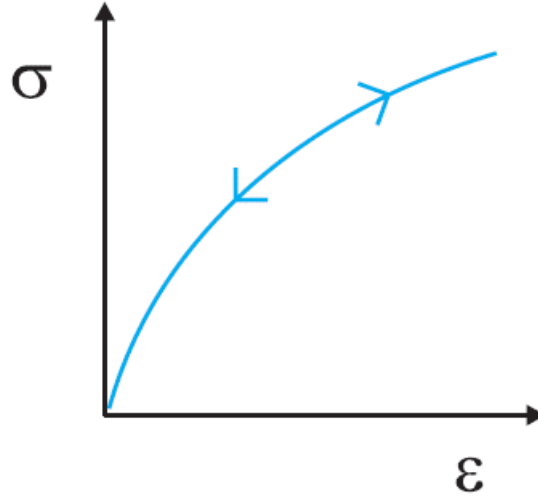

Figure A.3. Stress-strain response – J₂ deformation theory of plasticity.

J-integral was proposed by Eshelby [ref. 35] and later for crack problems by Rice [refs. 1, 30, 34] and Cherepanov [ref. 36]. The integral can be written as

$$J = \int_\Gamma \left(W \, dy - T \cdot \frac{\partial u}{\partial x} \, ds \right)$$

(A-6)

where, $W = W(x,y) = W(\varepsilon) = \int_0^\epsilon \sigma_{ij} \, d\varepsilon_{ij}$

with Γ is a closed contour integral followed counter clockwise (see Figure A.4) in a stressed solid, T is the tension (traction) vector perpendicular to Γ, $T = \sigma_{ij} \, n_j$, where n is the outward drawn normal to Γ, u is the displacement in the x direction and ds is an element of Γ, W in Eq. (A-6) is the strain energy per unit volume. J around a closed contour without any singularities is identically zero. J is also a path independent around a crack-tip.

Rice demonstrated that the J-integral around a crack-tip (see Figure A.4) is the change in potential energy for a virtual crack extension da:
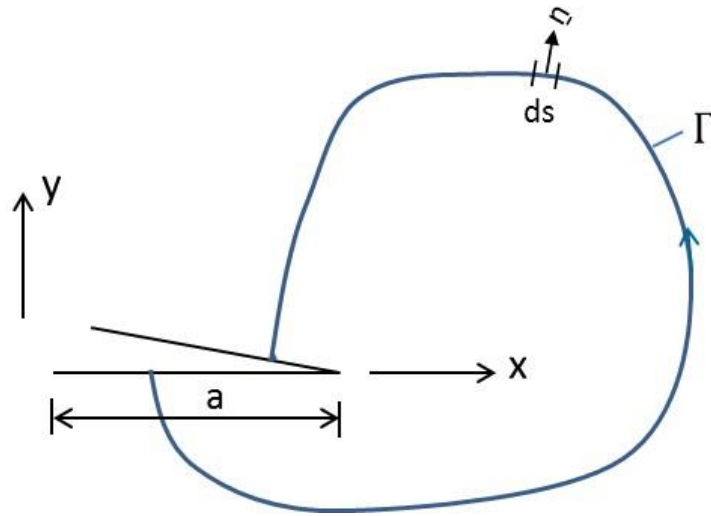
Figure A.4. Schematic representation of J-integral around the crack-tip.

$$J = -\frac{\partial V}{\partial a} \tag{A-7}$$

where V is the potential energy.

For a linear elastic material, $-\frac{\partial V}{\partial a} = G$, the strain energy release rate; thus J = G.

Thus for linear elastic materials,

$$J = G = \frac{K^2}{E}(1 - v^2) \tag{A-8}$$

For proportional loading J_2 deformation theory and J_2 flow theory (incremental theory of plasticity) give results that are comparable (i.e., for monotonic loading, stationary cracks). Not appropriate for situations where significant unloading occurs. The total mechanical potential energy of the cracked body is, U_M

$$U_M = U_e + U_{app} \tag{A-9}$$

U_M represents the sum of the stored strain potential energy and the potential energy of the applied loading.

$$U_M = \int_A w\, dA - \int_S T \cdot u\, ds \tag{A-10}$$

where, w = strain energy density (per unit volume) and $\sigma_{ij} = \frac{\partial w}{\partial \epsilon_{ij}}$,

dA is element of cross-section A within S. Now by evaluating the derivative of the mechanical potential energy, U_M with respect to crack length,

$$-\frac{dU_M}{da} = \int_S \left(w \, dy - T \cdot \frac{\partial u}{\partial x} \, ds \right) \tag{A-11}$$

$$\equiv J. \tag{A-12}$$

Thus, J represents the rate of change of net potential energy with respect to crack advance (per unit thickness of crack front) for a nonlinear elastic solid. J also can be thought of as the energy flow into the crack-tip. Thus, J is a measure of the singularity strength at the crack-tip for the case of elastic-plastic material response.

This relationship can be used to infer an equivalent K_{Ic} value from J_{Ic} measurements in high toughness, ductile solids in which valid K_{Ic} testing will require unreasonably large test specimens.

A-3. HRR field [refs. 2, 3]

Consider a pure power law material response,

$$\frac{\epsilon}{\epsilon_0} = \alpha \left(\frac{\sigma}{\sigma_0}\right)^n \tag{A-13}$$

where α = material constant, σ_0 = reference yield strength, n = strain hardening exponent and ϵ_0 = reference yield strain = $\frac{\sigma_0}{E}$. For linear elastic material $n = 1$, for perfectly plastic response, $n = \infty$. With these assumptions, the crack-tip fields (HRR field) can be derived as

$$\sigma_{ij} = \sigma_0 \left(\frac{J}{\alpha\sigma_0\epsilon_0 I_n r}\right)^{\frac{n}{n+1}} \breve{\sigma}_{ij}(\theta, n) \tag{A-14}$$

$$\epsilon_{ij} = \alpha\sigma_0 \left(\frac{J}{\alpha\sigma_0\epsilon_0 I_n r}\right)^{\frac{1}{n+1}} \breve{\epsilon}_{ij}(\theta, n) \tag{A-15}$$

$$u_i = \alpha\sigma_0 \left(\frac{J}{\alpha\sigma_0\epsilon_0 I_n r}\right)^{\frac{n}{n+1}} r \ \breve{u}_i(\theta, n) \tag{A-16}$$

function I_n is a scaling integral depending on hardening exponent, n. $\breve{\sigma}_{ij}(\theta, n)$, $\breve{\epsilon}_{ij}(\theta, n)$ and $\breve{u}_i(\theta, n)$ are dimensionless angular stress, strain and displacement functions.

A-4. CTOD

The definition of CTOD, δ_t is somewhat arbitrary since the opening displacement varies as the crack-tip is approached and the also the distance from the crack-tip. A commonly used operational definition is based on the 45^0 construction depicted below or measured at a fixed distance behind the crack-tip.
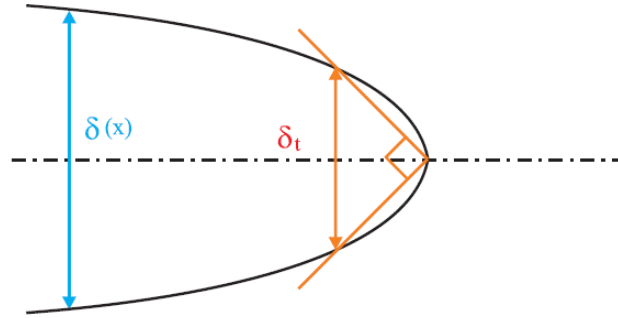

Figure A.5. Schematic representation of CTOD for a blunted crack

CTOD is related to J by the following expression,

$$\delta_t = d_n \frac{J}{\sigma_0} \tag{A-17}$$

where, d_n is a strong function of n, and a weak function of σ_0/E.

For Plane Strain condition,
$$d_n \approx 0.3 - 0.65 \ (\ 0.65 \ for \ n \ \rightarrow \ \infty \ ) \tag{A-18}$$

For Plane Stress condition,
$$d_n \approx 0.5 - 1.07 \ (\ 1.07 \ for \ n \ \rightarrow \ \infty \ ) \tag{A-19}$$

Presuming dominance of HRR fields,

$$\delta_t = d_n \frac{J}{\sigma_0} \approx \frac{J}{\sigma_0} \tag{A-20}$$

For Small, scale Yielding, (SSY),

$$J = \frac{K_I^2}{E}(1 - \mu^2) \tag{A-21}$$

$$\delta_t = d_n \frac{K_I^2}{E}\left(\frac{1 - \mu^2}{\sigma_0}\right) \tag{A-22}$$

A-4. Two-parameter Characterization

In the two-parameter characterization, the measure of asymptotic fields are represented by either stress intensity factor *K*, or the *J*-integral with an additional constraint parameter, such as the *T*-stress or stress difference *Q*. Generally, a two-parameter characterization is accomplished using modified boundary layer formulation (MBL). Characterization and application of two-parameter approach to crack problems were reported in fracture mechanics by numerous authors in references 6, 10-11, and 37-41. In the following sections, the terminologies used in J-T and J-Q two-parameter approach are briefly described.

A-4.1 J-T Theory

In the Williams expansion of a linear elastic stress field, the leading term has a $1/\sqrt{r}$ singularity and the second term is a term with *r*. The second term under mode I crack opening is referred to as the T-stress and is shown in Equation A-23. *T*-stress is defined as a uniform stress parallel to the crack plane and perpendicular to the crack front. The negative T-stresses characterizes low crack-tip constraint while a positive T-stress characterizes high crack tip constraint. Specimens or geometries with negative T-stress cannot maintain single parameter J-dominance due to loss of constraint associated with lowering of the stress state. However, to some extent, for negative T-stress specimens, state of stress around the crack tip can be characterized by J-integral and T-stress up to and not exceeding net section yielding [ref. 6]. With increase in applied load, changes in crack tip stress field distribution, plastic zone shape, and size changes lead to change in T-stress value. The size and shape of the plastic zone ahead of the crack tip is directly dependent on constraint level. Dependence of plastic zone size and shape on T-stress is shown in Figure A-6. Low *T* ($T/\sigma_o = -1$) results in moving the plastic zone away from the crack front/tip while high *T* ($T/\sigma_o = +1$) shifts the zone towards the opening face/tip. Zero T/σ_o results in a plastic zone is a common of the "plane-strain" small scale yielding condition. The *T*-stress factors are available in literature for a number of standard facture mechanics specimens making it a valuable measure of constraint for engineering applications.

$$\sigma_{ij}(r,\theta) = \frac{K_I}{\sqrt{2\pi r}} f_{ij}(\theta) + T\delta_{1i}\delta_{1j} \qquad (A\text{-}23)$$
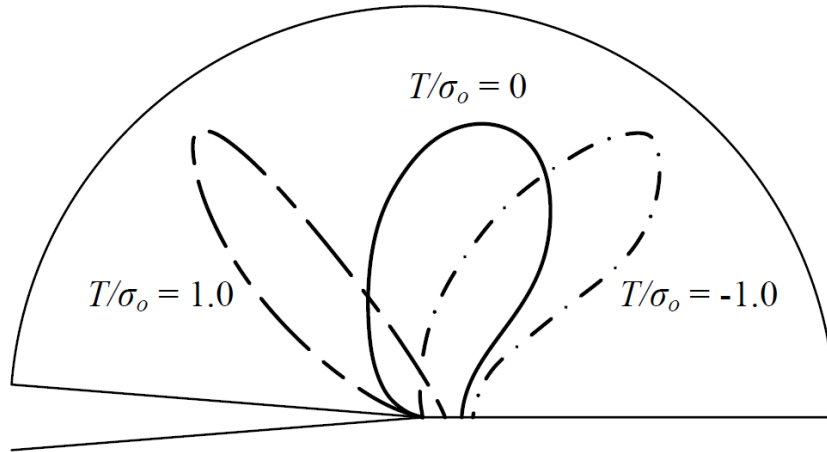
where, δ_{ij} is the Kronecker delta.

Figure A.6. Plastic zone shapes diagram for high (T/σₒ = 1), zero (T/σₒ = 0) and low (T/σₒ = -1) T-stresses. (σₒ is the yield stress of the material)

A-4.2 J-Q Theory

As mentioned previously, measure of stress field within the plastic zone is a more accurate determination of constraint within the plastic zone. A more accurate measure of constraint around the crack tip and within the plastic zone for geometries undergoing large-scale plasticity can be accomplished by estimating the Q-parameter. Wang [ref. 26] showed that the Q parameter as a measure of the difference between the actual opening stress and the small scale yielding solution for a range of normalized radial distance $(r/(J/\sigma_o))$. Many investigators have implemented J-Q theory to characterize crack tip stress fields for 2D and 3D geometries [refs. 10-11, 37-41]. The parameter Q is estimated as the difference between the actual hoop stress $(\sigma_{\theta\theta})$ and a reference hoop stress within a cracked body. Using Q parameter, the near crack tip field is represented by [refs. 10, 11],

$$\sigma_{ij}(r,\theta) = \left[\sigma_{ij}\left(\frac{r}{J/\sigma_o},\theta\right)\right]_{T=0} + Q\sigma_o\delta_{ij} \; for \; {}^{-\pi}/_2 \leq \theta \leq {}^{\pi}/_2 \tag{A-24}$$

within a range of normalized radial distances, typically $1.5 \leq r/(J/\sigma_o) \leq 5$.

The first term is equation A-24 is the small scale yielding solution and δ_{ij} is the Kronecker delta. Silva et al. [ref. 41] have shown that, Q parameter can be considered as a fracture parameter by evaluating at a fixed normalized radial distance equal to $2J/\sigma_0$ from the crack tip. This marks the location from where cleavage mechanism of fracture is triggered ahead of the crack tip. Following that, Q can now be defined as the hoop stress difference in the cracked plane (opening stress or σ_{yy}) at a radial distance equal to $2J/\sigma_0$:

$$Q = \frac{\sigma_{yy} - (\sigma_{yy})_{T=0}}{\sigma_o} \; at \; \theta = 0 \; and \; r = 2J/\sigma_0 \tag{A-25}$$

Using this definition of constraint, a plane-strain J-Q family of curves can be constructed using the modified boundary layer finite element formulation for different materials and loading conditions.

Appendix B. Material Testing Summary

Material characterization and fracture tests were conducted on 2024-T3 aluminum coupons extracted from 1-inch thick plates. The material characterization tests included tensile and tension/torsion tests to generate data for the stress-strain model required in the finite element analysis. The fracture tests included several different configurations to provide different levels of constraint for evaluation of the fracture model. The following sections describe each type of test conducted.

Tensile Tests

The tensile tests were conducted on round coupons that had a reduced diameter gage section, as shown in Figure B.1. The coupons were loaded under displacement control at a ramp rate of 0.01 inch/minute. Three identical coupons were tested and full-field strain and displacement measurements were made using digital image correlation (DIC), as shown in Figure B.2. The DIC produced the full-field displacements for both the gage section and the visible ends of the larger diameter grip section. The global strain was obtained using virtual extensometers to extract the relative displacement of two points that were initially 1 inch apart. The location of the virtual extensometer was selected after the test to include the region that experienced localized necking. The global stresses were calculated from the initial area and the applied load measurement.

The local strains used a similar virtual extensometer, but with an initial gage length that was 0.1-inch apart and located in the necking region. The local stresses were obtained by using the DIC measurements to calculate the reduction in the coupon radius as the coupon is stretch axially. The resulting local stress-strain curve has greater strains and higher stresses than the global stress-strain curve.
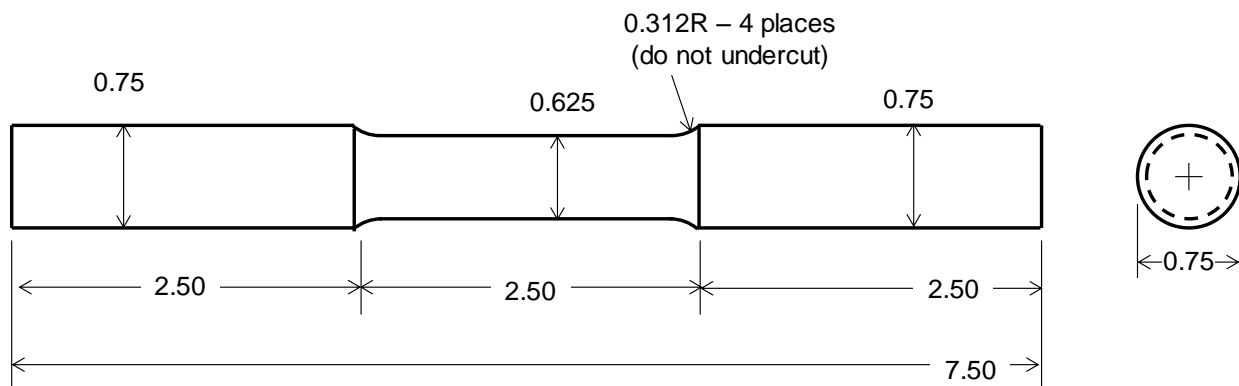

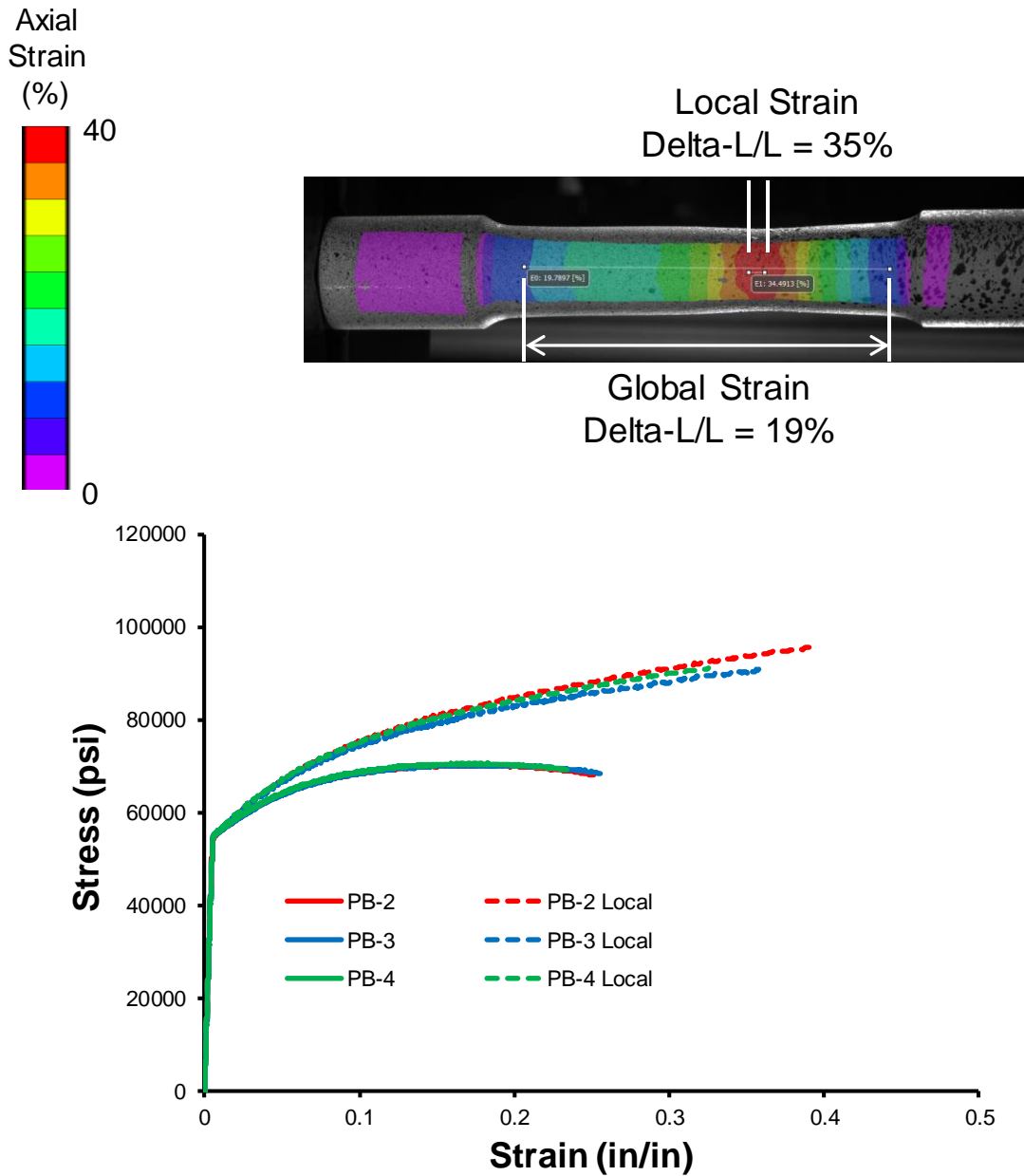*Figure B.1. Dimensions of the tensile coupon.*

Figure B.2. Measurement of global and local strains using DIC.

Tension/Torsion Tests

Combined tension and torsion tests were conducted to provide data to verify that the material model used in the finite element analysis accurately depicted the behavior of the material. The coupons were round, hollow, and notched, as shown in Figure B.3. The tests were conducted at a constant rotation rate (2-degrees per minute) while loading in tension at a constant load. The full-field rotations, displacements, and strains were measured using DIC. The reported angular rotations were obtained by extracting points that were on the larger diameter grip section and were initially 2.65 inches apart. The coupons were loaded to a constant value and the torque was increased, as shown in Figure B.4. The maximum rotation of the load frame was about 90-degrees, so the tests were not taken to failure. The maximum rotation was achieved by

starting coupons PF-2, PF-3, and PF-4 at a load frame controller angle of -45-degrees and rotating to +45-degrees. Coupon PF-1 was started at a load frame controller angle of 0-degrees, so the maximum angle that could be achieved was 45-degrees.
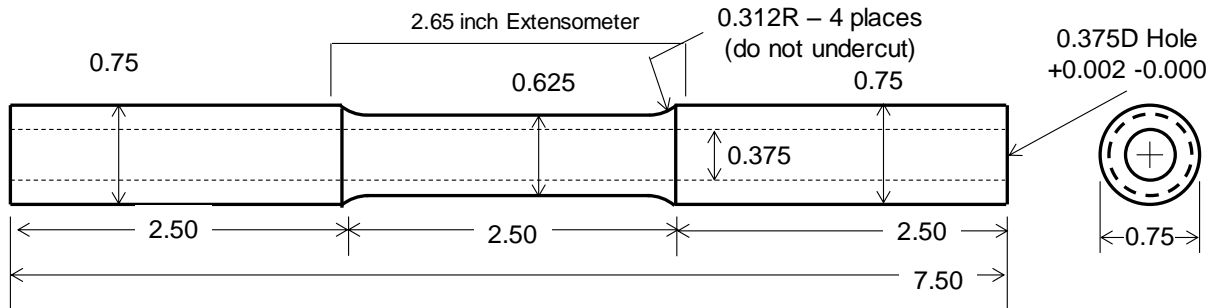
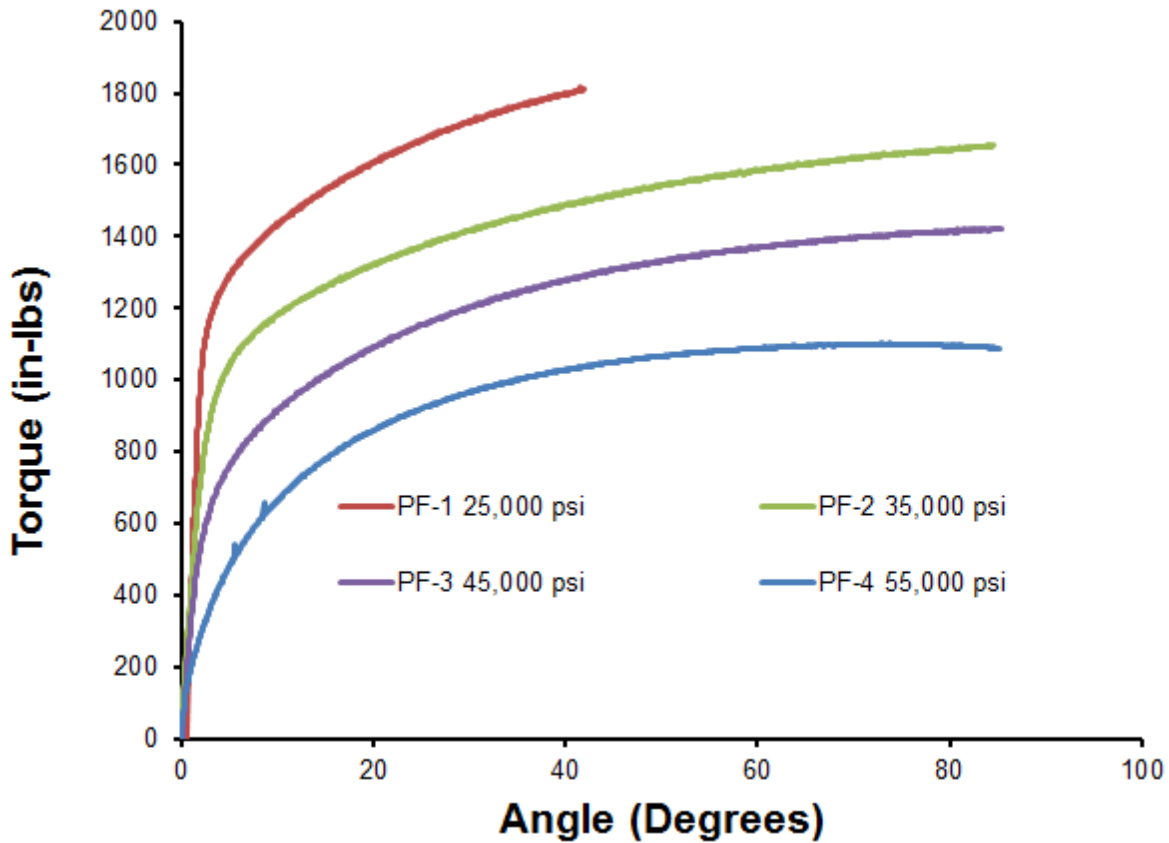*Figure B.3. Dimensions of the tension/torsion coupon*

Figure B.4. Results from the tension/torsion tests.

3PTB Tests

3PTB tests were conducted on 0.75-inch-thick coupons. Two different notch sizes were used: long notch (0.6 inch) and short notch (0.3). The dimensions of the short notch coupon are provided in Figure B.5. The long notch coupons were identical to the short notch coupons with the exception of the notch length.

The 3PTB coupons were fatigue precracked elastically at a stress ratio of R = 0.1 and a peak stress intensity factor of about 8 ksi inch$^{1/2}$. The dimensions of the 3PTB loading fixture is provided in Figure B.6. The coupons were loaded to failure under displacement control at a rate of 0.005 inch/minute.

Chevron Notch Detail
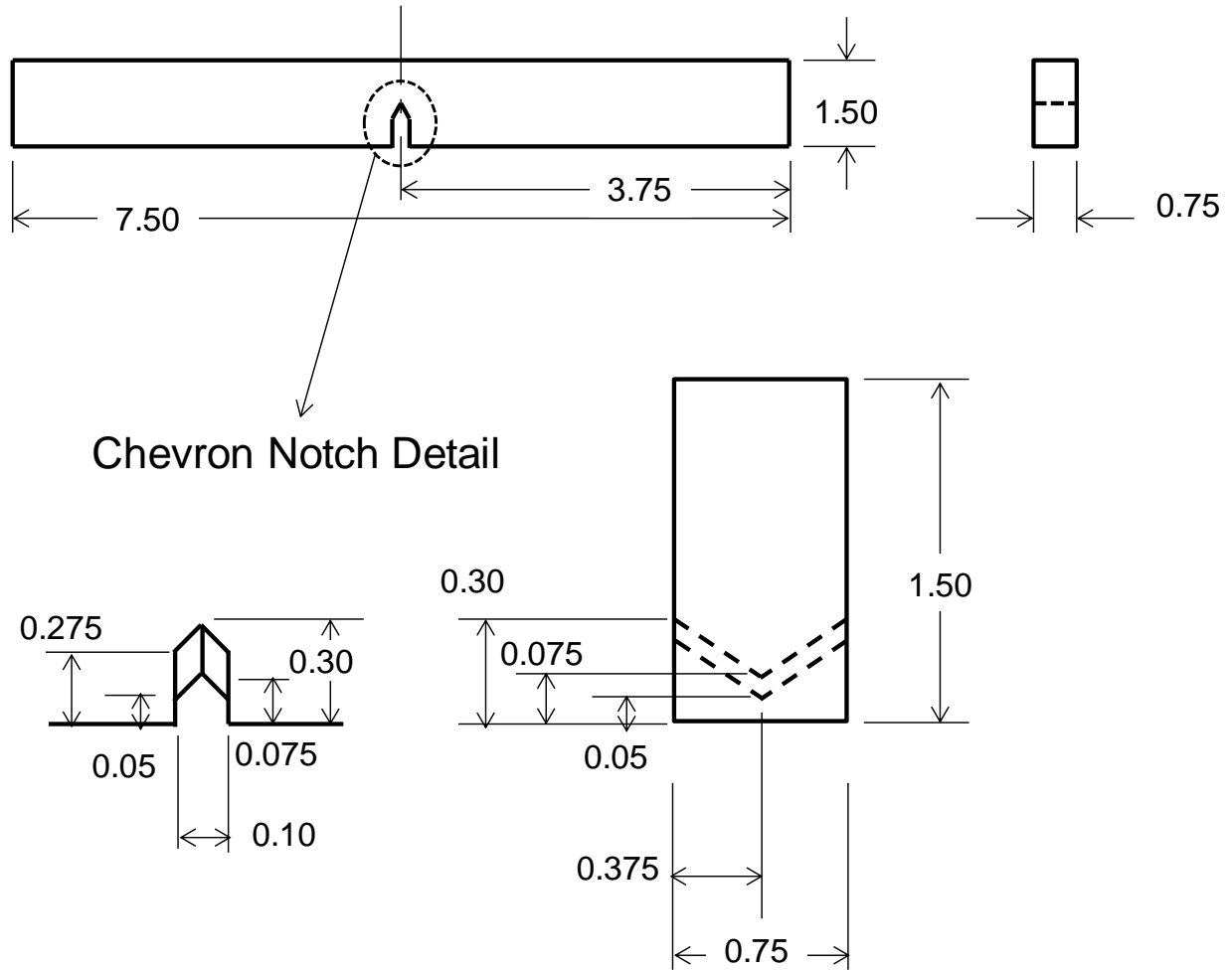
Figure B.5. Dimensions of the short notch 3PTB coupons.

DIC was used to measure the notch tip opening displacement as a function of the applied load, as shown in Figure B.7. The crack length after the fatigue precracking was measured by examining the post-failure surface and averaging the length across the crack front, as shown in Figure B.8. The crack growth during stable tearing created a distinct difference in the fracture morphology, clearly marking the end of the fatigue crack growth region. The initial crack length and the resulting failure load from the 3PTB tests are shown in Figure B.9.
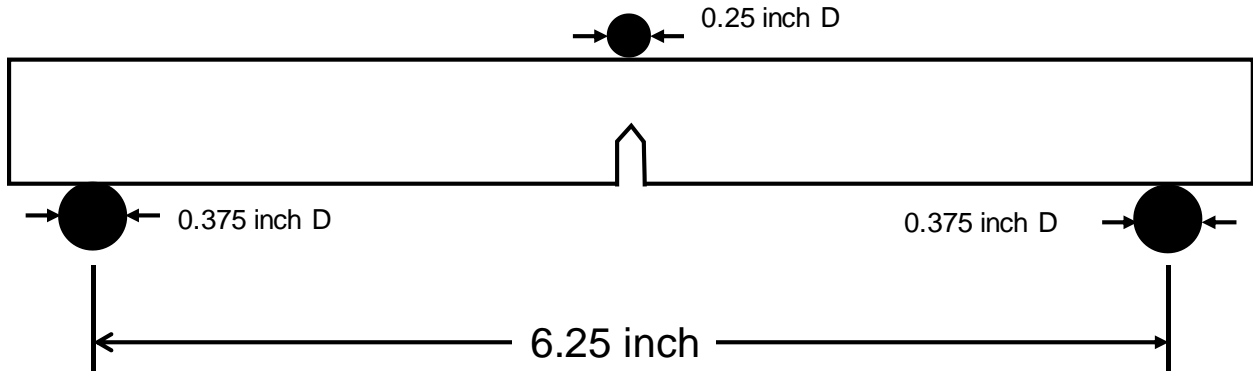
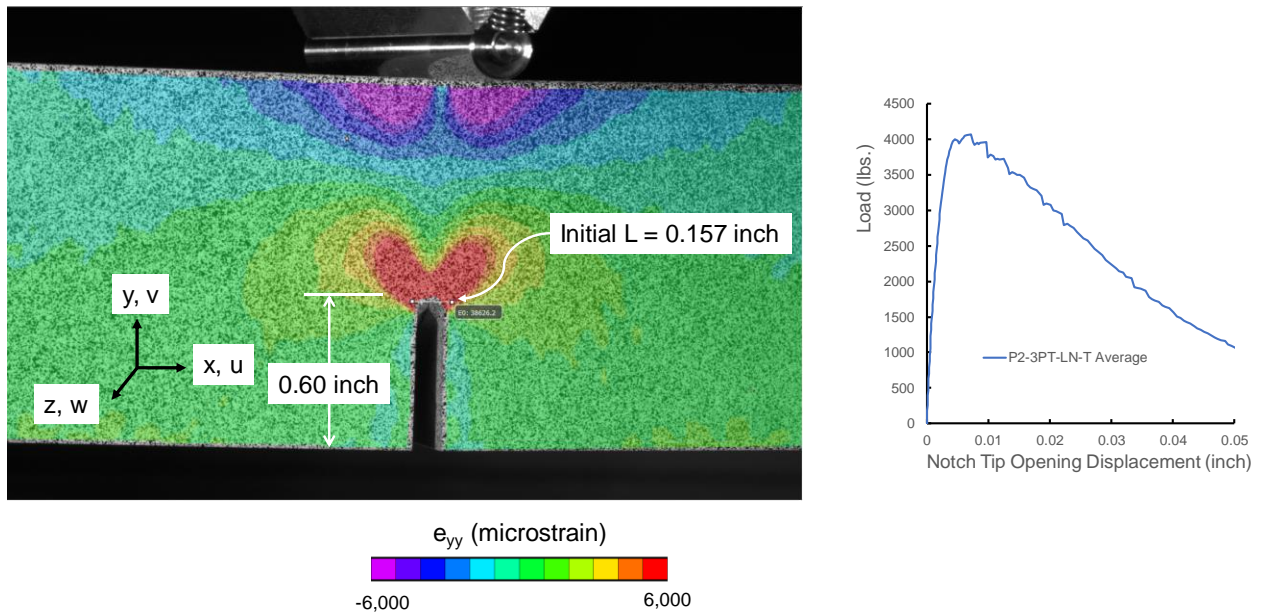*Figure B.6. Dimensions of the 3PTB loading fixture.*

e_{yy} (microstrain)

-6,000   6,000

Figure B.7. Measurement of the notch tip opening displacement for a 3PTB test.
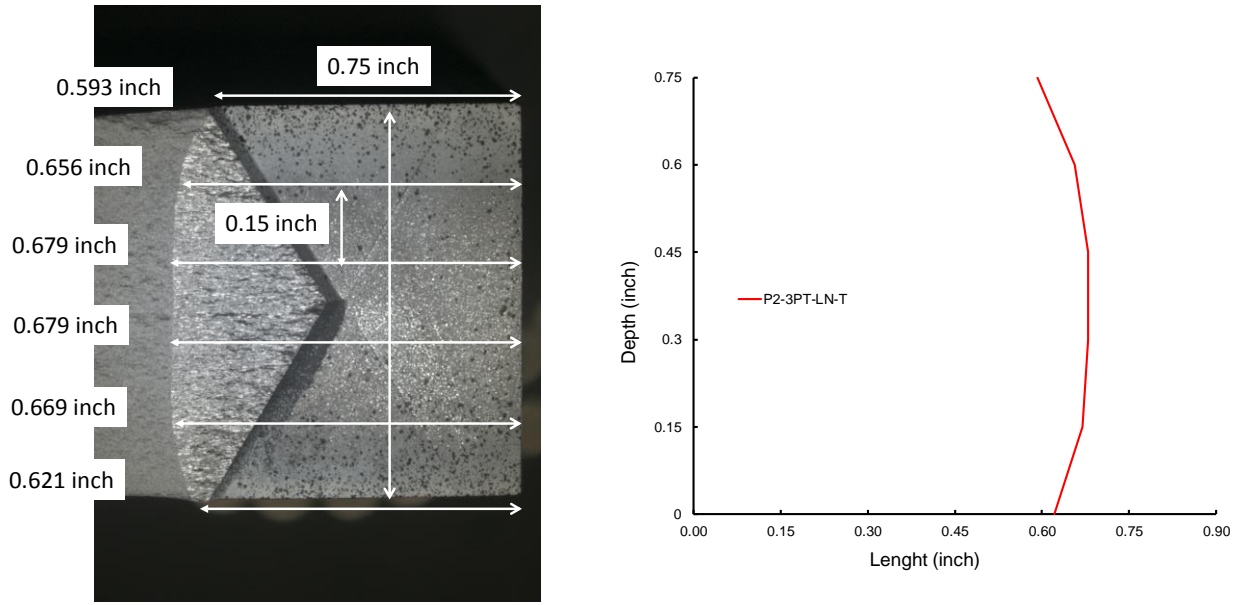
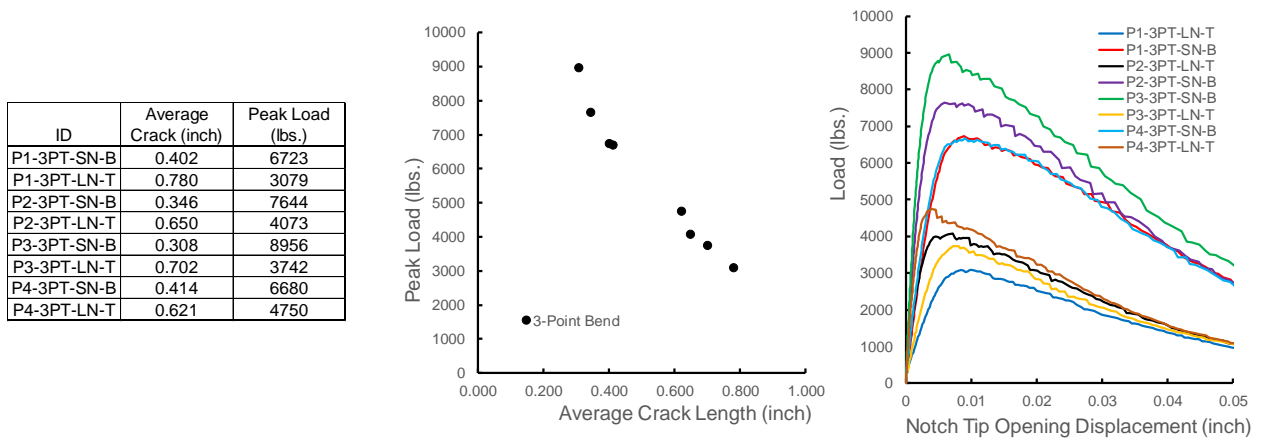*Figure B.8. Measurement of the initial crack length in the 3PTB tests.*

ID	Average Crack (inch)	Peak Load (lbs.)
P1-3PT-SN-B	0.402	6723
P1-3PT-LN-T	0.780	3079
P2-3PT-SN-B	0.346	7644
P2-3PT-LN-T	0.650	4073
P3-3PT-SN-B	0.308	8956
P3-3PT-LN-T	0.702	3742
P4-3PT-SN-B	0.414	6680
P4-3PT-LN-T	0.621	4750

Figure B.9. Results from the 3PTB tests.

Middle Crack Tension Tests

Middle crack tension tests were conducted on coupons that were proportionally the same size but with widths of W = 3, 6, and 12 inches. The basic shape of the coupons is shown in Figure B.10. The coupons were 1-inch thick and were precracked to a total crack length that was 1/3 of the width. The precracking was performed elastically at a stress ratio of R = 0.1 and a peak stress intensity factor of about 8 ksi inch$^{1/2}$. The coupons were loaded to failure under displacement control at a rate of 0.01 inch/minute. The recorded coupon width and failure stresses are provided in Table B.1.
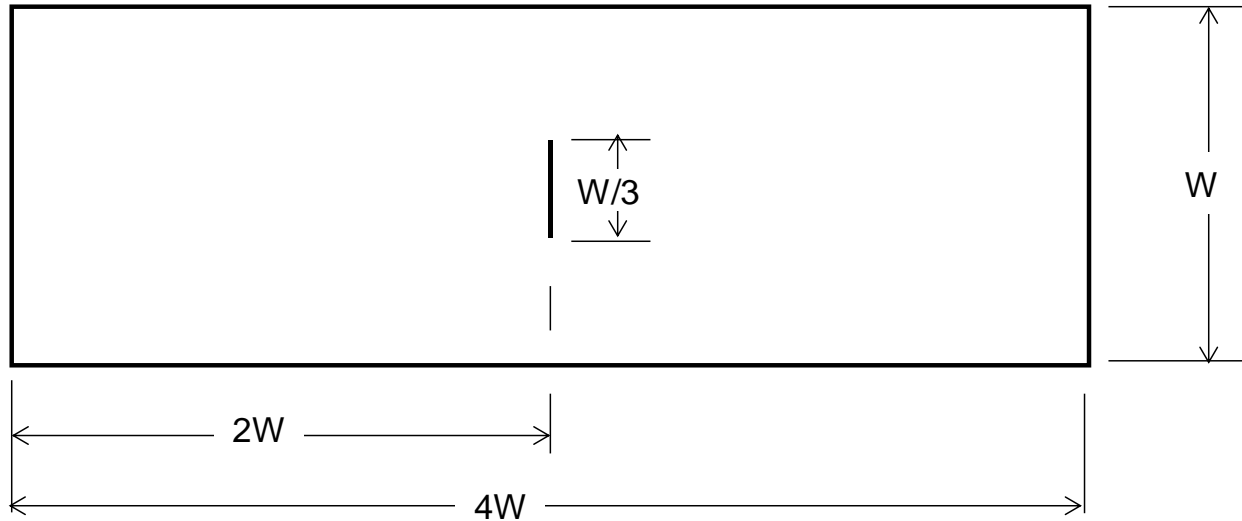
Figure B.10. Dimension of the middle crack tension coupon.

Table B.1. Results from the Middle Crack Tension Tests

Coupon ID	Width (inch)	Stress (psi)
MT3-1-P21	3	27.6
MT3-2-P22	3	30.1
MT6-1-P21	6	27.8
MT6-2-P22	6	27.9
MT12-1-P23	12	24.9
MT12-2-P23	12	25.2

CT Tests

CT tests were conducted on coupons that were proportionally the same size but with widths of W = 2, 4, 6, and 8 inches. The basic shape of the coupons is shown in Figure B.11. The coupons were 0.75-inch thick and were precracked to different crack lengths. The precracking was performed elastically at a stress ratio of R = 0.1 and a peak stress intensity factor of about 8 ksi inch$^{1/2}$. The coupons were loaded under displacement control to failure at a rate of 0.01 inch/minute. The recorded coupon width, crack length, and failure loads are provided in Table B.2.

Table B.2. Results from the CT Tests

Coupon ID	Width (inch)	Initial Crack Length (inch)	Load (lbs.)
1-P21	1.001	2	5.2
CT2-2-P22	0.801	2	7.45
CT2-3-P21	1.003	2	5.488
CT4-1-P21	2.831	4	3.426
CT4-2-P21	2.81	4	3.587
CT4-3-P21	2	4	10.14
CT4-4-P21	2.005	4	10.13
CT6-1-P21	3	6	14.18
CT6-2-P21	3.004	6	14.81
CT8-1-P21	5.811	8	6.876
CT8-3-P21	4.025	8	18.68
CT8-4-P21	4.098	8	19.28
CT8-5-P21	2.402	8	37.48
CT8-6-P21	2.401	8	37.19
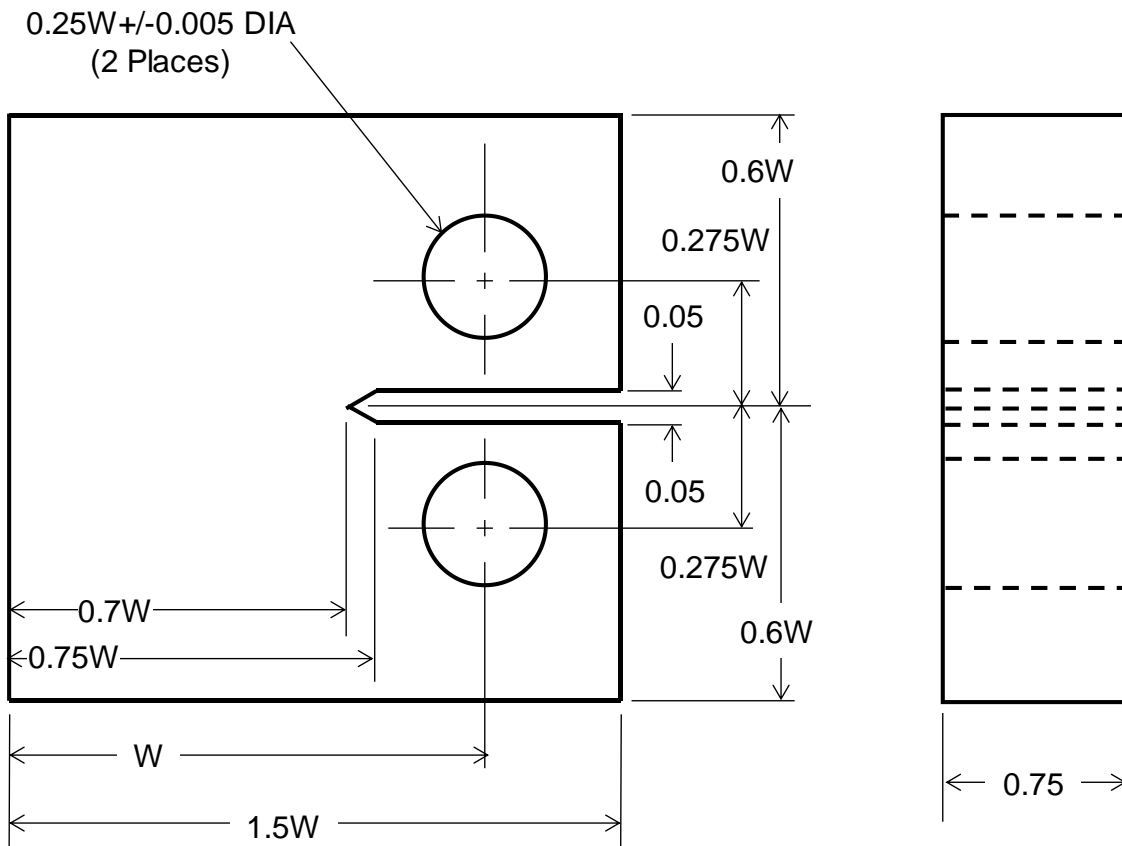
Figure B.11. Dimensions of the CT coupons.

Three-hole Tension

Fracture tests were conducted on the three-hole tension configuration shown in Figure B.12. The smaller hole was notched and the coupon fatigue cycled at a stress ratio of R = 0.1 and a peak stress intensity factor of about 8 ksi inch$^{1/2}$. The coupons were loaded to failure under displacement control at a rate of 0.01 inch/minute. The crack length after the fatigue precracking was measured by examining the post-failure surface and averaging the length across the crack front, as shown in Figure B.13. The crack growth during stable tearing created a distinct difference in the fracture morphology, clearly marking the end of the fatigue crack growth region. DIC was used to characterize the notch opening displacement as shown in Figure B.14. A summary of the initial crack lengths and stress as a function of notch opening displacement is provided in Figure B.15.
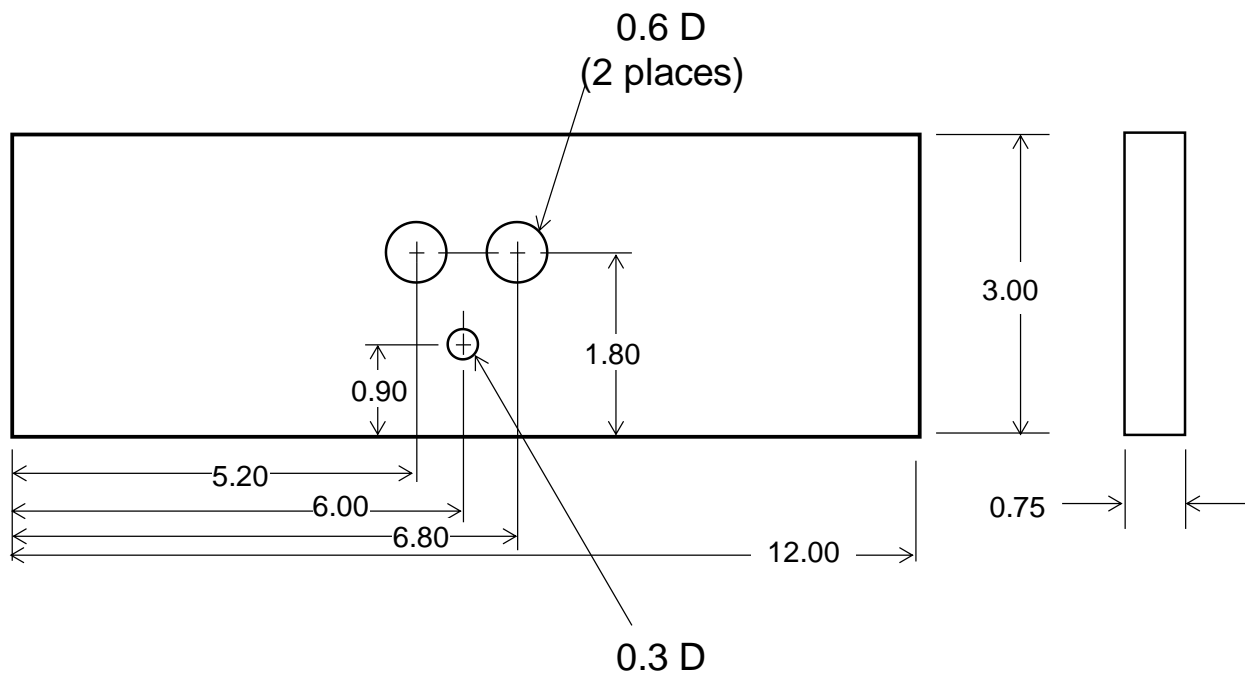
Figure B.12. Dimensions of the three-hole tension coupons.
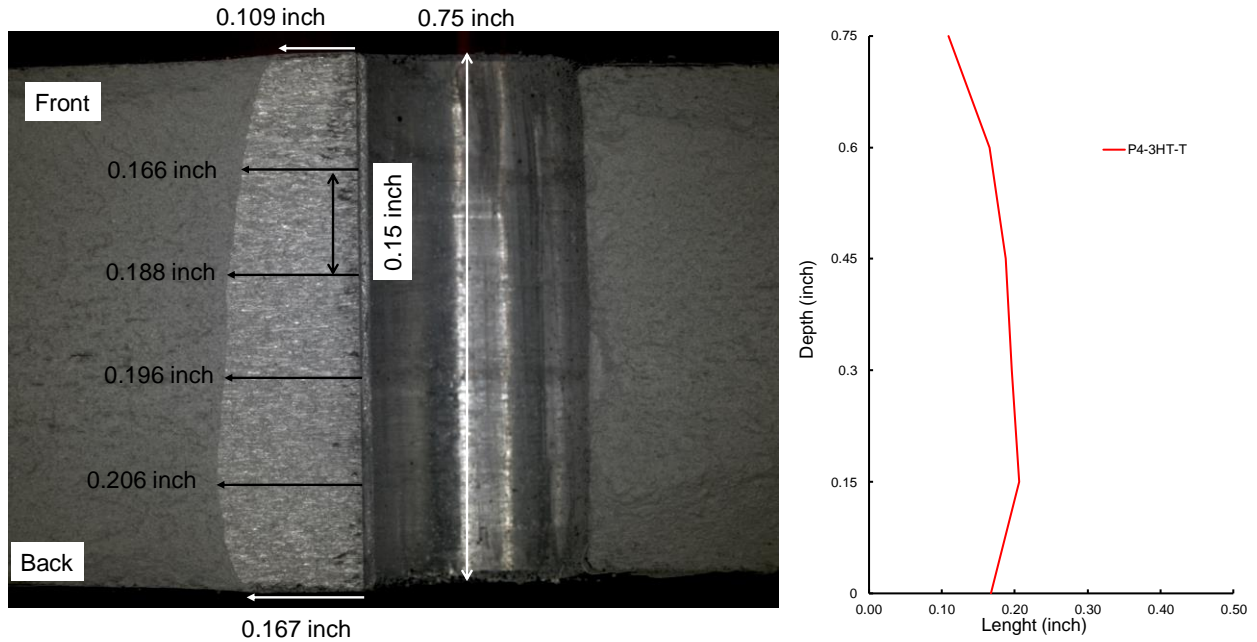
Figure B.13. Measurement of the initial crack length in the three-hole tension tests.
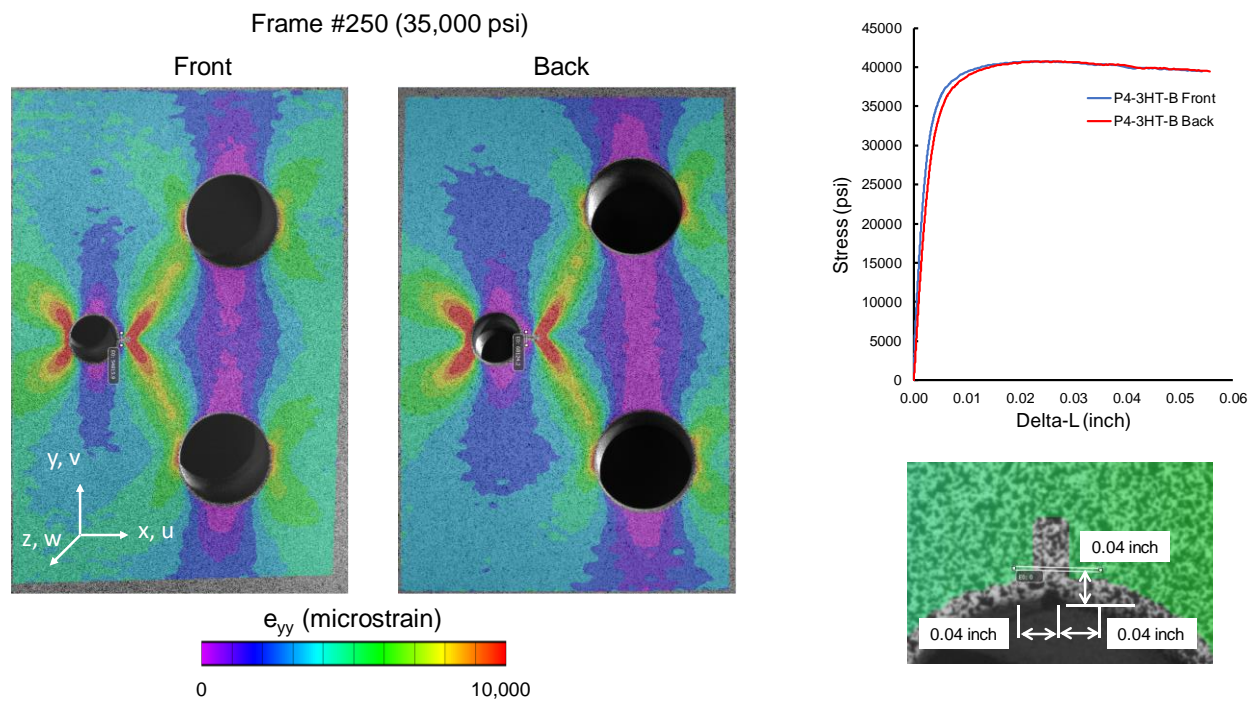

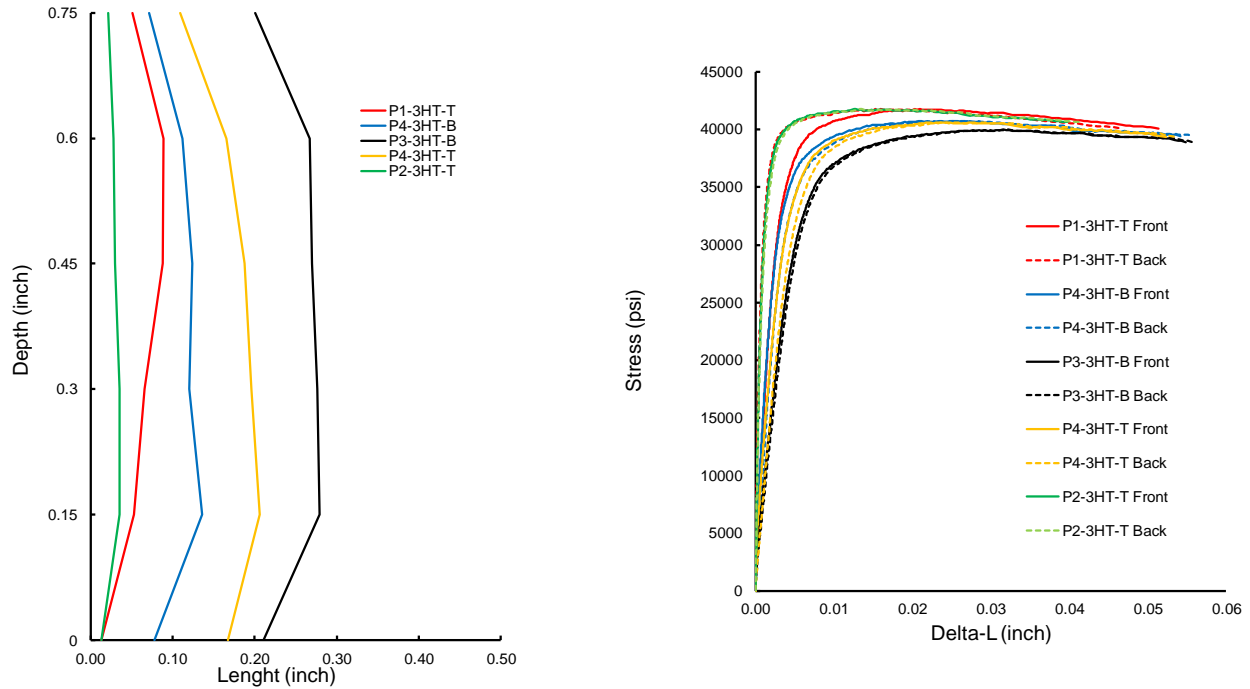*Figure B.14. DIC measurements from a three-hole tension tes.t*

Figure B.15. Initial crack lengths and failure stresses from the three-hole tension tests.

3PCT

Fracture tests were conducted on the 3PCT configuration shown in Figure B.16. The coupons were fatigue cycled at a stress ratio of $R = 0.1$ and a peak stress intensity factor of about 8 ksi inch$^{1/2}$. The coupons were loaded to failure under displacement control at a rate of 0.01 inch/minute. The crack length after the fatigue precracking was measured by examining the post-failure surface and averaging the length across the crack front, as shown in Figure B.17. The crack growth during stable tearing created a distinct difference in the fracture morphology, clearly marking the end of the fatigue crack growth region. DIC was used to characterize the notch opening displacement as shown in Figure B.18. A summary of the initial crack lengths and stress as a function of notch opening displacement is provided in Figure B.19.
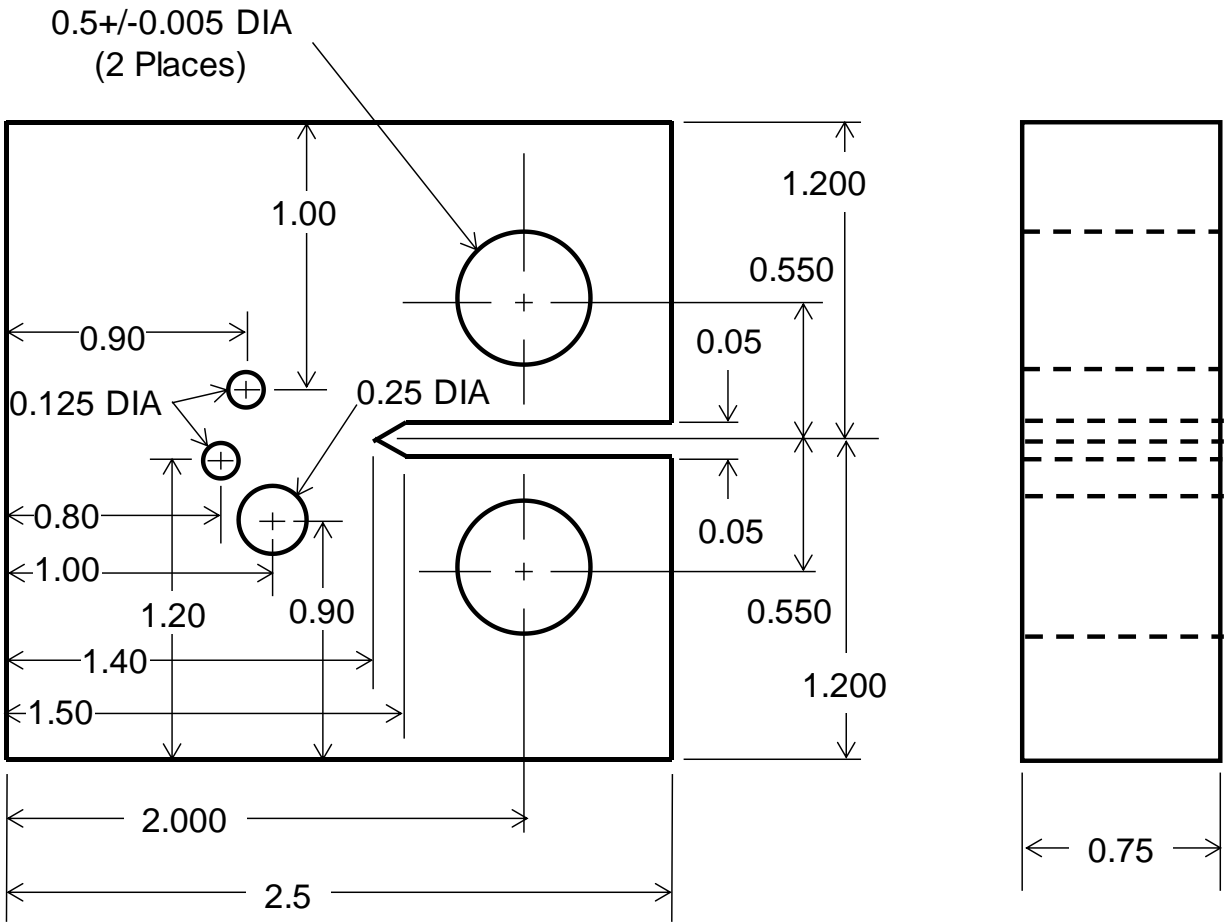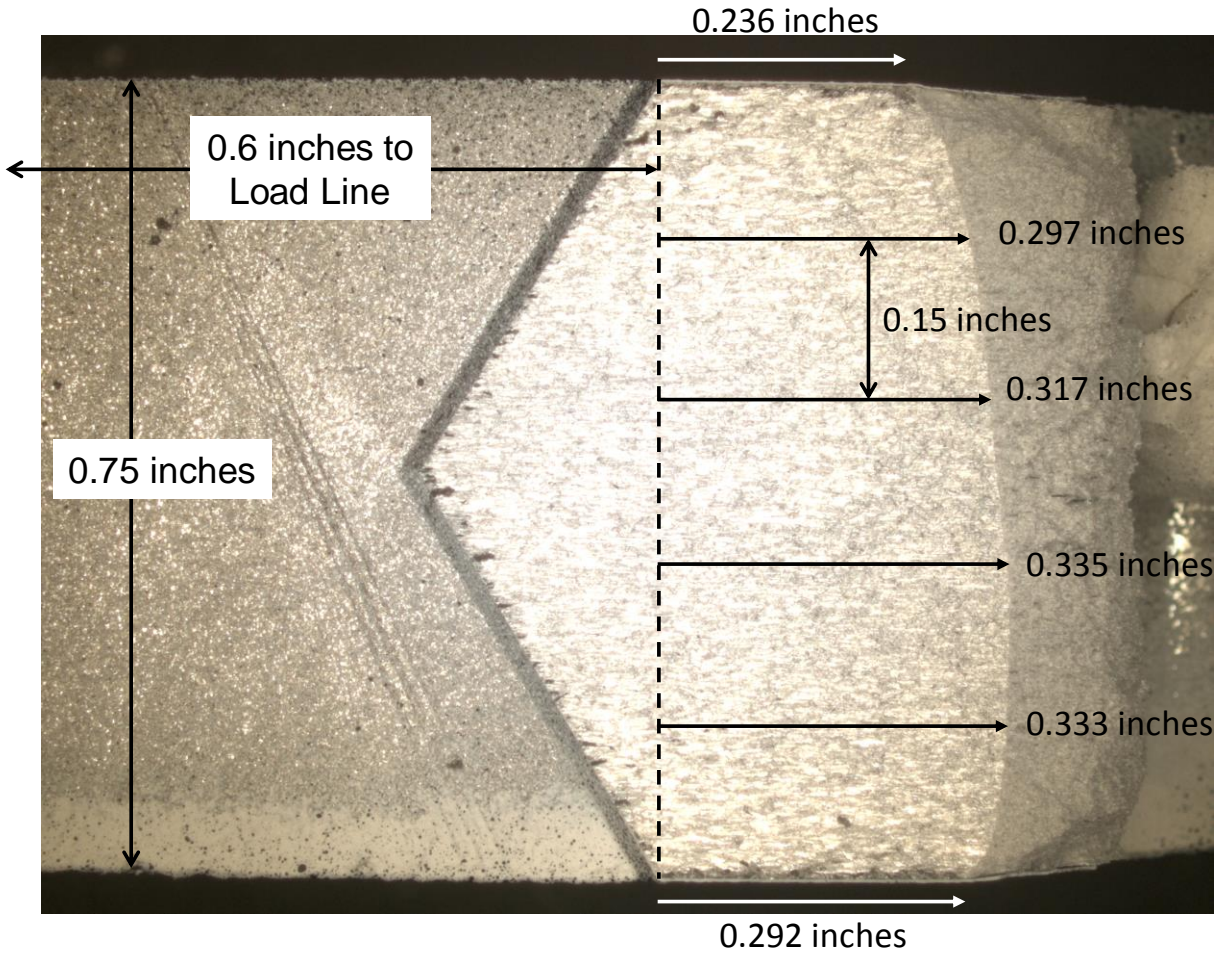
Figure B.16. Dimensions of the 3PCT coupons.

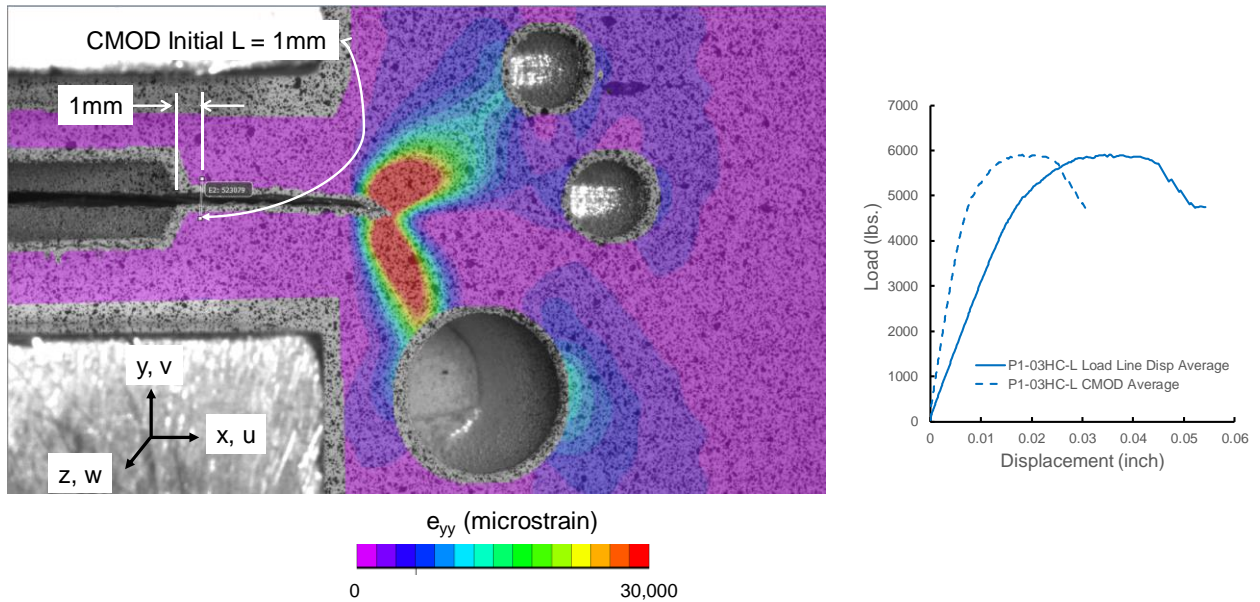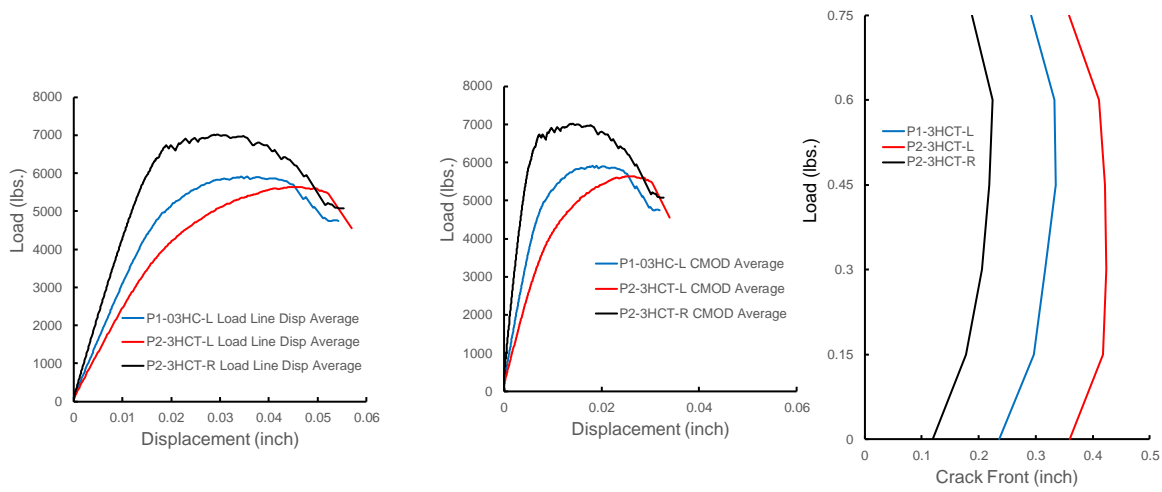*Figure B.17. Measurement of the initial crack length in the 3PCT tests.*

Figure B.18. DIC measurements from a 3PCT test.

Note: The crack front is the distance from the notch to the end of precracking. The total crack length needs an additional 0.6 inch length.

Figure B.19. Initial crack lengths and failure loads from the 3PCT tests.

REPORT DOCUMENTATION PAGE

1. REPORT DATE *(DD-MM-YYYY)*	2. REPORT TYPE	3. DATES COVERED *(From - To)*
11/15/2018	Technical Memorandum	

4. TITLE AND SUBTITLE	5a. CONTRACT NUMBER
Implementation of J-A Methodology Elastic-Plastic Crack Instability Analysis Capability into the WARP-3D Code	
	5b. GRANT NUMBER
	5c. PROGRAM ELEMENT NUMBER

6. AUTHOR(S)	5d. PROJECT NUMBER
Hamm, Kenneth Rl, Jr.; Seshadri, Banavara R.; Dawicke, David S.; Raju, Ivatury S.	
	5e. TASK NUMBER
	5f. WORK UNIT NUMBER
	869021.05.07.02.11

7. PERFORMING ORGANIZATION NAME(S) AND ADDRESS(ES)	8. PERFORMING ORGANIZATION REPORT NUMBER
NASA Langley Research Center Hampton, VA 23681-2199	L-20979 NESC-RP-14-01001

9. SPONSORING/MONITORING AGENCY NAME(S) AND ADDRESS(ES)	10. SPONSOR/MONITOR'S ACRONYM(S)
National Aeronautics and Space Administration Washington, DC 20546-0001	NASA
	11. SPONSOR/MONITOR'S REPORT NUMBER(S)
	NASA/TM-2018-220115

12. DISTRIBUTION/AVAILABILITY STATEMENT

Unclassified - Unlimited
Subject Category 16 Space Transportation and Safety
Availability: NASA STI Program (757) 864-9658

13. SUPPLEMENTARY NOTES

14. ABSTRACT

Characterization of the near crack-tip stress/strain fields is the foundation of fracture mechanics. Determination of stress field and constraint around the crack tip is critical for achieving reliable fracture control analysis results for all space and non-space programs that require fracture control analysis. For effectively performing this improved analysis approach, a special software code was required that was accurate, efficient, and easy to use. This report summarizes the attempts at ongoing processes to achieve development of such software.

15. SUBJECT TERMS

Cracked Plate; Elastic-Plastic Fracture Mechanics; NASA Engineering and Safety Center; J-A Methodology; WARP-3D Code

16. SECURITY CLASSIFICATION OF:			17. LIMITATION OF ABSTRACT	18. NUMBER OF PAGES	19a. NAME OF RESPONSIBLE PERSON
a. REPORT	b. ABSTRACT	c. THIS PAGE			STI Help Desk (email: help@sti.nasa.gov)
					19b. TELEPHONE NUMBER *(Include area code)*
U	U	U	UU	72	(443) 757-5802